MIXED FORMULATIONS IN SPACE AND TIME DISCRETIZATIONS FOR THE FIXED-STRESS SPLIT METHOD IN POROMECHANICS

A Dissertation

by

HYUN CHUL YOON

Submitted to the Office of Graduate and Professional Studies of
Texas A&M University
in partial fulfillment of the requirements for the degree of

DOCTOR OF PHILOSOPHY

Chair of Committee,	Jihoon Kim
Committee Members,	Nobuo Morita
	Hadi Nasrabadi
	Joseph Sang-Il Kwon
Head of Department,	A. Daniel Hill

December 2017

Major Subject: Petroleum Engineering

ABSTRACT

Coupled flow and geomechanics become one of the important research topics in oil and gas industry for development of unconventional petroleum reservoirs such as gas shale, tight gas, and gas hydrates. In particular, these reservoirs are naturally born with its complex behavior, exhibiting strong non-linearity, anisotropy, and heterogeneity effects within each geomaterial and fluid by itself. In addition, the coupling between flow and geomechanics is more complicated for unconsolidated reservoirs or shale formations. Thus, it is critical to assess these complex coupled processes properly through poromechanics with forward numerical simulation and to provide more accurate solutions in order to predict the reservoir performance more precisely.

The main objective of this study is to address several numerical issues that are accompanied with simulation in poromechanics. We perform in-depth analysis on mathematical conditions to satisfy for numerically stable and accurate solution, employing various mixed formulations in space and time discretization.

Specifically, in space discretization, we deal with the spatial instability that occurs at early times in poromechanics simulation, such as a consolidation problem. We identify two types of spatial instabilities caused by violation of two different conditions: the condition due to discontinuity in pressure and the inf-sup condition related to incompressible fluid, which both occur at early times. We find that the fixed-stress split with the finite volume method for flow and finite element method for geomechanics can provide stability in space, allowing discontinuity of pressure and circumventing violation of the inf-sup condition.

In time discretization, we investigate the order of accuracy in time integration with the fixed-stress sequential method. In the study, two-pass and deferred correction methods

are to be considered for studying the high-order methods in time integration. We find that there are two different inherent constraint structures that still cause order reductions against high-order accuracy while applying the two methods.

As an additional in-depth analysis, we study a large deformation system, considering anisotropic properties for geomechanical and fluid flow parameters, the traverse isotropy and permeability anisotropy ratio. Seeking more accurate solutions, we adopt the total Lagrangian method in geomechanics and multi-point flux approximation in fluid flow. By comparing it to the infinitesimal transformation with two-point flux approximation, we find that substantial differences between the two approaches can exist.

For a field application, we study large-scale geomechanics simulation that can honor measured well data, which leads to a constrained geomechanics problem. We employ the Uzawa's algorithm to solve the saddle point problem from the constrained poromechanics. From numerical parallel simulations, we estimate initial stress distribution in the shale gas reservoir, which will be used for the field development plan.

From this study, we find several mathematical conditions for numerically stable and accurate solution of poromechanics problems, when we take the various mixed formulations. By considering the conditions, we can overcome the numerical issues. Then, reliable and precise prediction of reservoir behavior can be obtained for coupled flow-geomechanics problems.

DEDICATION

To all who have been willing to await me,

especially to my family who are my strength,

parents, grandparents, only sister, even my future wife and child,

also to all my friends who cheer me up,

and above all with ultimate glory, to my God who is good all the time.

ACKNOWLEDGMENTS

First of all, I would like to express my deep gratitude to my advisor Dr. Kim, who is the one that has led me into the genuine research world with poromechanics. Even though I've stumbled and failed a lot, through his continuous support, training and persistence, I've stood up again and walked forward to my PhD study. And here I am standing on a small but harsh mountain under his great guidance.

I also appreciate Dr. Morita's kind advice and immense knowledge and experience in this field. Although his mastery shed light on so many paths not only around him but also all over the world, it is his modesty that dragged me more into the research and guided me up to the goal.

I am also grateful to have Dr. Nasrabadi as my committee member. His expertise and rock solid knowledge in petroleum engineering, especially with reservoir simulation, provided me acute and deep insight into the coupling concept and its application.

And finally, I also would like thank Dr. Kwon sincerely. Through diverse conversations that we shared, I could bring many brilliant ideas up to the research. His greatness in the field of optimizing and control promoted me to step further with curiosity.

As a closing acknowledgement, special thanks should go to Dr. Moridis and Dr. Blasingame who provided me a big firm bridge from a starting point of a graduate student leading up to this research and thesis.

With many thanks to all of my advisors.

CONTRIBUTORS AND FUNDING SOURCES

Contributors

This work was supported and supervised by a dissertation committee consisting of Professor Dr. Jihoon Kim (advisor), Professors Dr. Nobuo Morita and Dr. Hadi Nasrabadi of the Department of Petroleum Engineering and Professor Dr. Joseph Kwon of the Department of Chemical engineering. The data analyzed for Chapter 6 was provided by Professor Dr. Ding Zhu of the Department of Petroleum Engineering. All other work conducted for the dissertation was completed by Hyun Chul Yoon independently.

Funding Sources

Graduate study was supported by the funds from the Crisman Institute for Petroleum Research at Texas A&M University, University of Texas at Austin, PetroChina, and Department of Energy, Methane Hydrate Program (DE-FE-0028973).

NOMENCLATURE

PDE	Partial Differential Equation
DAE	Differential Algebraic Equation
ODE	Ordinary Differential Equation
FEM	Finite Element Method
FVM	Finite Volume Method
LBB	Ladyzhenskaya-Babuška-Brezzi
BDF	Backward Differentiation Formula
RK	Runge-Kutta
DC	Deferred Correction
CDC	Classical Deferred Correction
SDC	Spectral Deferred Correction
TPFA	Two Point Flux Approximation
MPFA	Multi Point Flux Approximation
TL	Total Lagrangian
IT	Infinitesimal Transformation
SGeMS	Stanford Geostatistical Modeling Software
TAMU HPRC	Texas A&M University High Performance Research Computing Center

TABLE OF CONTENTS

Page

LIST OF FIGURES

FIGURE Page

LIST OF TABLES

TABLE Page

1. INTRODUCTION

1.1 Overview and Objective of the Research

Geomechanics are getting more attention than ever in petroleum engineering and reservoir simulation community since the oil and gas industry is aiming for more cost effective production from unconventional reservoirs, such as tight or shale play and heavy oil and gas systems [1]. For example, hydraulic fracturing plays the key role for shale gas and liquid production. There are several factors affecting fracture propagation, such as the rock type, natural fractures and lateral stress distribution, which all need an optimization process including refracturing [2]. Beyond oil and gas systems, different types of new energy techniques can be closely related to the geomechanical analysis too. For example, the carbon (CO_2) storage technique, which sometimes may also lead to the enhanced oil recovery in depleted reservoirs, has opened a new era for environmental and energy industry but it needs geomechanics to watch for the firm storage of CO_2. In addition, a geothermal system where higher stress and temperature exists than in the conventional reservoirs needs to account for the complex geomechanical effects to the flow or vice versa.

Coupling effects between geomechanics and fluid flow can add severe advantage or disadvantage to production activities or reservoir performance. Two-way streets among geomechanics and fluid flow generate multiphysical effects to each other and highly nonlinear behavior of the formation [3, 4]. Change in in-situ stress within formations can result in compaction, which can lead to consolidation or settlement. Volume or porosity change within formation can affect change in-situ stress and vice versa. For example, production of oil or gas from hydrocarbon reservoirs decreases pore-pressure, while it increases effective stress [5, 6]. This physics can cause significant surface subsidence, geological failure, or instability of well assembly. Another instance lies in oceanic gas hydrate deposits, since

depressurization for gas production results in dissociation of the hydrate from solid phase to liquid [7, 8]. Even though geological formation is strong under its virgin condition, the formation becomes highly deformable after the dissociation because geomechanical properties highly depend on saturation of the solid phase [9, 10]. Ultimately, low constant bottom hole pressure with large overburden can cause significant subsidence and well-failure [11]. Similarly, injection of CO_2 induces the uplift of surface due to pressurization of the reservoir [12]. It might also activate the fault nearby, generating induced seismicity [13, 14, 15]. Hydraulic fracturing in tight or shale gas reservoirs or hydro-shearing in geothermal engineering show similar physical processes. Water or gas which is injected into the reservoirs in order to stimulate them creates fractures. As a result, the fracturing increases permeability and productivity, but it can induce micro-earthquakes [16, 17, 18].

Hence, sophisticated measurement and prediction of the effects from coupled fluid flow and geomechanics, otherly named poromechanics for the reservoir simulation, is becoming more critical. Poromechanics is the fundamental framework to describe multi-physical evolving behavior of strongly coupled geomechanics and flow in fully or partially saturated media [19, 20]. Historically for conventional reservoir simulation, geomechanical or thermal effects are considered simply through rock compressibility and thermal expansivity. As stated above, however, precise physics and mathematics are needed for accurate reservoir simulation, calculating fluid and heat flow through unconventional, deformable porous media.

In the view of continuum mechanics, where the representative elementary volume (REV) is homogenized at a certain scale [21], poromechanics is a multiphysics problem of at least two different continua of fluid and solid affecting each other expressed not only with vector fields, such as fields of displacement, velocity, and stress but also with scalar fields, such as fields of temperature, pressure, and so on. It was Terzaghi's brilliant idea [22] dividing the two continua within a system through effective stress and pore pressure,

and Biot expanded the idea of coupling into two to three dimensions with poroelasticity concept [23, 24]. Along with the mathematical implications, the physics beneath them may be much more complicated. Roughly speaking, fluid flow is more localized transient phenomena, as expressed with the mass balance equation, whereas geomechanics has more global scope through quasi-static property with momentum balance equation. Furthermore, in real cases, very complex conditions can exist together such as non-darcy or multiphase flow with phase transitions within multicomponents and elastoplastic behavior, all of which can add up the highly nonlinear effects to the whole system. For example, the crack tip for hydraulic fracturing is where the forefront of fracture propagation is located with moving boundary conditions. The stress localization phenomena at the crack tip is difficult to be addressed mathematically relating to the singularity concept [25, 26].

Even for single phase fluid and simple linear problem with homogeneous, isotropic, and isothermal conditions, there can be many inhibiting issues to circumvent for accurate predictions of the coupling phenomena. For example, there has been an issue with pressure oscillations at an early time of poroelastic simulation [27, 28, 29, 30]. The oscillation, which is similar to the locking phenomena [31], is related to the violation of the well-known Ladyzhenskaya-Babuška-Brezzi (LBB) condition [32] in which a formulation such as both bilinear interpolations using the finite element method (FEM) for displacement and pressure cannot be satisfied for the unique solution. Wan [27] dealt with the problem and proposed a penalty method for a mixed formulation to solve the instability at the early time of simulation for consolidation.

However, the oscillation may also be related to the concept with lack of regularity or smoothness[1] of the solution in numerical analysis, especially at the drainage boundary where abrupt mechanical loading is occuring. This physically interesting phenomena,

[1]Smoothness for a function is generally meant that at least one derivative of the function exists and it is continuous [31].

which has not been thoroughly studied in [27], can also be interpreted in terms of the type solution as instantaneous hyperbolic[2] of partial differential equations (PDEs), which typically discretized with the finite volume method (FVM), such as shocks in wave or fluid dynamics instead of elliptic (for quasi-static geomechanics) or parabolic (for transient fluid flow) property where bounded and smooth solutions can be approximated with piecewise linear or higher interpolation [33, 31]. Vermeer et al. [29] investigated the incompatibility of piecewise linear approximation using FEM and proposed a condition against the unbounded flux (pressure gradient), especially for timestep size during which a certain enough amount of flux can occur for stability at the drainage boundary. The issue is similar to the stress localization problem at fracture tip leading to the singularity since it physically resembles the discontinuous pressure jump at nearly undrained condition, where pressure gradient cannot be approximated using regular FEM.

Apart from the issue, Vijalapura et al. [34] investigated the order of accuracy in the index-1 differential algebraic equations (DAEs), and proposed an operator splitting technique (fractional step method) to achieve higher order of accuracy in time integration. It has been claimed that the decreasing order of accuracy is attributed to the structure of DAEs where the mechanics operator, an elliptic PDE, is working as an algebraic constraint to a system of ordinary differential equations (ODEs) such as the flow operator in case for poromechanics. Although they claimed the higher order of accuracy in time can be achieved through removing the redundancy of algebraic constraint, for coupled flow and geomechanics, however, geomechanics cannot be omitted since there is no redundancy as the case of abrupt loading at the time of initialization for simulation.

On the other hand, in the reservoir simulation community, the fluid flow is typically analyzed with FVM using two-point flux approximation for its spatial discretization with

[2]Where the information traveling speed is limited such as by the wave speed. While elliptic or parabolic PDEs share the infinite speed of information leading to smoothness of solutions, if loading is abrupt at a certain boundary then smoothness of data is required similar to the hyperbolic PDEs [33].

enough accuracy for engineering purposes. In spite of that, sometimes flow approximation needs to be properly enhanced using the multi-point approximation scheme [35, 36]. As for real cases, such as within shale reservoirs, the formation can be highly anisotropic in its permeability and geomechanical properties, partly due to the stimulation by the hydraulic fracturing, or due to the soil or rock property itself. Furthermore, there are chances to solve dynamical full-tensor permeability partly induced from the significant configuration change, which may be attributable to the nonlinear behavior of geomechanics, such as in case for big subsidence. This kind of physics can be categorized as the large deformation system. In this case, the configuration or mesh deformation itself hinders the accuracy of flow. However, the study of sequential algorithms for the coupled problem of large deformation (or finite strain) has little been investigated. For the case, non-linear elasticity must be addressed for its accuracy, and linear assumption is no longer valid. For the accuracy, the objectivity or frame-invariant calculation of the physical properties is needed and also for both geomechanics and fluid flow simulation.

Therefore, even for the simple poromechanics problem, there can be several physical or numerical issues inhibiting accurate calculations, such as displacement and pressure. In this thesis, we are aiming to seek more accurate solutions over those numerous issues inhibiting accurate calculations. For the numerical simulations, we start with simple but straightforward assumptions such as homogeneous and isotropic conditions going toward more complicated conditions as heterogeneous, anisotropic, with the non-linear elastic problem and eventually with real stress data. While pursuing more accurate numerical solutions for several poroelastic problems, we use the fixed-stress split method which is famous for its unconditional stability and convergence property unlike other sequential methods, which has been studied and proved as a rigorous operator splitting scheme [37, 38, 39, 40]. For the simulation, the fixed-stress split method facilitates the use of existing individual flow and geomechanics codes, only by implementing the interface code

between the two simulators. We also adopt the implicit backward Euler method for time discretization. The implicit method is typically used because of its unconditional stability for the stiff problem with an evolving phenomena (e.g., the reaction or diffusion terms within parabolic partial differential equations (PDEs)) [41, 42].

1.2 Thesis Outline

The thesis is composed as follows:

- In the starting chapter, fundamental and introductory Mathematical Formulations for linear poromechanics that are in common for the study are addressed.
- In Spatial Stability, spatial instabilities due to two different conditions are addressed: the LBB condition and the discontinuity in pressure condition at the boundary related to the non-smoothness of physical phenomena such as the abrupt mechanical loading. Dealing with the nearly undrained mechanical response at an early time of simulation with both compressible and incompressible fluids, we compare several spatial discretization methods for mixed formulations, also with two different solution strategies: the monolithic and the fixed-stress split methods.
- In Accuracy in Time Integration, the order of accuracy of numerical solution for poromechanics are addressed.We compare two operator spitting schemes for higher order of accuracy in time integration, motivated by [34]: one is the two-pass algorithm, a symmetric splitting scheme for the flow operator similar to the Strang's splitting scheme, and the other one is based on the spectral deferred correction method.
- In Large Deformation System, we deal with a large deformation system in poroelasticity, where small deformation or infinitesimal transformation–thus linear elasticity–are no longer valid. In this system, the severe mesh deformation and anisotropic properties of geomechanical and fluid flow parameters work against the accuracy.

In order to obtain accurate numerical solutions in this system, we utilize the total Lagrangian method for the configuration change and multi-point flux approximation for the flux approximation.

- In the last chapter as an application, Application with Large Scale Simulation, we perform a large scale simulation with real well data working as constraints for accurate calculations. In order to honor the real well data and avoid the saddle point problem[3] from the constrained mechanics, we use the Uzawa's algorithm for poromechanics to accurately estimate in-situ stress distribution over a domain.

Throughout the study, we find there may exist several different kinds of issues inhibiting accurate calculations for numerical solutions in poromechanics problems. With the fixed-stress split method, using its natural stabilization property and the expandability in code development, we seek not only the feasible but also more precise and accurate numerical solutions in poromechanics.

[3]We deal with this problem in Ch.3 and Ch.6. See more related concept with the compressible and incompressible mechanics or with the inf-sup condition in Appendix B and E.

2. MATHEMATICAL FORMULATIONS

Through this chapter, fundamental equations for poromechanics such as governing equations, constitutive relations, and weak formulations are addressed. Along with them, some basic concepts about numerical solution, which following chapters have in common, are also addressed ahead.

2.1 Well-posed Problem and Numerical Solution

Before seeking a more accurate solution or measuring the accuracy of any approximate or numerical solution, a physical problem expressed with equations (PDE or ODE) needs to be well defined. For example, a PDE can be regarded as well-posed problem in the sense of Jacques Hadamard[1] if the following properties are satisfied:

- A solution exists.
- The solution is unique.
- The solution continuously depends on data, such as initial conditions, boundary conditions, source or sink terms, etc.

If the problem to solve is well-posed, then there exists the unique and true solution. The well-posedness is usually measured through a defined energy type of norm,[2] satisfying its monotonically decreasing property (the concept of contractivity) [33]. In many real physics, however, the true solution, which can be explicitly expressed and obtained through the analytic method, is rare. Thus, we seek the numerical approximate solution, which may not be unique, instead of the true solution by appropriate numerical meth-

[1] A French mathematician (Dec. 1865 - Oct. 1963) who made lots of contributions in mathematics including PDEs, differential geometry and so on.

[2] Defined in a certain metric space that can measure any distance. As an example, the Sobolev space is introduced with it norms in Appendix C.

ods. The appropriate numerical methods basically implies replacing the complex with the simple, including:

- from differential equations to algebraic equations
- from non-linear equations to linear equations
- from high-order systems to low-order systems
- from infinite formulations to finite formulations: dimensions, space, etc.

The accuracy of numerical solutions is important and directly related to the error that is measured with a certain type of norm. The error in numerical methods, in general, is composed of several types [43] such as system, noise, or rounding errors, but in a broad sense, there are only two types: computation error (rounding, truncation) and data error. Among the computation error, rounding error is due to representation in digits related to sufficient number of decimal places. In this study, only truncation error related to algorithm or approximation formula will be addressed.

The truncation error (due to approximating formula) usually can be measured through Taylor expansion as follows:

$$f(x_0 + h) = f(x_0) + f'(x_0)h + \frac{f''(x_0)}{2!}h^2 + \cdots + \frac{f^n(x_0)}{n!}h^n + \frac{f^{n+1}(X)}{(n+1)!}h^{n+1}, \quad (2.1)$$

where x_0 is a certain point with known value of $f(x_0)$, f^n is n-derivative of function f and it is assumed that the function has derivatives of all orders on an interval $I = |x - x_0| < h$. Also X is a value of x among the interval I.

Through the Taylor expansion, the order of accuracy of a numerical solution can be measured. If we approximate a numerical solution as $f(x_0 + h) \approx f(x_0) + f'(x_0)h$, then

the absolute error E will be the rest,

$$E = \frac{f''(x_0)}{2!}h^2 + \cdots + \frac{f^n(x_0)}{n!}h^n + \cdots , \tag{2.2}$$

and from Equation 2.2, it can be expressed $E \sim O(h^2)$, meaning the second order of accuracy.

While assessing a numerical solution, it can be said that the numerical solution is approaching to the true solution when the size of discretization or mesh, expressed as h in Equation 2.1 and 2.2, is reduced and approaching to zero. This is the convergence property of the numerical solution. And an algorithm or formula approximating an original form is said to be consistent if it converges to the to original form. For example, a finite-element discretization of a PDE is consistent if it converges to the original PDE, as grid spacing and time discretization h goes to zero. There is another concept about the stability of a numerical solution, meaning that errors from any source will not grow but it is bounded with time. Then by Lax equivalence theorem [44], for consistent formulation, if and only if (necessary and sufficient) the stability is satisfied, the numerical solution has convergence and vice versa is true.

2.2 Strong Form with Governing Equations for Poromechanics

We adopt the mathematical model based on the poroelasticity and poroelastoplasticity theories [45]. The physical problems in this study are in common that they are assumed to be isothermal single-phase flow, small deformation (i.e., infinitesimal transformations), isotropic geomaterial, and no stress-dependence of flow properties, except for Ch.3 where small deformation, isotropic geomaterial and stress-dependence of flow properties are no longer valid. We will deal with the specific formulations that belong to large deformation systems in Ch.3.

The governing equations for coupled flow and geomechanics are derived from the mass

balance and linear momentum balance, respectively. Under the quasi-static assumption, the governing equation for geomechanics can be written as

$$\text{Div}\boldsymbol{\sigma} + \rho_b \boldsymbol{g} = \mathbf{0}, \tag{2.3}$$

where $\text{Div}(\cdot)$ is the divergence operator, $\boldsymbol{\sigma}$ is the Cauchy total stress tensor, $\boldsymbol{g}$ is the gravity vector, $\rho_b = \phi\rho_f + (1-\phi)\rho_s$ is the bulk density, ρ_f is fluid density, and ρ_s is the density of the solid phase. ϕ is the true porosity, defined as the ratio of the pore volume to the bulk volume in the deformed configuration. In this study, tensile stress and strain are positive.

For flow, we have the governing equation as follows.

$$\frac{dm}{dt} + \text{Div}\boldsymbol{w} = \rho_{f,0} f, \tag{2.4}$$

where $\boldsymbol{w}$ is the fluid mass flux (fluid mass flow rate per unit area and time), and f is a volumetric source term. The subscript 0 means reference state.

Flow and geomechanics are coupled through the constitutive equation by Biot's theory [45, 23, 24, 46], which relates mass and total stress to pressure and strain, expressed as

$$\boldsymbol{\sigma} - \boldsymbol{\sigma}_0 = \mathbf{C}_{dr} : \boldsymbol{\varepsilon} - b(p - p_0)\mathbf{1}, \tag{2.5}$$

$$\frac{1}{\rho_{f,0}}(m - m_0) = b\varepsilon_v + \frac{1}{M}(p - p_0), \tag{2.6}$$

where $\mathbf{C}_{dr}$ is the rank-4 drained elasticity tensor, $\mathbf{1}$ is the rank-2 identity tensor, p is fluid pressure and m is fluid mass per unit bulk volume. M and b are the Biot modulus and

coefficient, respectively, and take the forms as follows [45].

$$\frac{1}{M} = \phi_0 c_f + \frac{b - \phi_0}{K_s}, \tag{2.7}$$

$$b = 1 - \frac{K_{dr}}{K_s}, \tag{2.8}$$

where c_f is the fluid compressibility $(1/K_f)$, K_f is the bulk modulus of the fluid, K_s is the bulk modulus of the solid grain, and K_{dr} is the drained bulk modulus. $\boldsymbol{\varepsilon}$ is the linearized strain tensor under the assumption of infinitesimal transformation:

$$\boldsymbol{\varepsilon} = \mathbf{Grad}^s \boldsymbol{u} = \frac{1}{2}(\mathbf{Grad}\boldsymbol{u} + \mathbf{Grad}^t \boldsymbol{u}), \tag{2.9}$$

which can be decomposed into the volumetric and deviatoric parts, as follows.

$$\boldsymbol{\varepsilon} = \frac{1}{3}\varepsilon_v \mathbf{1} + \boldsymbol{e}, \tag{2.10}$$

$$\boldsymbol{\sigma} = \sigma_v \mathbf{1} + \boldsymbol{s}, \tag{2.11}$$

where $\varepsilon_v = \mathrm{tr}\boldsymbol{\varepsilon}$ is the volumetric strain (the trace of the strain tensor), $\boldsymbol{e}$ is the deviatoric part of the strain tensor, $\sigma_v = \frac{1}{3}\mathrm{tr}\boldsymbol{\sigma}$ is the volumetric (mean) total stress, and $\boldsymbol{s}$ is the deviatoric total stress tensor.

Using Equation 2.6, Equation 2.4 can be expressed in terms of pressure and volumetric strain:

$$\frac{1}{M}\frac{\partial p}{\partial t} + b\frac{\partial \varepsilon_v}{\partial t} + \mathrm{Div}\boldsymbol{v} = f, \tag{2.12}$$

where $\boldsymbol{v} = \boldsymbol{w}/\rho_{f,0}$ is the fluid velocity relative to the solid skeleton, described by Darcy's law:

$$\boldsymbol{v} = -\frac{\boldsymbol{k}_p}{\mu}(\mathbf{Grad}p - \rho_f \boldsymbol{g}), \tag{2.13}$$

where $\boldsymbol{k}_p$ is the symmetric positive definite absolute permeability tensor, and μ is fluid viscosity.

We then specify initial and boundary conditions to complete the mathematical problem. The pressure and total stress are specified at initial time as $p|_{t=0} = p_0$ and $\boldsymbol{\sigma}|_{t=0} = \boldsymbol{\sigma}_0$. The initial stress field should satisfy mechanical equilibrium, and reflect the history of stress paths. The initial displacements and strains are, by definition, equal to zero. For the boundary condition of flow, we have $p = \bar{p}$ (prescribed pressure) on Γ_p, and $\boldsymbol{v} \cdot \boldsymbol{n} = \bar{v}$ (prescribed volumetric flux) on Γ_v, where $\boldsymbol{n}$ is the outward unit normal to the boundary, $\partial\Omega$. For well-posedness, we take $\Gamma_p \cap \Gamma_v = \emptyset$, and $\Gamma_p \cup \Gamma_v = \partial\Omega$. For the boundary condition of geomechanics, we have $\boldsymbol{u} = \bar{\boldsymbol{u}}$ (prescribed displacement) on Γ_u and $\boldsymbol{\sigma} \cdot \boldsymbol{n} = \bar{\boldsymbol{t}}$ (prescribed traction) on Γ_σ. For well-posedness, we also take $\Gamma_u \cap \Gamma_\sigma = \emptyset$, and $\Gamma_u \cup \Gamma_\sigma = \partial\Omega$.

2.3 Weak Form with Discretization in Space

We partition the domain into non-overlapping elements (grid blocks), $\Omega = \cup_{j=1}^{n_{\text{elem}}} \Omega_j$, where n_{elem} is the number of elements. Then, using Galerkin's method [31], the discrete approximation of the weak form of Equations 2.3 and 2.4 becomes: Find $(\boldsymbol{u}_h, p_h) \in \mathcal{U}_h \times \mathcal{Q}_h$ such that

$$\int_\Omega \mathbf{Grad}^s \boldsymbol{\eta}_h : \boldsymbol{\sigma}_h \, d\Omega = \int_\Omega \boldsymbol{\eta}_h \cdot \rho_b \boldsymbol{g} \, d\Omega + \int_{\Gamma_\sigma} \boldsymbol{\eta}_h \cdot \bar{\boldsymbol{t}} \, d\Gamma \quad \forall \boldsymbol{\eta}_h \in \mathcal{U}_{h,0}, \tag{2.14}$$

$$\frac{1}{\rho_{f,0}} \int_\Omega \varphi_h \frac{\partial m_h}{\partial t} \, d\Omega + \int_\Omega \varphi_h \text{Div} \boldsymbol{v}_h \, d\Omega = \int_\Omega \varphi_h f \, d\Omega, \quad \forall \varphi_h \in \mathcal{Q}_{h,0}, \tag{2.15}$$

where the subscript h indicates discrete approximation in space. $\mathcal{U}$, $\mathcal{Q}$, $\mathcal{U}_0$ and $\mathcal{Q}_0$ are the functional spaces of $\boldsymbol{u}$, p, $\boldsymbol{\eta}$ and φ, respectively, and $\mathcal{U}_h$, $\mathcal{U}_{h,0}$, $\mathcal{Q}_h$ and $\mathcal{Q}_{h,0}$ are the corresponding finite-dimensional subspaces[3].

[3]For clarity, we derive the linearized form for the Q1Q1 space (interpolation with the bilinear function for both displacement and pressure) from the strong form and the weak form for a 1D problem in Appendix A.

Different functional spaces of $\boldsymbol{u}_h$ and p_h yield different finite elements. For example, the Q2Q1 element takes

$$\mathcal{U}_h \times \mathcal{Q}_h := \left\{ (\boldsymbol{u}_h, p_h) \in \mathrm{R}^{\mathrm{n_{dim}}} \times \mathrm{R} : u_{hi} \in H^2(\Omega), \boldsymbol{u}_h = \bar{\boldsymbol{u}}_h \text{ on } \Gamma_u,\ p_{hi} \in H^1(\Omega), \right. \\ \left. p_h = \bar{p}_h \text{ on } \Gamma_p \right\}, \tag{2.16}$$

$$\mathcal{U}_{h,0} \times \mathcal{Q}_{h,0} := \left\{ (\boldsymbol{\eta}_h, \varphi_h) \in \mathrm{R}^{\mathrm{n_{dim}}} \times \mathrm{R} : \eta_{hi} \in H_0^2(\Omega), \boldsymbol{\eta}_h = \mathbf{0} \text{ on } \Gamma_u,\ \varphi_{hi} \in H_0^1(\Omega), \right. \\ \left. \varphi_h = 0 \text{ on } \Gamma_p \right\}, \tag{2.17}$$

where n_{dim} is the space dimension of the domain Ω. u_{hi} and η_{hi} are the components of $\boldsymbol{u}_h$ and $\boldsymbol{\eta}_h$, respectively. H^k denotes a Sobolev space[4] of degree of k. For the Q1Q1 element, H^2 of both u_{hi} and η_{hi} in Equations 2.16 and 2.17 are changed to H^1. Similarly, for the Q1P0 element, H^1 of both p_h and φ_h in Equations 2.16 and 2.17 are changed to L^2.

The pressure and displacement fields are approximated as follows:

$$\boldsymbol{u}_h = \sum_a \eta_a \boldsymbol{u}_a, \quad p_h = \sum_i \varphi_i p_i, \tag{2.18}$$

where $\boldsymbol{u}_a$ is the displacement vectors at the element nodes, and p_i is the pressures at the element nodes (FEM) or elements (FVM). Precisely, for FVM of flow, Equation 2.15 can be interpreted as a mass conservation statement element-by-element, changed to

$$\frac{1}{\rho_{f,0}} \int_{\Omega_i} \frac{\partial m_h}{\partial t}\, d\Omega_i + \int_{\Omega_i} \mathrm{Div} \boldsymbol{v}_h\, d\Omega_i = \int_{\Omega_i} f\, d\Omega_i, \tag{2.19}$$

where the second term can be integrated by parts to arrive at the sum of integral fluxes,

[4]See Appendix C.

$V_{h,ij}$, between element i and its adjacent elements j:

$$\int_{\Omega_i} \mathrm{Div}\boldsymbol{v}_h \, d\Omega_i = \int_{\partial\Omega_i} \boldsymbol{v}_h \cdot \boldsymbol{n}_i \, d\Gamma = \sum_{j=1}^{n_{\text{face}}} \int_{\Gamma_{ij}} \boldsymbol{v}_h \cdot \boldsymbol{n}_i \, d\Gamma = \sum_{j=1}^{n_{\text{face}}} V_{h,ij}, \tag{2.20}$$

where n_i is the outward unit normal vector of the boundary of element i. n_{face} is the number of interfaces at an element. The inter-element flux can be evaluated using a two-point or a multipoint flux approximation [35]. Then, the semi-discrete coupled equations are written as

$$\int_{\Omega} \boldsymbol{B}_a^T \boldsymbol{\sigma}_h \, d\Omega = \int_{\Omega} \eta_a \rho_b \boldsymbol{g} \, d\Omega + \int_{\Gamma_\sigma} \eta_a \bar{\boldsymbol{t}} \, d\Gamma \quad \forall a = 1, \ldots, n_{\text{node}}, \tag{2.21}$$

$$\int_{\Omega_i} \frac{1}{M} \frac{\partial P_i}{\partial t} \, d\Omega + \int_{\Omega_i} b \frac{\partial \varepsilon_v}{\partial t} \, d\Omega + \int_{\partial\Omega_i} \boldsymbol{v}_h \cdot \boldsymbol{n}_i \, d\Gamma = \int_{\Omega_i} f \, d\Omega, \quad \forall i = 1, \ldots, n_{\text{elem}}, \tag{2.22}$$

where n_{elem} and n_{node} are the number of the elements and nodes. The matrix $\boldsymbol{B}_a$ is the linearized strain operator, which in 2D takes the form

$$\boldsymbol{B}_a = \begin{bmatrix} \partial_x \eta_a & 0 \\ 0 & \partial_y \eta_a \\ \partial_y \eta_a & \partial_x \eta_a \end{bmatrix}. \tag{2.23}$$

The stress and strain tensors are expressed in compact engineering notation [31]. For example, in 2D,

$$\boldsymbol{\sigma}_h = \begin{bmatrix} \sigma_{h,xx} \\ \sigma_{h,yy} \\ \sigma_{h,xy} \end{bmatrix}, \qquad \boldsymbol{\varepsilon}_h = \begin{bmatrix} \varepsilon_{h,xx} \\ \varepsilon_{h,yy} \\ 2\varepsilon_{h,xy} \end{bmatrix}. \tag{2.24}$$

The stress–strain relation for linear poroelasticity takes the form:

$$\boldsymbol{\sigma}_h = \boldsymbol{\sigma}'_h - bp_h\mathbf{1}, \qquad \delta\boldsymbol{\sigma}'_h = \boldsymbol{D}\delta\boldsymbol{\varepsilon}_h, \tag{2.25}$$

where $\boldsymbol{\sigma}'$ is the effective stress tensor, and $\boldsymbol{D}$ is the elasticity matrix which, for 2D plane strain conditions, reads:

$$\boldsymbol{D} = \frac{E(1-\nu)}{(1+\nu)(1-2\nu)} \begin{bmatrix} 1 & \frac{\nu}{1-\nu} & 0 \\ \frac{\nu}{1-\nu} & 1 & 0 \\ 0 & 0 & \frac{(1-2\nu)}{2(1-\nu)} \end{bmatrix}, \tag{2.26}$$

where E is the Young modulus, and ν is the Poisson ratio.

2.4 The DAEs of Index-1 System

Before moving on to the time discretized system, the discretized governing equations (Equation 2.21 and 2.22) can be expressed with the primary variables of the spatially-only-not-temporally-yet discretized vectors, $\boldsymbol{U}$ and $\boldsymbol{P}$ for displacement and pressure, respectively.

Since Equation 2.22 has a time derivative term, it leads to a system of ODE[5]. Then Equation 2.21 takes the role of non-differential contraint for the whole system, which can be expressed as:

$$\begin{cases} \Xi : \mathbf{0} = g(\boldsymbol{U}, \boldsymbol{P}, t), \\ \Phi : \dot{\boldsymbol{P}} = f(\dot{\boldsymbol{U}}, \boldsymbol{P}, t), \end{cases} \tag{2.27}$$

where Ξ and Φ represent operators for spatially discretized geomechanics and flow, respec-

[5]By following the method of line (MOL) approach [47, 48], through which a PDE is taking the form of a sytem of ODEs.

tively. Note that if $\dot{\boldsymbol{U}}$ in Φ is explicitly given or prescribed, Φ is showing pure ODEs with variable $\boldsymbol{P}$. Thus Equation 2.27 has the form of the semi-explicit DAEs index-1 system. According to [47], the index[6] of the DAEs is the number of the time derivation needed for the constraint equation to force the system to have the same form as the implicit ODE system.

2.5 Time Discretization and Solution Strategy

There are several coupling methodologies or solution strategies in petroleum reservoir engieering such as one way or explicit coupling which is a type of sequential and iterative coupling but where only one iteration per timestep is performed [4]. For more accurately addressing and solving the multiphysically coupled and transient problem including poromechanics [20, 41], however, broadly two approaches exist in terms of numerical integration with a time stepping or marching algorithm: one is the monolithic or fully-coupled method, and the other one is the sequential or iterative method.

- the monolithic (or fully implicit) approach
- the sequential (or iterative) approach

The monolithic approach solves all variables simultaneously, applying the same scheme (e.g., the implicit scheme) to all sub-equations for time stepping (e.g., the fully implicit) and providing unconditional stability. However, it requires effort of code development and significant computational cost. On the other hand, the sequential method can be used to overcome this drawback of the monolithic method. It solves one of the variables through a partition and then moves to the next variable until the convergence is reached among the variables through iterations. If fully iterated, the sequential method converges to the monolithic method and both methods are mathematically equivalent [4, 37, 38]. This type

[6] See Appendix D for the concept.

of approach, called staggered or partitioned method, has been studied in many engineering fields including structural analysis and fluid dynamics [49]. Since the sequential method may suffer the stability issue, however, many studies have been done to find reliable sequential methods including operator splitting schemes [50, 51, 52].

A fully discretized system of equations are obtained by discretization in time. In this thesis, the backward Euler method is used for time discretization, typically used in reservoir simulation. Before deriving the fully discrete system, we state solution strategies above in solving the coupled fluid flow and geomechanics problem: the monolithic and the sequential scheme in poromechanics. There are several sequential methods that have been used for poromechanics problems. Among them, we employ the fixed-stress split, because it is unconditionally stable and convergent with high accuracy[7] [53, 38].

2.5.1 Monolithic scheme

The monolithic scheme, also called the fully coupled method in poromechanics, solves the equations of flow and mechanics simultaneously, typically using the Newton–Raphson method [54, 20]. Let us denote by $\mathcal{A}$ the operator of the original problem (Equations 2.3 and 2.4). The discrete approximation of this operator corresponding to the monolithic scheme can be represented as [53, 38]:

$$\begin{bmatrix} \boldsymbol{u}^n \\ \boldsymbol{p}^n \end{bmatrix} \xrightarrow{\mathcal{A}_{\text{mn}}} \begin{bmatrix} \boldsymbol{u}^{n+1} \\ \boldsymbol{p}^{n+1} \end{bmatrix}, \quad \text{where} \quad \mathcal{A}_{\text{mn}} : \begin{cases} \text{Div}\boldsymbol{\sigma} + \rho_b \boldsymbol{g} = \boldsymbol{0}, \\ \dot{m} + \text{Div}\boldsymbol{w} - \rho_{f,0} f = 0, \end{cases} \tag{2.28}$$

where $\dot{(\,)}$ denotes time derivative and the superscript n denotes time level t_n.

Using a backward Euler time discretization in Equations 2.21 and 2.22, the residual

[7] Given the limited computational resources, there are two approaches possible: the staggered method with a small timestep size and the iterative fully-coupled method with a large timestep size. The accuracy between the two approaches is still arguable. When the timestep size is refined, the staggered fixed-stress method can reduce both the time discretization error (the first-order) and the sequential error simultaneously. Thus we employ the staggered fixed-stress split method in this study.

form of the fully-discrete coupled equations is:

$$\boldsymbol{R}_a^u = \int_\Omega \boldsymbol{B}_a^T \boldsymbol{\sigma}_h^{n+1}\, d\Omega - \int_\Omega \eta_a \rho_b^{n+1} \boldsymbol{g}\, d\Omega - \int_{\Gamma_\sigma} \eta_a \bar{\boldsymbol{t}}^{n+1}\, d\Gamma \quad \forall a = 1, \ldots, n_{\text{node}}, \tag{2.29}$$

$$\begin{aligned} R_i^p = &\int_{\Omega_i} \frac{1}{M}(P_i^{n+1} - P_i^n)\, d\Omega + \int_{\Omega_i} b(\varepsilon_v^{n+1} - \varepsilon_v^n)\, d\Omega + \Delta t \int_{\partial\Omega_i} \boldsymbol{v}_h^{n+1} \cdot \boldsymbol{n}_i\, d\Gamma \\ &- \Delta t \int_{\Omega_i} f^{n+1}\, d\Omega \quad \forall i = 1, \ldots, n_{\text{elem}}, \end{aligned} \tag{2.30}$$

where $\boldsymbol{R}_a^u$ and R_i^p are the residuals for geomechanics and flow, respectively. The set of Equations 2.29 and 2.30 is to be solved for displacements and pressures. Given an approximation of the solution $(\boldsymbol{u}^{n+1}, \boldsymbol{p}^{n+1})$, Newton's method yields the following system of equations:

$$\underbrace{\begin{bmatrix} \boldsymbol{K} & -\boldsymbol{L}^T \\ \boldsymbol{L} & \boldsymbol{F} \end{bmatrix}}_{\boldsymbol{J}} \begin{bmatrix} \delta\boldsymbol{u} \\ \delta\boldsymbol{p} \end{bmatrix}^n = - \begin{bmatrix} \boldsymbol{R}^u \\ \boldsymbol{R}^p \end{bmatrix}^n, \tag{2.31}$$

where $\delta(\cdot)^n = (\cdot)^{n+1} - (\cdot)^n$. $\boldsymbol{J}$ is the Jacobian matrix, $\boldsymbol{K}$ is the stiffness matrix and $\boldsymbol{L}$ is the coupling poromechanics matrix. $\boldsymbol{F} = \boldsymbol{Q} + \Delta t \boldsymbol{T}$, which is the flow matrix, where $\boldsymbol{Q}$ is the compressibility matrix and $\boldsymbol{T}$ is the transmissibility matrix. The entries of sub-matrices of the Jacobian matrix are:

$$\boldsymbol{K} = \boldsymbol{k}_{ab} = \int_\Omega \boldsymbol{B}_a^T \boldsymbol{D} \boldsymbol{B}_b\, d\Omega, \tag{2.32}$$

$$\boldsymbol{L} = l_{ib} = \int_\Omega \varphi_i b (\mathbf{Grad}\eta_b)^T\, d\Omega, \tag{2.33}$$

$$\boldsymbol{Q} = q_{ij} = \int_\Omega \varphi_i M^{-1} \varphi_j\, d\Omega. \tag{2.34}$$

The monolithic scheme computes the Jacobian matrix $\boldsymbol{J}$, and determines $\delta\boldsymbol{u}$ and $\delta\boldsymbol{p}$ simultaneously. In this study, we assume that a direct solver can be used to solve $\boldsymbol{J}$ in the

monolithic method.

2.5.2 Sequential scheme: Fixed-stress split

In the fixed-stress sequential method, the flow problem is solved first while fixing the rate of the total stress ($\delta\dot{\sigma} = 0$). The original operator is then split as follows:

$$\begin{bmatrix} \boldsymbol{u}^n \\ \boldsymbol{p}^n \end{bmatrix} \xrightarrow{\mathcal{A}^p_{ss}} \begin{bmatrix} \boldsymbol{u}^* \\ \boldsymbol{p}^{n+1} \end{bmatrix} \xrightarrow{\mathcal{A}^u_{ss}} \begin{bmatrix} \boldsymbol{u}^{n+1} \\ \boldsymbol{p}^{n+1} \end{bmatrix}, \quad \text{where} \quad \begin{cases} \mathcal{A}^p_{ss} : \dot{m} + \text{Div}\boldsymbol{w} = \rho_{f,0} f,\ \delta\dot{\sigma} = 0, \\ \mathcal{A}^u_{ss} : \text{Div}\boldsymbol{\sigma} + \rho_b \boldsymbol{g} = \boldsymbol{0},\ p:\ \text{prescribed}. \end{cases} \tag{2.35}$$

The initial conditions of $\mathcal{A}^p_{ss}$ are determined from the initial time conditions of the original coupled problem, which satisfy

$$\text{Div}\dot{\boldsymbol{\sigma}}_{t=0} = \boldsymbol{0}\,, \quad \text{Div}\boldsymbol{\sigma}_{t=0} + \rho_b \boldsymbol{g} = \boldsymbol{0}. \tag{2.36}$$

Then, the fully discrete system becomes

$$\begin{bmatrix} \boldsymbol{K} & -\boldsymbol{L}^T \\ \boldsymbol{L} & \boldsymbol{F} \end{bmatrix} \begin{bmatrix} \delta\boldsymbol{u} \\ \delta\boldsymbol{p} \end{bmatrix}^n \rightarrow \begin{bmatrix} \boldsymbol{K} & -\boldsymbol{L}^T \\ \boldsymbol{0} & \boldsymbol{F}+\boldsymbol{S} \end{bmatrix} \begin{bmatrix} \delta\boldsymbol{u} \\ \delta\boldsymbol{p} \end{bmatrix}^n - \begin{bmatrix} \boldsymbol{0} & \boldsymbol{0} \\ -\boldsymbol{L} & \boldsymbol{S} \end{bmatrix} \begin{bmatrix} \delta\boldsymbol{u} \\ \delta\boldsymbol{p} \end{bmatrix}^{n-1}, \tag{2.37}$$

where $\boldsymbol{S}$ is calculated by fixing the rate of mean stress and by introducing the term b^2/K_{dr} locally in each element [37, 39]. According to [37], [38], and [40], the fixed stress split provides unconditional stability and convergence in time, while the fixed-strain and drained splits are neither unconditionally stable nor convergent. The undrained split is known to be unconditionally stable but not convergent when incompressible fluid exists.

Also note that the fixed stress split can be applied to a preconditioner of the monolithic

method [39, 55]. Then, Equation 2.37 can be modified as

$$\begin{bmatrix} \boldsymbol{K} & -\boldsymbol{L}^T \\ \boldsymbol{L} & \boldsymbol{F} \end{bmatrix} \begin{bmatrix} \delta\boldsymbol{u} \\ \delta\boldsymbol{p} \end{bmatrix}^{n,(k)} \rightarrow \begin{bmatrix} \boldsymbol{K} & -\boldsymbol{L}^T \\ \boldsymbol{0} & \boldsymbol{F}+\boldsymbol{S} \end{bmatrix} \begin{bmatrix} \delta\boldsymbol{u} \\ \delta\boldsymbol{p} \end{bmatrix}^{n,(k)} - \begin{bmatrix} \boldsymbol{0} & \boldsymbol{0} \\ -\boldsymbol{L} & \boldsymbol{S} \end{bmatrix} \begin{bmatrix} \delta\boldsymbol{u} \\ \delta\boldsymbol{p} \end{bmatrix}^{n,(k-1)}, \quad (2.38)$$

where (k) denotes the iteration level.

3. SPATIAL STABILITY

3.1 Introduction for Spatial Stability

Numerical simulation is an effective tool to predict behavior of the aforementioned complex coupled physical processes. For simple consoliation model such as Terzaghi's problem [22] which is a representative linear poroelastic problem in coupled flow and geomechanics, the approximation in space, geomechanics is typically done with the finite element method (FEM) with virtual work with variational fomulation [31], whereas the fluid flow espeically in reservoir simulation community is typically using the finite volume method (FVM) for its structural mass conserving property. In cases, the finite element method (FEM) also is frequently employed to solve both coupled flow and geomechanics numerically [54, 56]. However, from the previous studies, the equal order approximation for pressure and displacement might cause numerical instability in space [29, 57, 27, 28]. According to [29], when linear interpolation is used for both pressure and displacement of the one-dimensional (1D) consolidation problem, severe oscillation of pressure can occur at early times. They then found a lower bound of time step size for spatial stability. Murad and Loula [57, 58] analyzed numerical instability of the consolidation problem with incompressible fluid, and claimed that the instability is caused by violation of the well-known LBB condition, also called the inf-sup condition [32]. They showed that the mathematical problem at early times has the same type of Stoke's problem[1]. Because flow is almost in undrained condition at early times, the coupled flow-mechanics problem converges to an undrained mechanical problem[2]. When both the fluid and the solid grains are incompressible, the undrained bulk modulus is infinite, which results in an incompressible system. Hence, the inf-sup condition must be satisfied to obtain stable

[1] See Appendix E.
[2] See Appendix B for the detail.

numerical solutions. However, the equal-order approximations of pressure and displacement (e.g., piecewise linear interpolation) do not satisfy the inf-sup condition, causing numerical instability in space [57, 31].

Several studies have been done in order to remove the instability by introducing a numerical/artificial stabilizer with the monolithic approach (i.e., fully implicit method) [27, 28, 59]. Although the stabilization methods can alleviate spurious oscillation, more investigation is still required to understand the causes of the oscillation, the impacts of various spatial discretizations, and the sequential approach on the oscillation. For example, the oscillation still exists at the drainage boundary, when the fluid is compressible, even though the space discretization satisfies the inf-sup condition [29, 28]. For a slightly compressible fluid, at early times, the coupled flow-geomechanics problem reduces to a compressible mechanical problem, not requiring the inf-sup condition.

The objectives of this chapter are to perform in-depth analysis of the instability, to find the different characteristics of monolithic and sequential methods with the mixed discretization, and to show numerical results from various scenarios. The instability originates from the two parts: the discontinuity of pressure at the drainage boundary and the violation of the inf-sup condition due to incompressibility. The instability at early times can result from instantaneous mechanical loading, which causes discontinuity of pressure at the drainage boundary. Hence, this physics motivates the mixed finite element and finite volume methods for geomechanics and flow [37, 38], respectively, where we employ the piece-wise linear (or high-order) interpolation for displacement and the piece-wise constant interpolation for pressure. In addition, a finite element pair that satisfies the inf-sup condition needs to be used, for example, biquadratic and bilinear interpolations for displacement and pressure, respectively [31]. Nordbotten [60] recently claims that piecewise linear finite volume discretization for both flow and geomechanics can satisfy the inf-sup condition, but it needs to be more investigated for the case of the pressure discontinuity of

consolidation problems. Thus, we will study numerical behavior for various mixed finite element methods, specifically, Q1Q1, Q1P0, Q2Q1, and Q2P0, where the former Q is used for displacement using the standard finite element method (FEM), while the latter Q or P is used for pressure, using the FEM or finite volume method (FVM) with piecewise constant interpolation of pressure, respectively. The number of Q/P indicates the order of the basis (shape) function (e.g., Q2, Q1, and P0 for piecewise biquadratic, piecewise bilinear, piecewise constant interploations, respectively).

Furthermore, we will investigate the impacts of the sequential approach (i.e., the fixed-stress sequential method [38]) on the pressure field at early times, comparing it with the monolithic method. In previous studies, the fixed-stress method has mainly been studied for the case where FVM and FEM are employed for flow and geomechanics, respectively (i.e., Q1P0). For more in-depth analysis, in this study, we will compare the fixed-stress sequential method with the monolithic method for the Q1Q1, Q2Q1, Q1P0, and Q2P0, investigating their numerical characteristics of spatial stability.

From a-priori analysis and numerical experiments of this study, we will obtain the following findings. First, Q1P0 and Q2P0 yield stability at early times for the consolidation problems, while Q1Q1 and Q2Q1 show spatial oscillation near the drainage boundary, regardless of fluid compressibility. However, even for the Q1Q1 element pair that exhibits severe oscillation, the fixed-stress sequential method can effectively stabilize the oscillation without an artificial stabilizer. For the incompressibility, which might require the inf-sup condition, the fixed-stress sequential method can yield stability for all the element choices, while the monolithic method can cause severe instability, except the Q2Q1 pair known to satisfy the inf-sup condition. The stabilized monolithic method in this study does not yield good accuracy although it alleviates instability slightly. Thus, the fixed-stress method can be more stable in space for the cases where the monolithic method causes severe spatial oscillation, implying that the fixed-stress method can also be a good

preconditioner for the monolithic method.

3.2 Stability in Space

There are two main causes for spatial numerical instability for consolidation problems: discontinuity of pressure at the drainage boundary and violation of the inf-sup condition induced by incompressibility.

3.2.1 Discontinuity of pressure for the consolidation problems

Vermeer et al. [29] analyzed instability for linear interpolation functions for pressure and displacement with the nodal based finite-element method in the one-dimensional consolidation problem for single-phase flow (i.e., Terzaghi's problem). In this case, the flow equation is written as

$$\frac{\partial p}{\partial t} + \omega \frac{\partial \sigma_{xx}}{\partial t} = c_v \frac{\partial^2 p}{\partial x^2}, \;\; c_v = \frac{k K_c}{\mu}\omega, \;\; \omega = \frac{1/K_c}{1/K_c + \phi c_f}, \;\; K_c = \frac{E(1-\nu)}{(1+\nu)(1-2\nu)}, \tag{3.1}$$

where K_c is the constrained modulus. When the initial pressure is zero, the resulting system of equations can be written as [29]

$$\begin{bmatrix} 1-2b^* & b^* & & & & \\ b^* & 1-2b^* & b^* & & & \\ & \cdots & \cdots & \cdots & & \\ & & \cdots & \cdots & \cdots & \\ & & & b^* & 1-2b^* \end{bmatrix} \begin{bmatrix} \Delta p_1 \\ \Delta p_2 \\ \cdots \\ \cdots \\ \Delta p_{n-1} \end{bmatrix} = \omega \Delta \sigma \begin{bmatrix} 1 \\ 1 \\ \cdots \\ \cdots \\ 1 \end{bmatrix}, \tag{3.2}$$

where

$$b^* = \frac{1}{6} - \alpha \frac{c_v \Delta t}{h^2}, \tag{3.3}$$

where α is a parameter from time discretization (e.g., $\alpha = 1.0$ for the backward Euler method). According to [29], the necessary and sufficient conditions for stability in space is

$$b^* \leq 0, \tag{3.4}$$

which yields

$$\Delta t \geq \frac{1}{6}\frac{h^2}{\alpha c_v}. \tag{3.5}$$

The lower bound on the time step size implies that sufficient pressure diffusion is required to obtain a smooth distribution of pressure that can be interpolated by using piecewise polynomials.

When we use the quadratic interpolations for both displacement and pressure, we have

$$\begin{bmatrix} a_{11} & a_{12} & & & & \\ a_{21} & a_{22} & a_{23} & a_{24} & & \\ & \cdots & \cdots & \cdots & & \\ & & \cdots & \cdots & \cdots & \\ & & & a_{2n-12n-2} & a_{2n-12n-1} \end{bmatrix} \begin{bmatrix} \Delta p_1 \\ \Delta p_2 \\ \cdots \\ \cdots \\ \Delta p_{2n-1} \end{bmatrix} = \omega\Delta\sigma \begin{bmatrix} 2/3 \\ 1/3 \\ \cdots \\ 1/3 \\ 2/3 \end{bmatrix}, \tag{3.6}$$

$$a_{11} = a_{2n-12n-1} = \frac{8}{15} + \frac{16c\Delta t}{3h^2},$$
$$a_{12} = a_{21} = a_{23} = a_{2n-22n-1} = \frac{1}{15} - \frac{8c\Delta t}{3h^2},$$
$$a_{22} = \frac{4}{15} + \frac{14c\Delta t}{3h^2},\ a_{24} = \frac{1}{15} + \frac{c\Delta t}{3h^2}.$$

from which the condition of the spatial stability becomes

$$\Delta t \geq \frac{1}{10}\frac{h^2}{\alpha c_v}. \tag{3.7}$$

Note that Equations 3.5 and 3.7 are not new but found by Vermeer et al. [29]. The quadratic interpolation provides a less restricted time step size than the linear interpolation. And the analysis is consistent with the following. Ženišek [61] showed the error estimates for the two-dimensional consolidation problem with an incompressible fluid as

$$\|p - p_h\|_{l_2} + \|\mathbf{u}^m - \mathbf{u}_h^m\|_1 \leq C\left(h^n \Delta t^{-1/2} \left\|\mathbf{u}^0\right\|_{n+1} + h^n + \Delta t\right), \tag{3.8}$$

where $p \in H^n$, $\mathbf{u} \in [H^{n+1}]^2$, C is a constant independent of Δt and h, and $\mathbf{u}^m = \mathbf{u}(t = t_m)$. $\|\cdot\|_{l_2}$ and $\|\cdot\|_k$ are defined as

$$\|f\|_{l_2}^2 = \Delta t \sum_{i=1}^{m} \left\|f^i\right\|_0^2, \;\; \|f\|_k^2 = \sum_{a=k} \|D^a f\|_{L^2}^2, \tag{3.9}$$

where $D^a f$ is the a^{th} order spatial derivative of f. From the first term of the right hand side in Equation 3.8, we identify the lower bound on the time step size.

In this study, we further extend investigation of spatial stability, introducing different interpolations for displacement and pressure, and find additional the conditions of space stability. Specifically, when we use the mixed finite element/finite volume method, pressure is in L^2 space, being piecde-wise constant, which allows for jumps in the pressure field, such as discontinuity at the drainage boundary. Taking the procedure similar to Equation 3.2, we find that b^* from the piecewise constant finite-volume method for flow is obtained as

$$b^* = -\alpha \frac{c_v \Delta t}{h^2}, \tag{3.10}$$

which satisfies the stability condition in [29], Equation 3.4. This implies no restriction on the time step size for spatial stability. Hence, there is no spurious spatial instability around the drainage boundary.

On the other hand, when we take quadratic interpolation for displacement and linear interpolation for pressure with $\alpha = 1.0$, the right hand side vector of Equation 3.2 is changed to $\omega\Delta\sigma\left[4/3, 2/3, \cdots, 2/3, 4/3\right]^T$ with

$$b^* = \frac{1}{6} - \frac{4c_v\Delta t}{h^2}. \tag{3.11}$$

Then, we find a condition of spatial stability as

$$\Delta t \geq \frac{1}{8}\frac{h^2}{c_v}, \tag{3.12}$$

from which we identify that the mixed interpolations still have a lower bound of time step size.

3.2.2 Inf-sup condition

The consolidation problems with incompressible fluid result in $\boldsymbol{Q} = \mathbf{0}$ in Equation 2.31 and 2.34 in the previous chapter. Then, as Δt approaches zero, $\boldsymbol{F}$ in Equation 2.31 becomes $\mathbf{0}$. Then, the problem has the same form of the Stoke's problem, expressed as

$$\underbrace{\begin{bmatrix} \boldsymbol{K} & \boldsymbol{B}^T \\ \boldsymbol{B} & \mathbf{0} \end{bmatrix}}_{\boldsymbol{G}_m} \begin{bmatrix} \delta\boldsymbol{u} \\ \delta\boldsymbol{p} \end{bmatrix}^n = - \begin{bmatrix} \boldsymbol{R}^u \\ -\boldsymbol{R}^p \end{bmatrix}. \tag{3.13}$$

where $\boldsymbol{B} = -\boldsymbol{L}$. When $\mathrm{Ker}\boldsymbol{B}^T \neq \{\mathbf{0}\}$, the column vectors of the linear system are not independent, which leads to singularity.

From [32], we have

$$\sup_{\boldsymbol{v}_h \in \mathcal{U}_h} \frac{\int_\Omega q_h Div \boldsymbol{v}_h \, d\Omega}{\|\boldsymbol{v}_h\|_{\mathcal{U}_h}} \geq \tilde{C} \|q_h\|_{\mathcal{Q}_h / \mathrm{Ker} \boldsymbol{B}_h^T}, \ \ \forall q_h \in \mathcal{Q}_h, \tag{3.14}$$

where $||\cdot||_V$ is a defined norm for space V and $\tilde{C} > 0$, a constant independent of the mesh size. The right side of Equation 3.14 becomes zero when q_h is chosen from the space of $\mathrm{Ker}\boldsymbol{B}_h^T$. This implies that multiple solutions can exist if $\mathrm{Ker}\boldsymbol{B}_h^T \neq \{\boldsymbol{0}\}$, just as explained in Equation 3.13. Thus, the condition $\mathrm{Ker}\boldsymbol{B}_h^T = \{\boldsymbol{0}\}$ (or $\mathrm{Ker}\boldsymbol{B}^T = \{\boldsymbol{0}\}$ in a matrix form of Equation 3.13) is required for uniqueness of solution, which is the inf-sup condition[3].

According to [57] and [58], one order lower approximation of pressure, such as Taylor-Hood elements, can satisfy the inf-sup condition, deriving the following error estimates [58],

$$\|\boldsymbol{\varepsilon}(\boldsymbol{u}(t_m)) - \boldsymbol{\varepsilon}(\boldsymbol{u}_h^m)\|_{L^2} \leq C(h^n + \Delta t) \sup_{\tau \in (0,\infty)} \phi(\tau), \tag{3.15}$$

$$\|\mathbf{Grad} p(t_m) - \mathbf{Grad} p_h^m\|_{L^2} \leq C(h^l + \Delta t) \sup_{\tau \in (0,\infty)} \phi(\tau), \tag{3.16}$$

$$\phi(\tau) = |\boldsymbol{u}(\tau)|_{n+1} + |p(\tau)|_n + |\partial_t \boldsymbol{u}(\tau)|_{n+1} + |\partial_t p(\tau)|_n + \|\mathrm{Div} \partial_{tt} \boldsymbol{u}(\tau)\|_{L^2}, \tag{3.17}$$

where $n = l + 1$, t_m is time at the m^{th} time step, and $(\cdot)^m$ is a physical quantity at the m^{th} time step. In the error estimate, $\|\mathbf{Grad} p\|_{L^2}$ is assumed to be bounded. However, as aformentioned in the previous section, $\|\mathbf{Grad} p\|_{L^2}$ cannot properly be bounded at the drainage boundary at early times for the consolidation problems, and small oscillations are still observed, even though the elements satisfy the inf-sup condition (i.e., Q2Q1)[4].

[3]The original form for Stokes equation is addressed in Appendix E.

[4]Meanwhile, the piecewise linear FVM for both geomechanics and flow might circumvent violation of the inf-sup condition [60]. However, this choice of space discretization still has restriction of time step size from the discontinuity of pressure for the consolidation problems, as Equation 3.12.

$$\Delta t \geq \frac{1}{8} \frac{h^2}{c_v},$$

Both Q1Q1 and Q1P0 element pairs do not satisfy the inf-sup condition, while the Q2Q1 element does [31]. The Q1Q1 pair constrains the system too much, and the Q1P0 pair has been criticized by the checker-board pressure oscillation. Then, stabilization techniques have been used to reduce the instability, by introducing to the submatrix $\mathbf{0}$ of Equation 3.13 an error term that can preserve consistency in space and time [27, 28].

On the other hand, when the fixed-stress sequential method is used (Equation 2.37), Equation 3.13 is changed to

$$\underbrace{\begin{bmatrix} \boldsymbol{K} & \boldsymbol{B}^T \\ \mathbf{0} & \boldsymbol{S} \end{bmatrix}}_{\boldsymbol{G}_s} \begin{bmatrix} \delta \boldsymbol{u} \\ \delta \boldsymbol{p} \end{bmatrix}^n = \begin{bmatrix} \mathbf{0} & \mathbf{0} \\ -\boldsymbol{B} & \boldsymbol{S} \end{bmatrix} \begin{bmatrix} \delta \boldsymbol{u} \\ \delta \boldsymbol{p} \end{bmatrix}^{n-1} - \begin{bmatrix} \boldsymbol{R}^u \\ -\boldsymbol{R}^p \end{bmatrix}, \tag{3.18}$$

where all the column vectors of $\boldsymbol{G}_s$ are independent, because $\boldsymbol{K}$ and $\boldsymbol{S}$ are positive-definite. As a result, $\boldsymbol{G}_s$ is invertible, unlike $\boldsymbol{G}_m$ in Equation 3.13. Therefore, all the element choices (i.e., Q1Q1, Q2Q1, Q1P0) can provide uniqueness of solution, which do no require any other stabilization techniques.

For example, the Q1P0 element comes from the mixed formulation of the piecewise linear finite element method for geomechanics and the piecewise constant finite volume method for flow, being a natural choice of a sequential scheme in reservoir engineering. The Q1P0 pair with the fixed stress method can yield spatial stability in space without exhibiting the checker-board pressure oscillation due to contribution from $\boldsymbol{S}$ of Equation 3.18, while the monolithic method requires a stabilizer to remove the pressure oscillation. Furthermore, its piecewise constant interpolation of pressure can yield stability even if a consolidation problem generates self-discontinuity at the drainage boundary at the initial time. Thus, the mixed FEM/FVM with the fixed-stress sequential method becomes one

which implies that time step size cannot be refined for accuracy. Thus, the piecewise linear FVM does not yield convergence in time.

of the stable spatial and temporal discretization schemes in poromechanics simulation.

We can compare the fixed-stress split scheme with Uzawa's algorithm. Uzawa's algorithms are frequently used to solve the saddle point problems [62, 63], writtens as

$$
\begin{aligned}
&\text{for } \; k = 1 \; \text{ until convergence, do} \\
&\quad \text{Solve } \; \boldsymbol{K}\delta\boldsymbol{u}^k = -\boldsymbol{R}^u - \boldsymbol{B}^T\delta\boldsymbol{p}^{k-1} && (3.19)\\
&\quad \text{Compute } \; \delta\boldsymbol{p}^k = \delta\boldsymbol{p}^{k-1} + \gamma_{\text{uz}}\left(\boldsymbol{B}\delta\boldsymbol{u}^k - \boldsymbol{R}^p\right) && (3.20)\\
&\text{end do,}
\end{aligned}
$$

where k indicates the iteration level and γ_{uz} is a suitably chosen parameter. Then, the Uzawa algorithm leads to modification of Equation 3.13 as an iterative solver, as follows:

$$
\begin{bmatrix} \boldsymbol{K} & \boldsymbol{B}^T \\ \boldsymbol{B} & \boldsymbol{0} \end{bmatrix} \begin{bmatrix} \delta\boldsymbol{u} \\ \delta\boldsymbol{p} \end{bmatrix}^{n,(k)} \rightarrow \underbrace{\begin{bmatrix} \boldsymbol{K} & \boldsymbol{0} \\ \boldsymbol{B} & \frac{1}{\gamma_{\text{uz}}}\boldsymbol{I} \end{bmatrix}}_{\boldsymbol{G}_{\text{uz}}} \begin{bmatrix} \delta\boldsymbol{u} \\ \delta\boldsymbol{p} \end{bmatrix}^{n,(k)} - \underbrace{\begin{bmatrix} \boldsymbol{0} & -\boldsymbol{B}^T \\ \boldsymbol{0} & \frac{1}{\gamma_{\text{uz}}}\boldsymbol{I} \end{bmatrix}}_{\boldsymbol{N}_{\text{uz}}} \begin{bmatrix} \delta\boldsymbol{u} \\ \delta\boldsymbol{p} \end{bmatrix}^{n,(k-1)}, \quad (3.21)
$$

where Gauss-Seidel type iteration is applied. $\boldsymbol{I}$ is the identity matrix. Solvability of $\boldsymbol{G}_{\text{uz}}$ heavily relies on γ_{uz}, although $\boldsymbol{G}_{\text{uz}}$ theoretically has the full rank. Specifically, when γ_{uz} is too large, $\boldsymbol{G}_{\text{uz}}$ become singular, causing an ill-conditioned matrix followed by difficulty in convergence. Also, for the case not to satisfy the inf-sup condition, Algorithm 3.20 can possibly be modified to improve convergence, introducing a stabilization matrix $\boldsymbol{S}_{\text{uz}}$, as

$$
\text{Compute } \; \delta\boldsymbol{p}^k = \delta\boldsymbol{p}^{k-1} + \gamma_{\text{uz}}\left(\boldsymbol{B}\delta\boldsymbol{u}^k - \boldsymbol{S}_{\text{uz}}\delta\boldsymbol{p}^{k-1} - \boldsymbol{R}^p\right), \quad (3.22)
$$

where Elman and Golub [63] takes $S_{\text{uz}} = \beta_{\text{uz}} h_m^2 \boldsymbol{A}_n$, where β_{uz} is an arbitrary numerical parameter, h_m is the mesh size parameter, and $\boldsymbol{A}_n$ is a discrete Laplace operator defined on the pressure space, subject to Neumann boundary condition [64]. Along with solvability,

convergence of Algorithm 3.22 requires $\left\|\boldsymbol{G}_{\text{uz}}^{-1}\boldsymbol{N}_{\text{uz}}\right\| < 1.0$ [65]. For both Uzawa's algorithms, appropriate determination of γ_{uz} and β_{uz} are critical for convergence and accuracy.

On the other hand, the fixed-stress method can be modified for solution of Equation 3.13 as an iterative solver, as shown in Equation 3.18, when $\boldsymbol{F} = \boldsymbol{0}$. Compared to the Uzawa's algorithms, $\boldsymbol{S}$ only depends on b^2/K_{dr}, not containing a numerical parameter. It is worth noting that the fixed-stress method does not require calculating $\boldsymbol{K}^{-1}$, while $\boldsymbol{S}$ is very close to $\boldsymbol{L}\boldsymbol{K}^{-1}\boldsymbol{L}^T$. Kim et al. [38] shows that the spectral radius of the fixed-stress method does not exceed 2/3, which guarantees convergence in solving Equation 3.13.

Now as a simple system, let us introduce a two-gridblock 1D problem, shown in Figure 3.1. For the FEM/FVM discretization (left of Figure 3.1), pressure is located at a grid center whereas displacement is at a node. On the other hand, for the FEM/FEM discretization (right of Figure 3.1), both pressure and displacement are located at a node. When we use the mixed FEM/FVM and the FEM/FEM methods with the monolithic approach, the corresponding Jacobian matrices for $\boldsymbol{Q} = \boldsymbol{0}$ ($\boldsymbol{G}_m^V$ and $\boldsymbol{G}_m^E$, respectively) are

$$\boldsymbol{G}_m^V = \begin{bmatrix} \frac{2K_c}{\Delta x} & -b & b \\ b & \alpha_p & -\alpha_p \\ -b & -\alpha_p & \alpha_p \end{bmatrix}, \quad \boldsymbol{G}_m^E = \begin{bmatrix} \frac{2K_c}{\Delta x} & -\frac{b}{2} & 0 & \frac{b}{2} \\ \frac{b}{2} & \alpha_p & -\alpha_p & 0 \\ 0 & -\alpha_p & 2\alpha_p & -\alpha_p \\ -\frac{b}{2} & 0 & -\alpha_p & \alpha_p \end{bmatrix}, \quad \alpha_p = \frac{k_p \Delta t}{\mu \Delta x}, \tag{3.23}$$

where Δx is the grid spacing. When Δt approaches zero, α_p becomes zero, and thus both $\boldsymbol{G}_m^V$ and $\boldsymbol{G}_m^E$ become singular. As a result, a unique solution cannot be obtained. A very small time step size is typically taken at early times, considering initialization of flow and/or geomechanics. Thus, if the monolithic approach with a direct matrix solver is used, the uniqueness of solution might not be guaranteed.

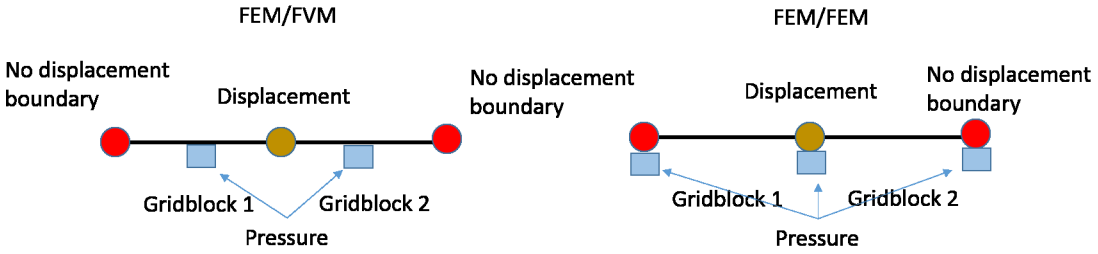

Figure 3.1: Different space discretizations for flow and geomechanics: FEM/FVM vs. FEM/FEM.

On the other hand, the fixed-stress sequential method yields

$$\boldsymbol{G}_s^V = \begin{bmatrix} \frac{2K_c}{\Delta x} & -b & b \\ 0 & \alpha_p + b^2/K_c & -\alpha_p \\ 0 & -\alpha_p & \alpha_p + b^2/K_c \end{bmatrix},$$
$$\boldsymbol{G}_s^E = \begin{bmatrix} \frac{2K_c}{\Delta x} & -\frac{b}{2} & 0 & \frac{b}{2} \\ 0 & \alpha_p + b^2/K_c & -\alpha_p & 0 \\ 0 & -\alpha_p & 2\alpha_p + b^2/K_c & -\alpha_p \\ 0 & 0 & -\alpha_p & \alpha_p + b^2/K_c \end{bmatrix}, \tag{3.24}$$

where $\boldsymbol{G}_s^V$ and $\boldsymbol{G}_s^E$ are the Jacobian matrices from the mixed FEM/FVM and the FEM/FEM methods, respectively. Even though Δt becomes very small, which makes α_p zero, both $\boldsymbol{G}_s^V$ and $\boldsymbol{G}_s^E$ still have the full rank, yielding a unique solution.

3.2.3 Double/multiple porosity system

When a set of fractures exists, we have local heterogeneity because the fracture and rock matrix coexist, viewed as dual continua. To consider the local heterogeneity, it is desirable to use double or multiple porosity models [66], particularly for low permeable rock matrix, as shown in Figure 3.2.

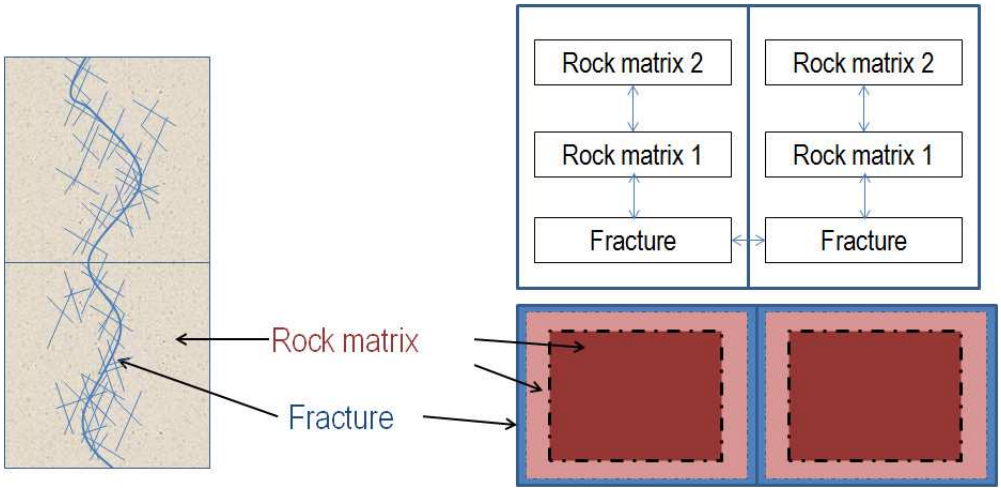

Figure 3.2: Left: a schematic diagram of a fracture-matrix system. Right: a conceptual model of the multiple interacting continuum (MINC) model. In the MINC model, fluid flows through the fracture medium over the domain. On the other hand, the rock matrix medium stores fluid and conveys it to the fracture medium. We can have several rock matrix media in order to model fluid-heat flow accurately.

For flow-only simulation with the double/multiple porosity models, the FVM has been used in reservoir engineering [66]. Berryman [67] proposed the constitutive relations for double porosity model of isothermal poroelasticity, and Kim et al. [68] generalized the model to the multiple porosity thermoporoelastoplasticity with multiphase flow. For the case of the multiple porosity poroelasticity with single phase flow in isothermal condition, we have

$$\delta\boldsymbol{\sigma} = \overbrace{\mathbf{C}_{up} : \delta\boldsymbol{\varepsilon}}^{\delta\boldsymbol{\sigma}'} - b_l^* \delta p_l \mathbf{1}, \quad b_l^* = K_{dr} \left(\frac{\alpha\eta}{K}\right)_l, \quad \frac{1}{K_{dr}} = \frac{\eta_k}{K_k}, \quad \mathbf{C}_{up} = K_{dr} \sum_{k=1}^{n_m} \frac{\eta_k}{K_k} \mathbf{C}_k, \tag{3.25}$$

$$\delta\zeta_l = b_l^* \delta\varepsilon_v, \tag{3.26}$$

where double indices indicate summation. Subscript k or l indicates one of the subelements within a gridblock. $\boldsymbol{\sigma}$, $\boldsymbol{\sigma}'$, and $\boldsymbol{\varepsilon}$ are total stress, effective stress, and total strain at the level of a gridblock. K_{dr} and $\mathbf{C}_{up}$ are the upscaled elastoplastic drained bulk and tangent

moduli at the gridblock. α_l is the Biot coefficient of the subelement l, (i.e., $\alpha_l = 1 - K_l/K_s$, where K_s is the intrinsic solid grain bulk modulus.). η_l is the volume fraction of the subelement l, and K_l is the drained bulk modulus of the subelement l. ζ_l is the fluid content for the material l. $\delta\zeta_l = (\delta m/\rho)_l$, where m_l is the fluid mass of the subelement l.

From Equations 3.25 and 3.26, the multiple porosity model yields

$$\underbrace{\begin{bmatrix} \boldsymbol{K} & \boldsymbol{B}_f^T & \boldsymbol{B}_m^T \\ \boldsymbol{B}_f & -\Delta t \boldsymbol{T}_{ff} & -\Delta t \boldsymbol{T}_{fm} \\ \boldsymbol{B}_m & -\Delta t \boldsymbol{T}_{fm} & -\Delta t \boldsymbol{T}_{mm} \end{bmatrix}}_{\boldsymbol{G}_m^{mp}} \begin{bmatrix} \delta \boldsymbol{u} \\ \delta \boldsymbol{p}_f \\ \delta \boldsymbol{p}_m \end{bmatrix}^n = - \begin{bmatrix} \boldsymbol{R}^u \\ -\boldsymbol{R}_f^p \\ -\boldsymbol{R}_m^p \end{bmatrix}, \tag{3.27}$$

where p_f and p_m are the pressures at the fracture and rock-matrix, respectively. The subscripts f and m indicate fracture and rock-matrix, respectively. T_{ff}, T_{fm}, and T_{mm} are also the matrices from transmissibilities of fracture-fracture, fracture-rock matrix, rock matrix-rock matrix, respectively. Because the rock-matrix permeabillity is much lower than the fracture permeability, the transmissibility of the rock-matrix is much smaller than that of the fracture. Thus, although time step size is not sufficient to make $\Delta t \boldsymbol{T}_{ff}$ null, it can make $\Delta t \boldsymbol{T}_{fm}$ and $\Delta t \boldsymbol{T}_{mm}$ become almost zero matrices due to the extremely low transmissibility [59]. Thus, $\boldsymbol{G}_m^{mp}$ can be singular, not providing a unique solution. When we consider the previous 1D example, as shown in Figure 3.1, it is obvious that the monolithic scheme with the mixed FEM/FVM does not yield a unique solution.

On the other hand, when the fixed-stress method is used, Equation 3.27 is changed to

$$\underbrace{\begin{bmatrix} \boldsymbol{K} & \boldsymbol{B}_f^T & \boldsymbol{B}_m^T \\ \boldsymbol{0} & -\Delta t \boldsymbol{T}_{ff} - \boldsymbol{S}_f & -\Delta t \boldsymbol{T}_{fm} \\ \boldsymbol{0} & -\Delta t \boldsymbol{T}_{fm} & -\Delta t \boldsymbol{T}_{mm} - \boldsymbol{S}_m \end{bmatrix}}_{=\boldsymbol{G}_s^{mp}} \begin{bmatrix} \delta \boldsymbol{u} \\ \delta \boldsymbol{p}_f \\ \delta \boldsymbol{p}_m \end{bmatrix}^n = \begin{bmatrix} \boldsymbol{0} & \boldsymbol{0} & \boldsymbol{0} \\ -\boldsymbol{B}_f & -\boldsymbol{S}_f & \boldsymbol{0} \\ -\boldsymbol{B}_m & \boldsymbol{0} & -\boldsymbol{S}_m \end{bmatrix} \begin{bmatrix} \delta \boldsymbol{u} \\ \delta \boldsymbol{p}_f \\ \delta \boldsymbol{p}_m \end{bmatrix}^{n-1} - \begin{bmatrix} \boldsymbol{R}^u \\ -\boldsymbol{R}_f^p \\ -\boldsymbol{R}_m^p \end{bmatrix}, \tag{3.28}$$

where $\boldsymbol{S}_l$ is symmetric and positive-definite, calculated from b_l^2/K_l locally at a subelement l. Unlike $\boldsymbol{G}_m^{mp}$ from the monolithic method, $\boldsymbol{G}_s^{mp}$ has full rank due to $\boldsymbol{S}_l$. Thus, the fixed-stress method provides a unique solution.

3.2.4 Comparison with the stabilized monolithic FEM method

Stabilized FEM methods for the same low-order approximation (e.g., Q1Q1) have been introduced in order to avoid spatial instability of the monolithic method [28, 59, 69]. Specifically, a stabilization matrix [28] is introduced to the null matrix part of $\boldsymbol{G}_m$ in Equation 3.13, which yields

$$\underbrace{\begin{bmatrix} \boldsymbol{K} & \boldsymbol{B}^T \\ \boldsymbol{B} & -\tilde{\boldsymbol{S}} \end{bmatrix}}_{\boldsymbol{G}_m^{stab}} \begin{bmatrix} \delta\boldsymbol{u} \\ \delta\boldsymbol{p} \end{bmatrix}^{n,(k+1)} = \begin{bmatrix} -\boldsymbol{R}^u \\ \boldsymbol{R}^p \end{bmatrix}^{(k)} + \begin{bmatrix} \boldsymbol{0} \\ \boldsymbol{H}^{stab} \end{bmatrix}^{(k)}, \tag{3.29}$$

$$\boldsymbol{H}^{stab} = \int_\Omega \frac{\tau}{2G}[\varphi_h - \Pi(\varphi_h)][p_h^{n+1,k} - \Pi(p_h^{n+1,k}) - p_h^n + \Pi(p_h^n)]\, d\Omega, \tag{3.30}$$

$$\Pi(\cdot)|_\Omega^e = \frac{1}{\Omega^e}\int_\Omega (\cdot) d\Omega, \tag{3.31}$$

$$\tilde{\boldsymbol{S}} = \int_\Omega \frac{\tau}{2G}[\varphi_h - \Pi(\varphi_h)][\varphi_h - \Pi(\varphi_h)]\, d\Omega, \tag{3.32}$$

where Ω^e is the volume of the element. $\Pi(\cdot)$ is an operator that takes the element average at each element. $\tau(>0)$ is a parameter tha can adjust the level of stabilization. From Equation 3.32, $\tilde{\boldsymbol{S}}$ is symmetric and positive-definite. Thus, $\boldsymbol{G}_m^{stab}$ becomes invertible, which can provide a unique solution.

Similar to the fixed-stress method, the stabilized monolithic FEM method also introduces $-\tilde{\boldsymbol{S}}$ into the null sub-matrix. However, in contrast with the fixed-stress method, the stabilized monolithic FEM method causes high computational cost because of the monolithic scheme. In addition, $\boldsymbol{G}_m^{stab}$ might not be well-conditioned due to high contrast of eigenvalues between $\boldsymbol{K}$ and $\tilde{\boldsymbol{S}}$, which requires strong linear solvers. Its accuracy also highly depends on τ, a user-determined parameter.

In this study, we take a stabilized monolithic FEM for numerical study, specifically written as

$$\underbrace{\begin{bmatrix} \boldsymbol{K} & \boldsymbol{B}^T \\ \boldsymbol{B} & -\tilde{\boldsymbol{S}} \end{bmatrix}}_{\boldsymbol{G}_m^{stab}} \begin{bmatrix} \delta \boldsymbol{u} \\ \delta \boldsymbol{p} \end{bmatrix}^n = \begin{bmatrix} -\boldsymbol{R}^u \\ \boldsymbol{R}^p \end{bmatrix}^n + \begin{bmatrix} \boldsymbol{0} \\ \boldsymbol{H}_n^{stab} \end{bmatrix}, \tag{3.33}$$

$$\boldsymbol{H}_n^{stab} = \int_\Omega \frac{\tau}{2G} [\varphi_h - \Pi(\varphi_h)][p_h^n - \Pi(p_h^n) - p_h^{n-1} + \Pi(p_h^{n-1})] \, d\Omega, \tag{3.34}$$

where $\boldsymbol{G}_m^{stab}$ is solved by a direct method. $\boldsymbol{H}_n^{stab}$ of the stabilized monolithic FEM is calculated from the previous time steps, taking no iterations, in order to have the same computational cost as the monolithic method of Equation 3.13, while Equation 3.29 requires full iteration, causing significant higher computational cost.

3.3 Numerical Examples

We perform numerical simulation in order to examine mathematical analysis shown in the previous sections. Specifically, we take four different spatial discretizations for displacement and pressure: Q1-Q1, and three other mixed formulation of Q2-Q1, Q1-P0, and Q2-P0 (Figure 3.3). For each discretization, We take two different solution strategies for both compressible and incompressible fluids: the monolithic and the fixed-stress sequential methods. Then, total 16 combinations are investigated at each numerical scenario. There are three different test scenarios: Terzaghi's consolidation problem, a production problem, a strip-footing plane strain problem (i.e., McNamee-Gibson problem [70, 71]). In addition, we also test a stabilized finite element method for the Q1Q1 pair with a direct solver for G_m^{stab} (Equation 3.33 - Equation 3.34). For the time discretization, we employ the backward-Euler method for all the examples.

We consider isothermal single-phase flow with isotropic and homogeneous geomaterial. We assume no gravitational effects and no stress dependence of flow properties. The common properties for all three examples are shown in the Table 3.1. Two compressibili-

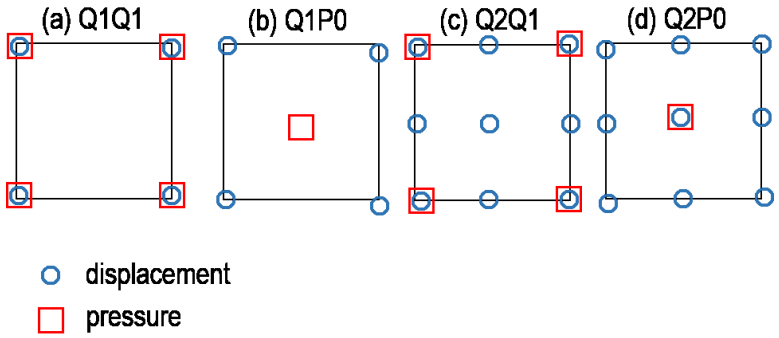

Figure 3.3: Four space discretization methods of flow and geomechanics.Q1Q1: bilinear interpolation of both displacement and pressure within an element. Q1P0: bilinear interpolation of displacement and constant interpolation of pressure. Q2Q1: biquadratic interpolation of displacement and bilinear interpolation of pressure. Q2P0: biquadratic interpolation of displacement and constant interpolation of pressure.

ties, 4.0×10^{-9} [Pa^{-1}] and 0 [Pa^{-1}], are used for compressible and incompressible fluids, respectively. We then investigate the numerical instabilities in pressure field at early time, taking a very small timestep size, which can be caused by incompatibility at the drainage boundary and/or the violation of the inf-sup condition.

Table 3.1: Common input data for three test scenarios

Property	Value	
Young's modulus	100	MPa
Poisson ratio	0	-
Biot's coefficient	1.0	-
porosity	0.3	-
permeability	50	mD
fluid density	1000	kg m^{-3}
fluid viscosity	1	cp
fluid compressibility	4.0×10^{-9} or 0	Pa^{-1}

3.3.1 Case 1: Terzaghi's consolidation problem

The domain is discretized with 20 grids, where each grid has a size ($\Delta x \times \Delta z$) of 1 m $\times$ 0.25 m, being 5 [m] in depth and 1 [m] in width (Figure 3.4). For geomechanics, 2.125 [MPa] of traction is applied to the top, while a no-vertical displacement boundary is placed at the bottom, and a no-horizontal displacement boundary is applied to both sides. Flow has drainage boundary at the top, where pressure is zero, and a no-flow boundary at the bottom. The initial pressure and total stress are also both zero (i.e., zero excessive pore-pressure). Then, before the traction is applied, the system is mechanically in equilibrium.

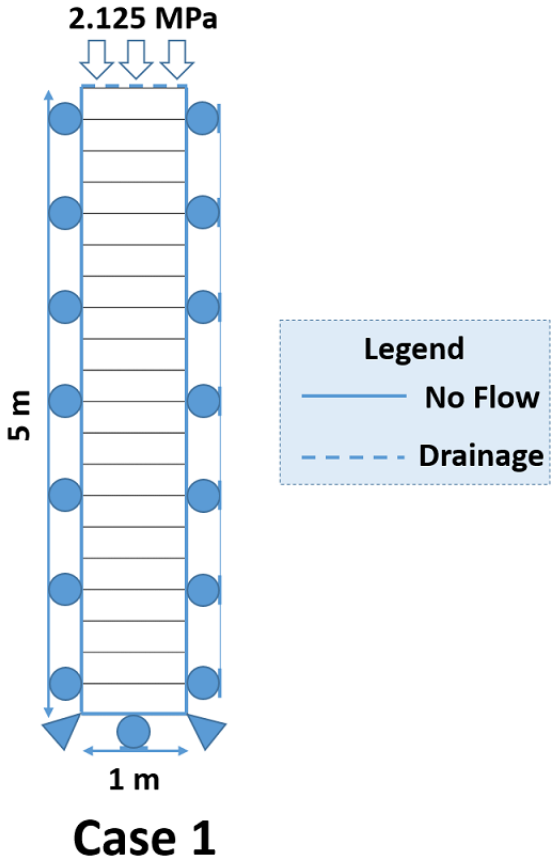

Figure 3.4: Schematics of Case 1: a consolidation problem (i.e., Terzaghi's problem).

Again for the stabilized monolithic FEM, we take $\tau = 1.0$ for the stabilization method, as suggested by [28] for all the Q1Q1 pair, hereafter. The simulation result is after 1 timestep with $\Delta t = 0.01\ [s]$. Thus the normalized or dimensionless time for the result is then, $T = c_v t/h^2 = 1.9378 \times 10^{-6}$.

Q1Q1: The top of Figure 3.5 shows the pressure distributions of the Q1Q1 pair where MONO and FSS indicate the solutions of the monolithic and the fixed-stress sequential methods, respectively while MonoSTAB is White's stabilized method. For Q1Q1, we find considerable oscillation near the drainage boundary due to discontinuity of pressure for compressible fluid, when using the monolithic method, although the inf-sup condition is not violated. When fluid is incompressible, the oscillation becomes severer because of violation of the inf-sup condition. However, for both compressible and incompressible fluids, the fixed-stress sequential method yields much more stable and accurate results than the monolithic method. The MonoSTAB, the stabilized monolithic method, has the same stability state for both compressible and incompressible cases with the fixed-stress method showing very tiny oscillation at the drainage boundary due to the pressure discontinuity at it. Through the artificial diffusion within the null matrix part of $\boldsymbol{G}_m$ in Equation 3.13, it removes the oscillation referring to the inf-sup condition as found in the result plots in Figure 3.5. However, without any artificial factor implementation, these results support the argument that the fixed-stress method itself can naturally stabilize the oscillation caused by discontinuity of pressure at the drainage boundary and/or violation of the inf-sup condition.

Q1P0: We find different results from the Q1P0 pair (the bottom of Figure 3.5), as contrasted with Q1Q1. We do not observe instability at the drainage boundary at the top, because the pressure field is interpolated as piecewise constant, facilitating discontinuous

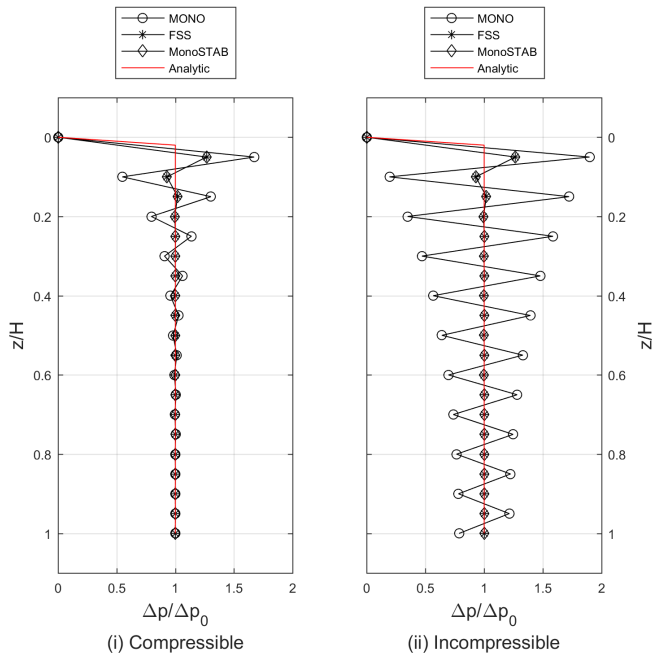

(a) Q1Q1: compressible (left) and incompressible (right)

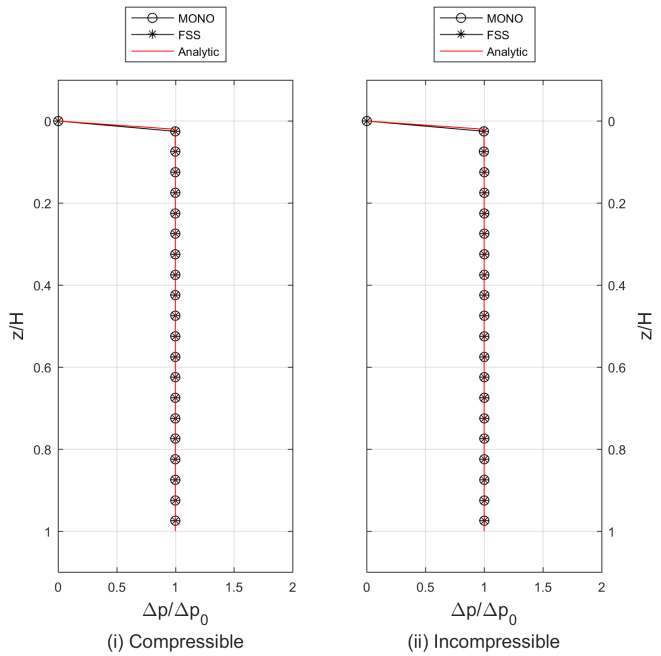

(b) Q1P0: compressible (left) and incompressible (right)

Figure 3.5: Pressure distributions for Case 1 with Q1Q1 (top) and Q1P0 (bottom) for both compressible and incompressible fluids.

pressure distribution. For incompressibility, Q1P0 is known to be more stable than Q1Q1, although it does not satisfy the inf-sup condition in general. From the bottom of Figure 3.5, both the monolithic and the fixed-stress methods do not cause oscillation in pressure, being accurate and not violating the inf-sup condition.

Q2Q1 & Q2P0: The Q2Q1 pair, one of the Tayler-Hood elements, is known as an LBB-stable element. For Q2Q1 and Q2P0, both the monolithic and the fixed-stress methods yield identical results, shown in Figure 3.6. We find that Q2Q1 shows oscillation near the drainage boundary, although it does not violate the inf-sup condition. In addition, the Q2Q1 pair shows more stable results than Q1Q1, even for the same compressible fluid. The quadratic interpolation of displacement causes much less oscillation than the linear interpolation, yielding less strict stability condition (see Equation 3.12). We also find that Q2P0 is as stable as Q1P0, having no oscillation for both compressible and incompressible fluids.

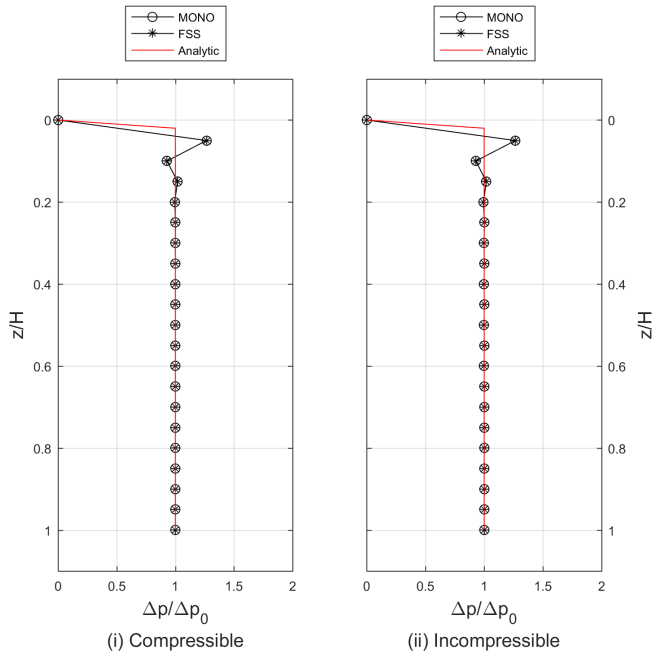

(a) Q2Q1: compressible (left) and incompressible (right)

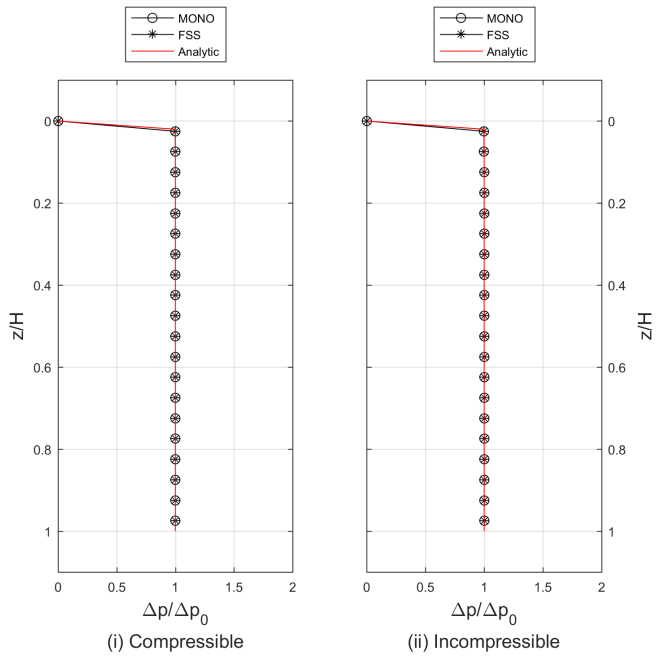

(b) Q2P0: compressible (left) and incompressible (right)

Figure 3.6: Pressure distributions for Case 1 with Q2Q1 (top) and Q2P0 (bottom) for both compressible and incompressible fluids.

3.3.2 Case 2: production problem

For the Case 2 scenario, we take a simple production problem. For the simulation domain, we have two different boundary conditions especially with geomechanics as shown in Figure 3.7. For Case 2-1, (a) in Figure 3.7, we have no displacement normal to all the boundaries. Reversely for Case 2-2, (b) in Figure 3.7, all displacement boundary conditions are exactly perpendicular to the corresponding boundaries of Case 2-1.

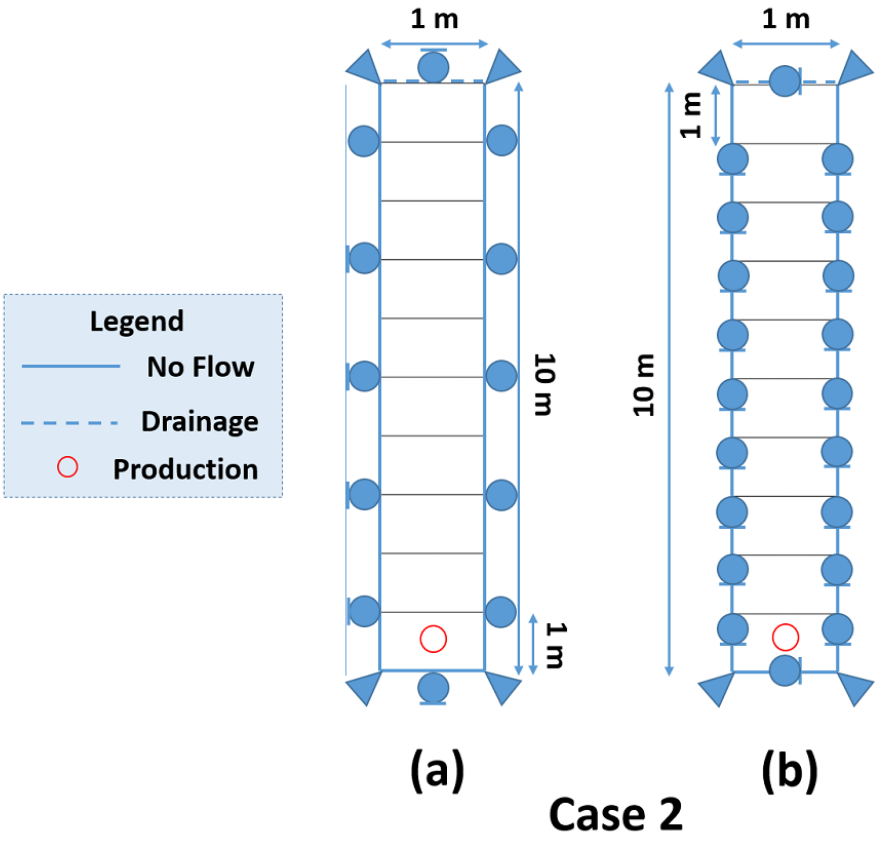

Figure 3.7: Schematics of Case 2: two production problems. Two different boundary conditions are applied as (a) Case 2-1 and (b) Case 2-2.

There is no overburden stress at the top. For flow, we have no-flow boundary condition

for all boundaries except for the top drainage boundary. The production well is located at the bottom block with the rate of $Q_{prod} = 10^6$ [kg/m^3/day]. Initial pressure and total stress are 2.125 [MPa], and thus the excessive pore-pressure is zero. The time step size Δt is 1 second and we use numerical results at 100 seconds. For Case 2-1, we can obtain the accurate numerical solution by taking the finite-element or finite-volume based flow-only simulation with the exact rock-compressibility, just like the procedure of the analytical solution for Case 1, because the directions of stress and flow are one-dimensional. Then, we use this solution as a reference solution for both cases (Case 2-1 & Case 2-2). The simulation result is after 1 timestep with $\Delta t = 0.01$ $[s]$, exactly the same condition as Case 1.

Q1Q1: From the top of Figure 3.8, for Case 2-1, we have all stable results for compressible fluid when we use the monolithic, the stabilized monolithic, and the fixed-stress methods, because they do not have severe discontinuity effect at the boundary (i.e., no instantaneous pressure jump at the drainage boundary). For incompressible fluid, the monolithic method causes severe oscillation, because it violates the inf-sup condition. Note that the reference solution is indicated as FLOW ONLY.

Note that $\boldsymbol{G}_m$ of Equation 3.13 is not invertible. On the other hand, both stabilized monolithic methods and the fixed-stress methods yield stability in space, because $\boldsymbol{G}_m^{stab}$ of Equation 3.29 and $\boldsymbol{G}_s$ of Equation 3.18 are invertible, respectively. Both the stabilized monolithic method and the fixed-stress method yield accurate solutions, matching the reference solution.

From the top of Figure 3.9, for Case 2-2, we have different type of oscillation for Q1Q1 in both compressible and incompressible conditions. The monolithic method has a tiny oscillation near the production well even for compressible fluid and this oscillation becomes severer for incompressible fluid violating the inf-sup condition. These results

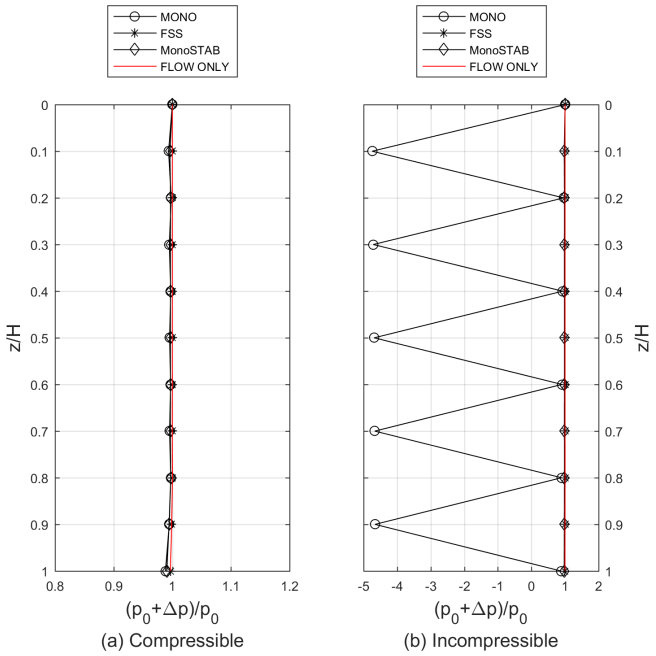

(a) Q1Q1: compressible (left) and incompressible (right)

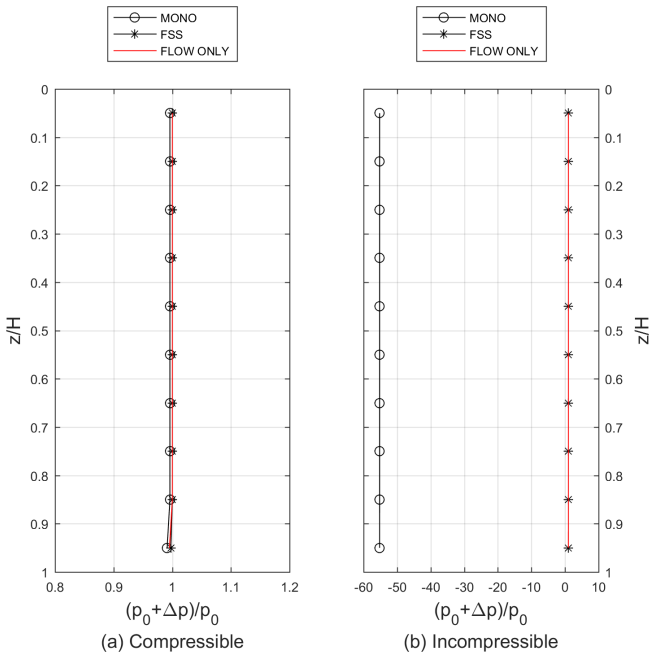

(b) Q1P0: compressible (left) and incompressible (right)

Figure 3.8: Pressure distributions for Case 2-1 with Q1Q1 (top) and Q1P0 (bottom) for both compressible and incompressible fluids.

are probably due to the different displacement conditions, no vertical displacement but horizontal displacement and vice versa for the top and bottom boundary conditions. All other methods, the fixed-stress and the stabilized method show no oscillation, stabilizing the effects in both fluid compressibility cases.

Q1P0: Both the bottom of Figure 3.8 (for Case 2-1) and the bottom one of Figure 3.9 (for Case 2-2) show stable results for both monolithic and fixed-stress methods for compressible fluid, just like the Q1Q1 pair. However, for incompressible fluid, the monolithic method causes instability unlike Case 1. Aforementioned in [31], we categorize this as the 'spurious mode', which can be found the Q1P0 pair, violating the inf-sup condition. On the other hand, the fixed stress method is stable and accurate, matching the reference solution and circumventing violation of the inf-sup condition. As for Case 2-2, the notorious 'checkerboard' oscillation of Q1P0 for the incompressible case can be found distinctly for incompressible fluid especially as shown in the bottom of Figure 3.9.

Q2Q1 & Q2P0: For the Q2Q1 and Q2P0 pairs, two different results can be found depending on the boundary conditions, Case 2-1 and Case 2-2.

Figure 3.10 shows that the monolithic and the fixed-stress methods are stable and accurate, regardless of fluid compressibility, when Q2Q1 is used, albeit a slight tendency of locking for incompressible fluid near the drainage boundary. As for Q2P0 result, the biquadratic interpolation of displacement yields much more stable and accurate solution than the bilinear interpolation of displacement. However, the spurious mode of pressure as Q1P0 due to the inf-sup condition stays the same for Case 2-1 boundary condition, implying that Q2P0 is not satisfying the inf-sup condition in general. For Case 2-2 unlike Case 2-1 results, Figure 3.11 clearly shows that the monolithic and the fixed-stress methods are stable and accurate, regardless of fluid compressibility using Q2Q1 and Q2P0.

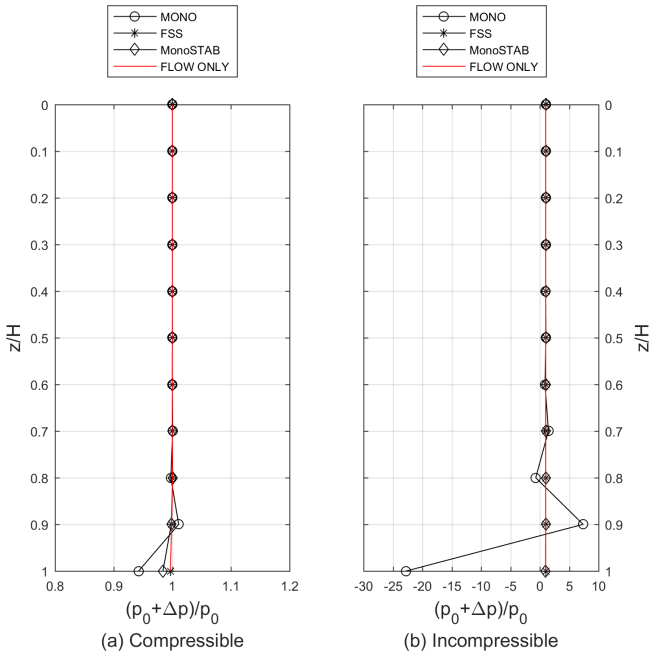

(a) Q1Q1: compressible (left) and incompressible (right)

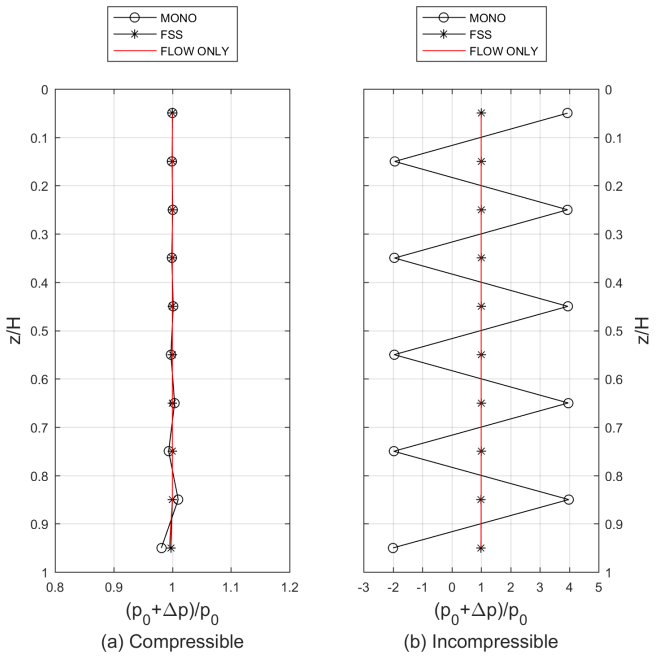

(b) Q1P0: compressible (left) and incompressible (right)

Figure 3.9: Pressure distributions for Case 2-2 with Q1Q1 (top) and Q1P0 (bottom) for both compressible and incompressible fluids.

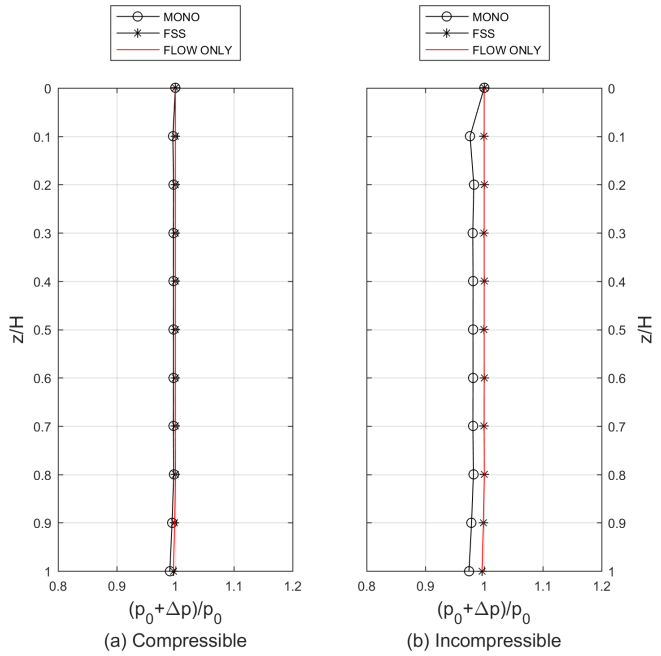

(a) Q2Q1: compressible (left) and incompressible (right)

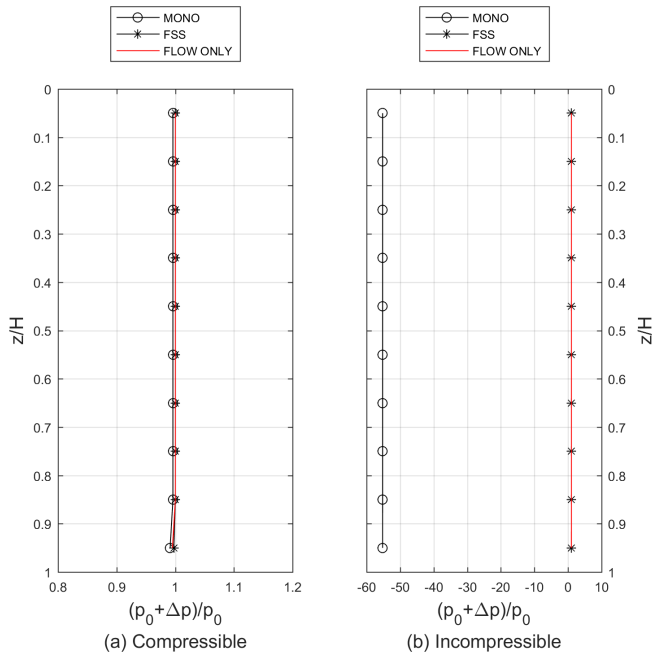

(b) Q2P0: compressible (left) and incompressible (right)

Figure 3.10: Pressure distributions for Case 2-1 with Q2Q1 (top) and Q2P0 (bottom) for both compressible and incompressible fluids.

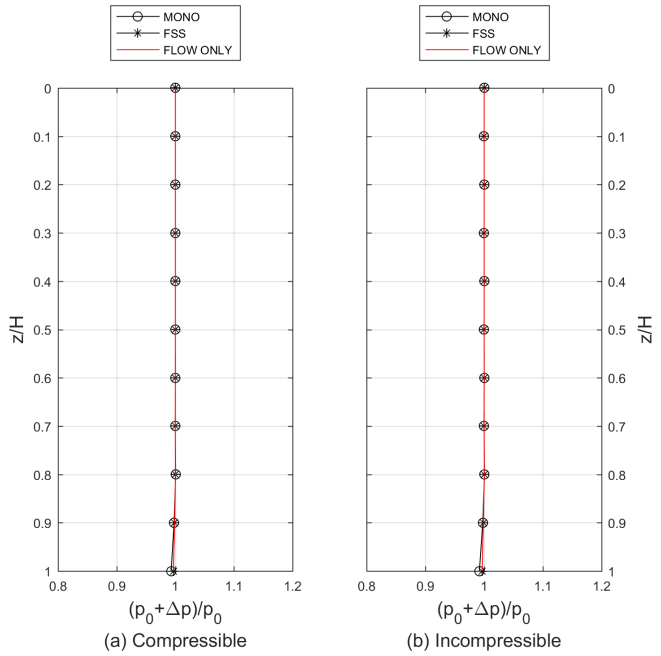

(a) Q2Q1: compressible (left) and incompressible (right)

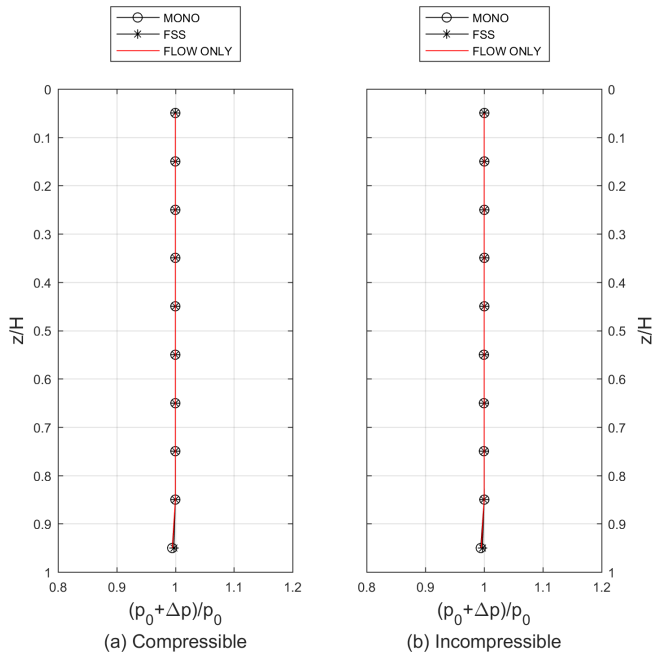

(b) Q2P0: compressible (left) and incompressible (right)

Figure 3.11: Pressure distributions for Case 2-2 with Q2Q1 (top) and Q2P0 (bottom) for both compressible and incompressible fluids.

3.3.3 Case 3: plane strain strip-footing

For Case 3, we employ a typical 2D plane strain problem with a strip-footing (Figure 3.12), known as the McNamee and Gibson problem [70, 71]. For the boundary condition of geomechanics, we apply no horizontal displacement to the left and right boundaries and no vertical displacement at the bottom.

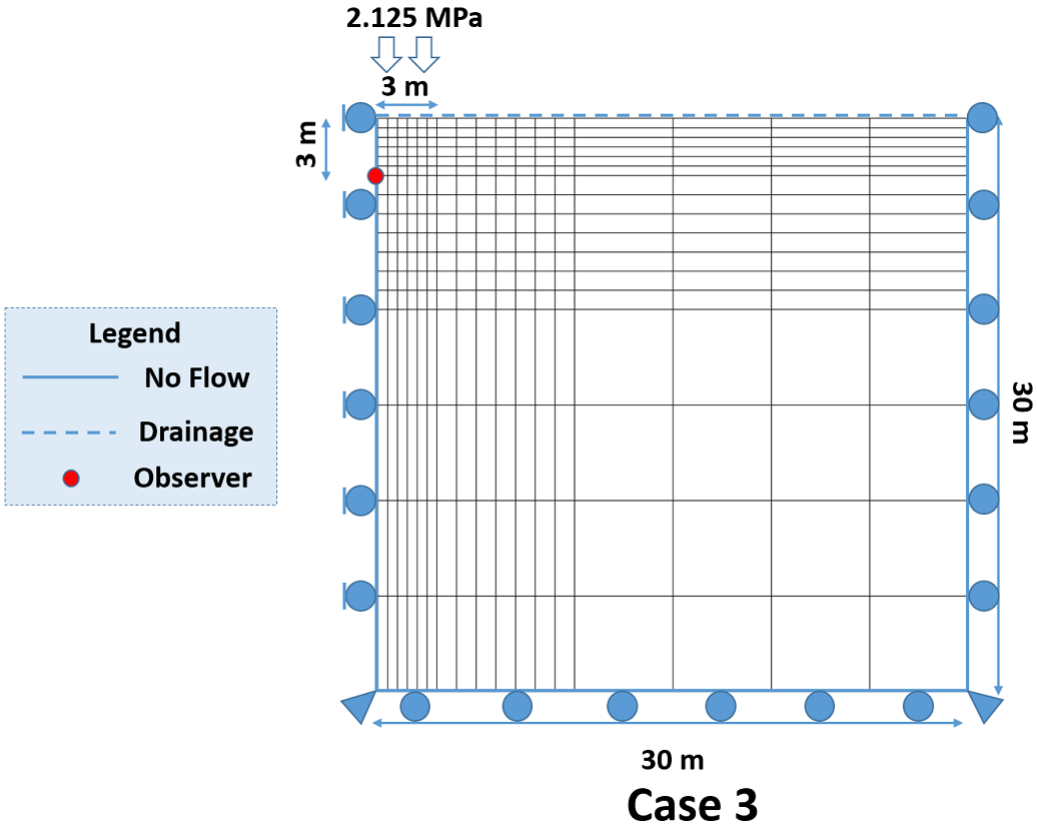

Figure 3.12: Schematics of Case 3: plane strain strip-footing (i.e., McNamee-Gibson's problem).

The overburden of 2.125 [MPa] is applied to the left 3 [m] at the top. For flow, we have no-flow boundary along the both sides and at the bottom, while the drainage boundary is

applied at the top.

For the simulation purpose, we choose the variational timestep size starting $\Delta t_0 = 1.0 \times 10^{-4}$ [s] and doubles its size every timestep until it reaches $\Delta t = 10$ [s]. In order to monitor the pressure through the simulation, we set the observer point as in Figure 3.12. The total simulation is for 200 timesteps, which is corresponding to the dimensionless time of $T = 0.8858$ for the monitoring spot. We also take a snapshot of pressure distribution for the whole domain after 10 timesteps, representing at about $t = 0.1023$ [s], with each discretization, solution strategy and fluid compressibility.

Q1Q1: For Q1Q1, we have the results similar to Case 1.

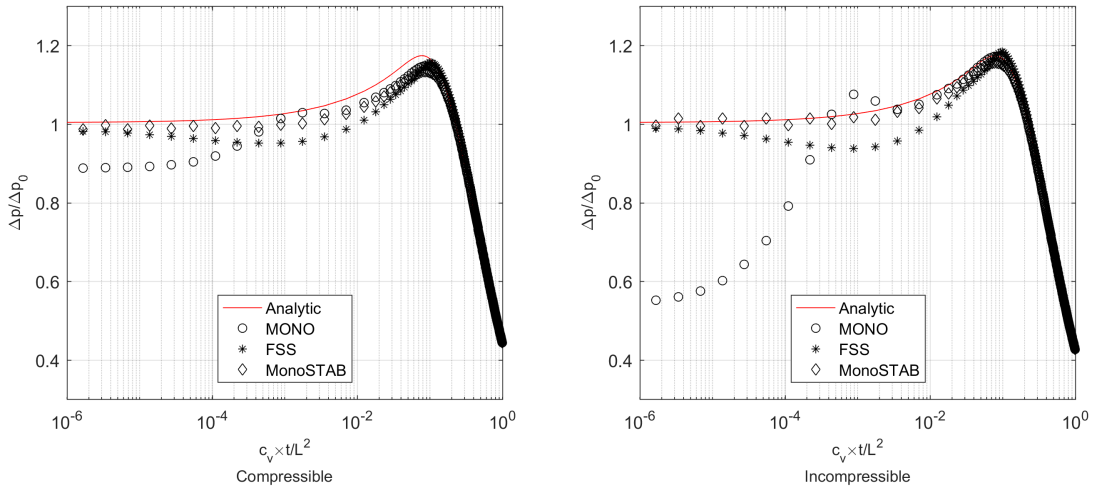

Figure 3.13: Evolutions of pressure at the monitoring point for Case 3 with Q1Q1. L=3 [m].

From Figures 3.13, small deviations from the analytical solution are found for compressible fluid (left), especially for the monolithic method at early times. This is because of discontinuity of pressure at the drainage boundary, while all the solutions match the

analytical solution at late times. For incompressible fluid (right), inaccuracy at early times becomes severer because of the violation of the inf-sup condition.

For compressible fluid, when using the monolithic method, we find from Figures 3.14 that the discontinuous pressure due to instantaneous loading mainly leads to spatial instability over the whole domain at early times ($t = 0.1023\ [s]$), particularly identifying severe oscillation around the left corner down to the $z/L_z = 0.9$ in depth. For incompressible fluid, the oscillation becomes severer at early times because of voliation of the inf-sup condition. As shown, the monolithic method is the most unstable among the methods.

Q1P0: The piecewise constant interpolation for pressure facilitates discontinuous spatial distribution induced by the instantaneous pressure jump. Figure 3.15 shows the pressure distributions from the monolithic and the fixed-stress methods when Q1P0 is used.

Both methods provide stability and accuracy for compressible and incompressible fluids, capturing the Mandel-Cryer effect correctly (Figure 3.15a). It is shown that all the solutions are stable and accurate. Albeit, note that there are some discretization errors in space between numerical and analytical solutions. No spurious pressure mode from the violation of the inf-sup condition is found for incompressible fluid, showing that Q1P0 is a more stable element pair than Q1Q1.

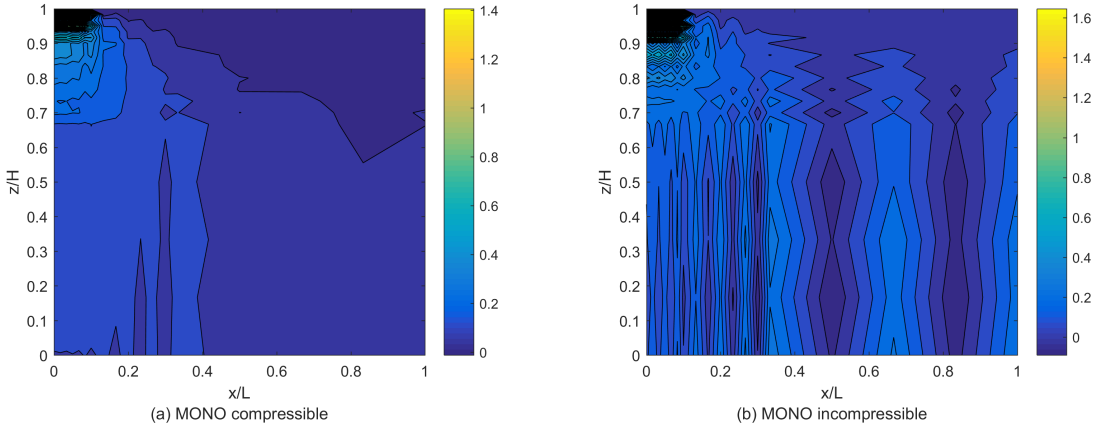

(a) Pressure distribution for the monolithic

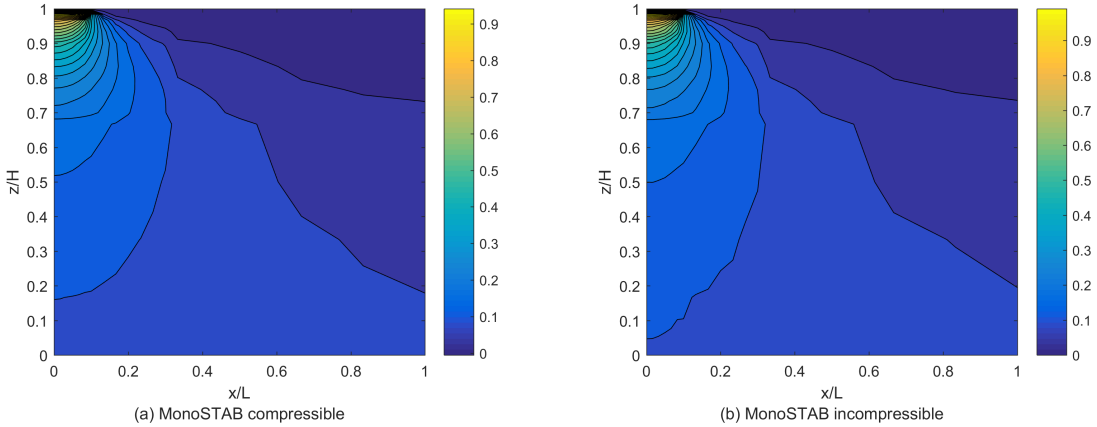

(b) Pressure distribution for the fixed-stress

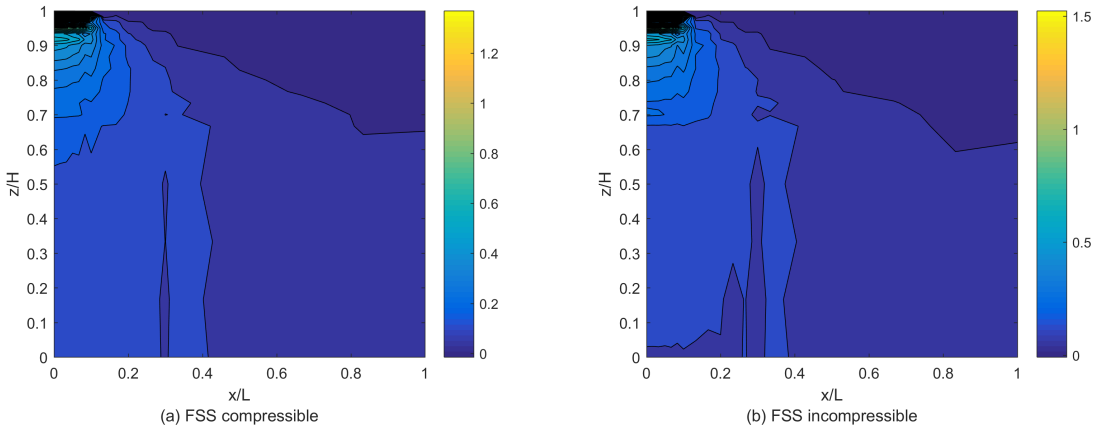

(c) Pressure distribution for the stabilized

Figure 3.14: Pressure distributions for Case 3 with Q1Q1 at the early time. Pressure is normalized by the initial overburden of 2.125 [MPa].

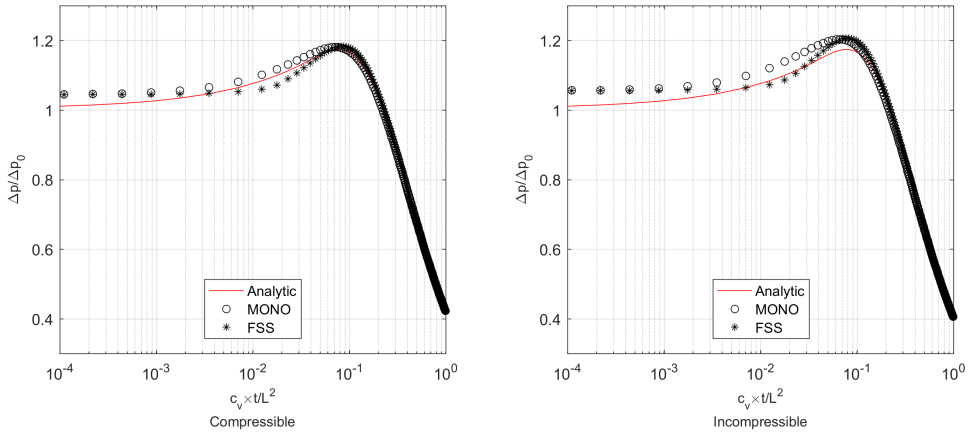

(a) Evolutions of pressure at the monitoring point for Case 3 with Q1P0. L=3 [m].

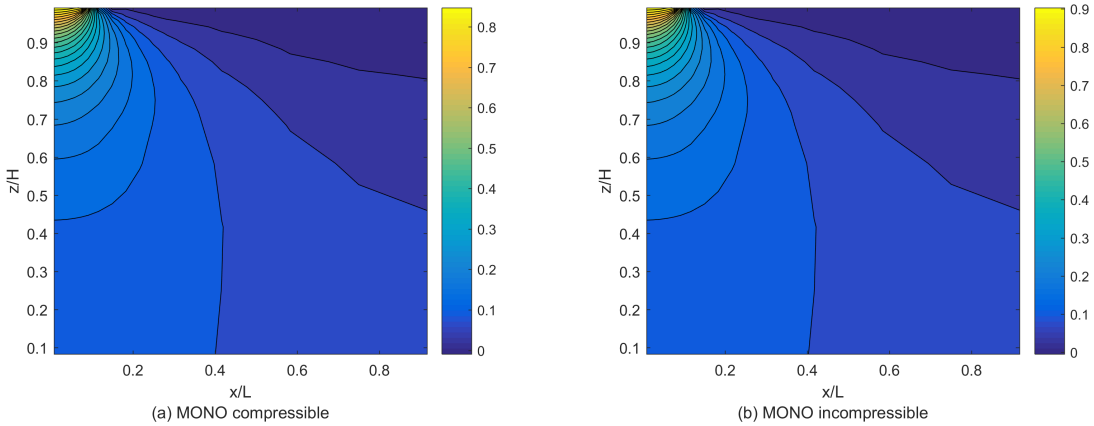

(b) Normalized pressure distribution for the monolithic at the early time

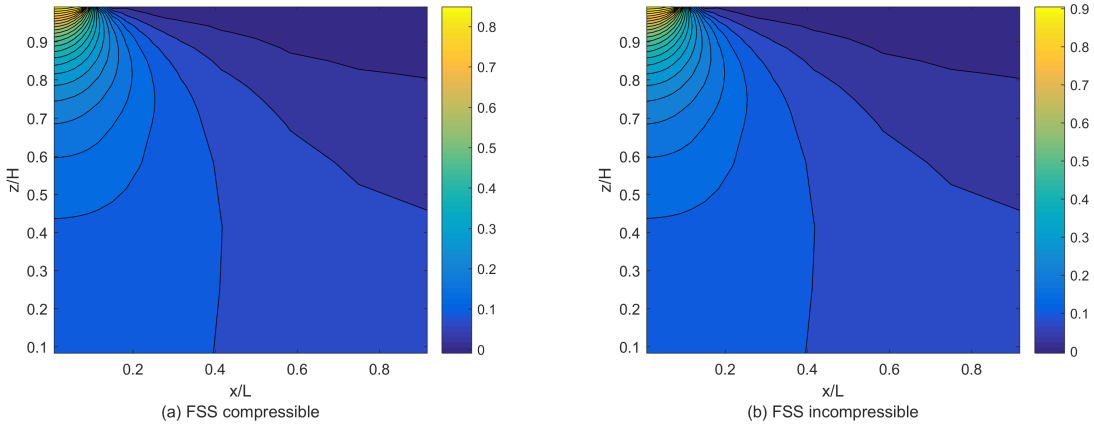

(c) Normalized pressure distribution for the fixed-stress at the early time

Figure 3.15: Pressure distributions for Case 3 with Q1P0. For (b) and (c), pressure snapshot is at $t = 0.1023$ [s] normalized by the initial overburden of 2.125 [MPa].

Q2Q1 & Q2P0: From Figures 3.16 and 3.17, we find no severe oscillations for Q2Q1 & Q2P0, when employing the monolithic and fixed-stress methods. Q2Q1 satisfies the inf-sup condition through this discretization, but we find a little oscillation near the top-left corner because of pressure discontinuity (Figures 3.16b and 3.16c), while Q2P0 shows no oscillation just like Q1P0. Still, both element choices show stable and accurate results, capturing the Mandel-Cryer effect well. The monolithic and fixed-stress methods yield stability for both compressible and incompressible fluids.

3.4 Summary

In this chapter, we studied spatial stability for poromechanics problems with various mixed space discretizations (i.e., Q1Q1, Q1P0, Q2Q1, Q2P0). We identified two causes of spurious oscillation: discontinuity of pressure at the drainage boundary and the violation of the inf-sup condition. For the pressure discontinuity, a piecewise continuous interpolation of pressure (or higher-order interpolation) can cause spatial oscillation at early times, while the piecewise constant interpolation of pressure yields stability. Also, we found that lower approximations of pressure than displacement (Q2Q1, Q1P0, Q2P0) yielded small or no oscillation. Whereas, we confirmed that the equal-order approximation of pressure and displacement (Q1Q1) caused severe oscillation. For an incompressible fluid, Q2Q1 was better than Q1P0, when we use the monolithic method, because Q1P0 might not satisfy the inf-sup condition. However, we found that the fixed-stress sequential method can circumvent violation of the inf-sup condition, including Q1Q1 and Q1P0, as well as that it can also stabilize the oscillation of the pressure discontinuity for Q1Q1. Since poromechanics deal with different physics to solve, related to fluid flow and soil or rock (geomaterial), which have different physical properties, it also naturally leads to the fact that mixed formulations for spatial discretization need to be considered for more accurate numerical solutions. Through the chapter, it is shown that the fixed-stress split can naturally

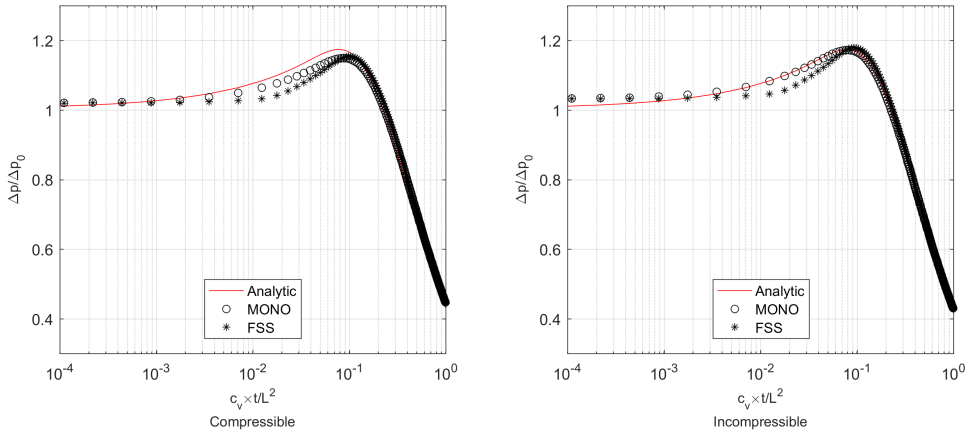

(a) Evolutions of pressure at the monitoring point for Case 3 with Q2Q1. L=3 [m].

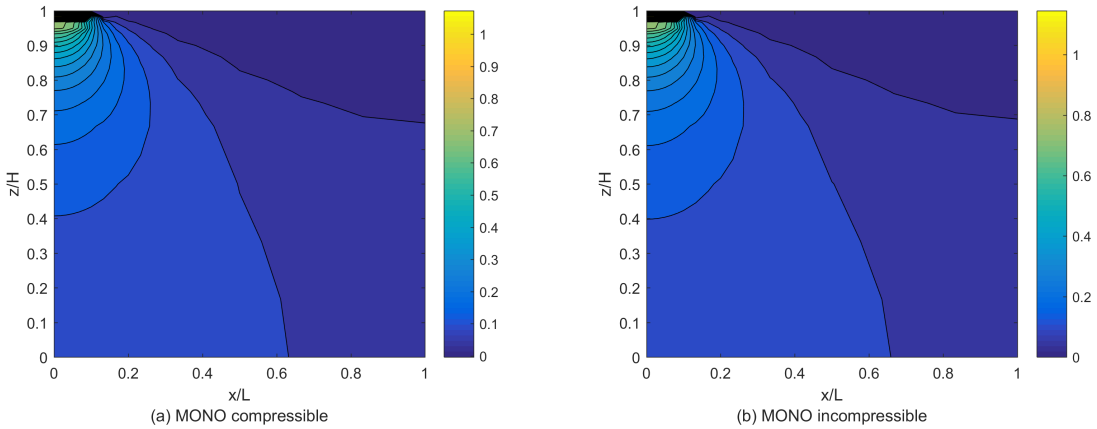

(b) Normalized pressure distribution for the monolithic at the early time

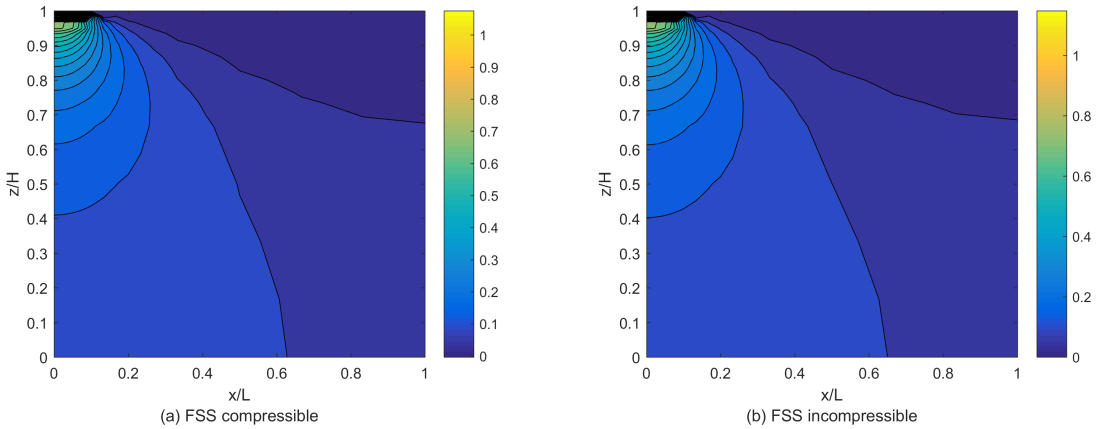

(c) Normalized pressure distribution for the fixed-stress at the early time

Figure 3.16: Pressure distributions for Case 3 with Q2Q1. For (b) and (c), pressure snapshot is at $t = 0.1023$ [s] normalized by the initial overburden of 2.125 [MPa].

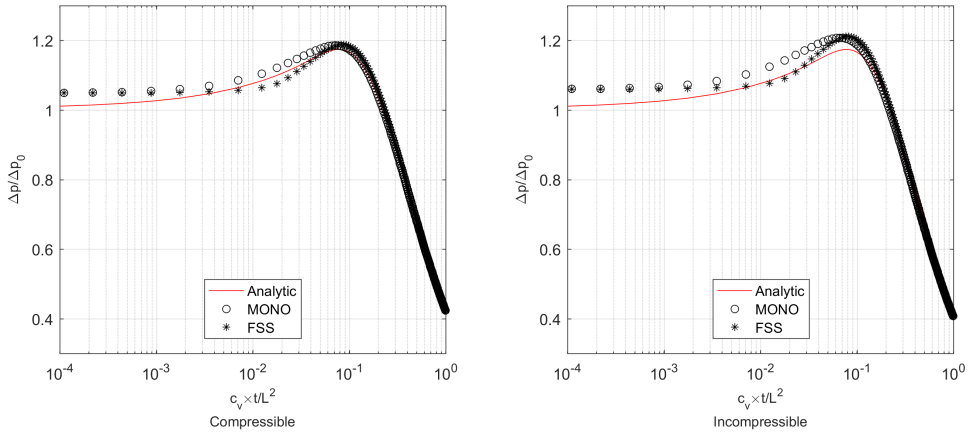

(a) Evolutions of pressure at the monitoring point for Case 3 with Q2P0. L=3 [m].

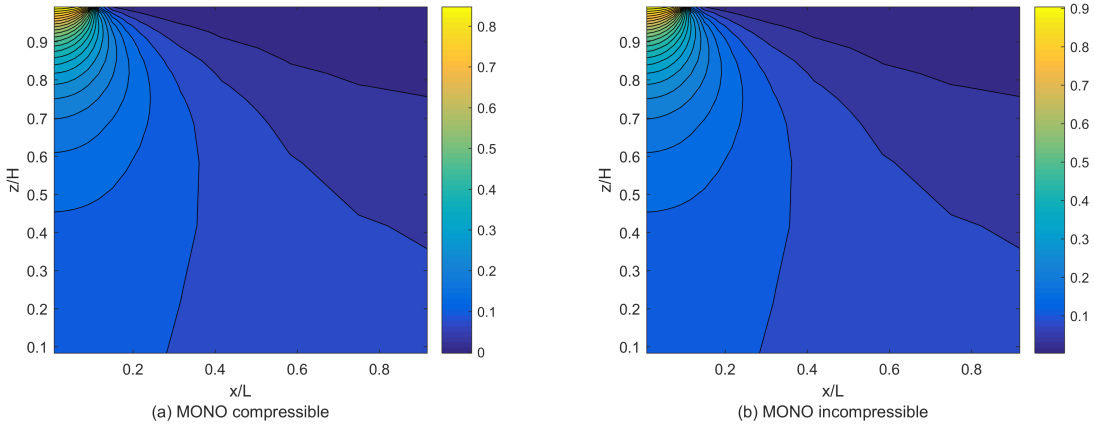

(b) Normalized pressure distribution for the monolithic at the early time

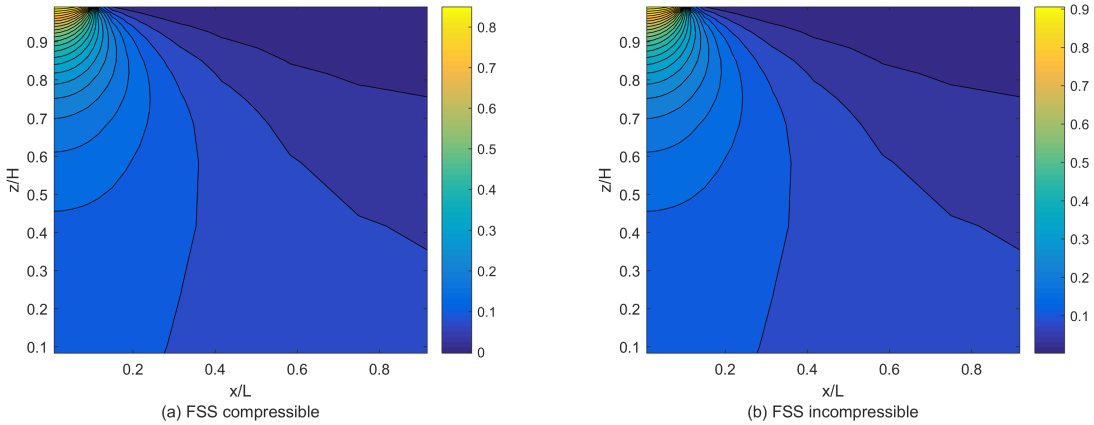

(c) Normalized pressure distribution for the fixed-stress at the early time

Figure 3.17: Pressure distributions for Case 3 with Q2P0. For (b) and (c), pressure snapshot is at $t = 0.1023$ [s] normalized by the initial overburden of 2.125 [MPa].

overcome the two spatial oscillations which can dominate at an early time of simulation for poromechanics.

4. ACCURACY IN TIME INTEGRATION

4.1 Introduction for Accuracy in Time Integration

In the numerical analysis literature, accuracy of solution measures errors resulting from spatial and temporal discretizations. The order of accuracy quantifies the convergence rate or degree of consistency of the numerical solution, approaching the true solution of the original differential equation [43]. For reservoir simulation, after spatial discretization, the initial value problem results in a system of ODEs, and the time derivative term is approximated using the finite difference method. If the typical backward Euler method (the fully implicit method) is employed, stability (A-stable) is achieved and the first-order of accuracy in time is obtained [72].

On the other hand, high-order of accuracy in time is also desired in computational mechanics when the sensitivity of other parameters is significant, depending on the flow of motion. Furthermore, for a complex domain, spatial discretization itself needs high-order approximations and it requires the high-order temporal discretizations.

There are broadly two types of high-order schemes for ODE integrators to advance in time [42]. One is the multi-step (or multi-value) approach, targeting higher gradients approximation (e.g., the backward differentiation formula (BDF)). The other is the classical family of Runge-Kutta (RK) methods categorized as an one-step or a starting method. However, both methods are not appropriate for large systems, such as reservoir simulation, in terms of their computational efficiency. The multi-step methods unlike the one-step method have large storage requirements and computations for higher derivatives, which need to be prepared at each timestep. In addition, it is known that the implicit BDF may not be stable for high-orders [42, 72]. Although the RK methods do not require derivative calculations generally, this approach still needs multiple functions to evaluate

recursively within a timestep, such that the number of functions per timestep equals the order of method [73].

In this point of view, for large scale simulation the deferred or defect correction (DC) [74, 34] can be a more efficient method for high-order time integration. The advantages over the aforementioned approaches are that it is easy to construct an error-correction equation using the original equation for any desired order of accuracy, and that it is a one-step method, where there is no need to store values other than previous time calculation. The DC is based on a scheme that accelerates the convergence rate of low-order. Using the error equation, which has the same structure as the original, and applying the lower order solution to the original scheme, it removes the low-order term in the truncated error and obtains the high-order solution [74, 75, 34].

As aforementioned, poromechanics is a system of DAEs that has different physics and disparity in time scales for its subsystems. In other words, for example in this thesis the geomechanics is assumed to be quasi-static, while the flow is assumed to contain transient/time-dependent physical processes. Thus, it is natural that we can apply different time integration schemes for the sub-equations. This application is another superiority of the sequential scheme to the monolithic scheme for poromechanics [41].

There is a recent study to implement the DC to the DAEs index-1 system. Vijalapura et al. [34] used the fractional step (the operator splitting) scheme to apply the DC method. They also studied a symmetric splitting as Strang's spitting [76], named the two-pass algorithm, known as a high-order scheme in ODEs. They found that the desired high-order in time is only reached by the DC method in DAEs index-1 system, not by the two-pass algorithm.

We use these two-pass algorithm and DC for the high-order scheme in poromechanics using the fixed-stress split in this chapter. Then, we compare the two-pass algorithm and DC for the poromechanics problems. The selection of both methods is natural be-

cause they are simple to construct, based on the operator splitting schemes, using the typical Euler's method for reservoir simulation. By combining time integration schemes for sub-problems, the operator splitting method provides an efficient scheme for the overall problem [77]. Likewise, the sequential part or partitioned operator in the sequential scheme (e.g., the fixed-stress split) is itself based on operator splitting, with each operator representing a specific physics among multiphysics.

Through the splitting schemes, one can apply different time integration schemes on different operators or disparate partitions. For example, for the DC method, we apply the correction step or operator to the pure ODE system, that is, the flow equation only, with the geomechanical constraint. Specifically, we choose the spectral DC (SDC) method [75] proposed by Dutt et al. instead of the classical DC (CDC) in order to avoid the numerical instabilities. Because the construction of error equations in the CDC involves numerical differentiation of error, which may cause the numerical instabilities, thus Dutt et al. have proposed a stable method, called SDC with application of the Picard-type integral equation without approximation for the derivative of the error terms.

In this chapter, we analyze the two-pass and SDC methods as high-order methods in time integration for the fixed-stress split. To study the order of accuracy, we employ the Taylor series expansion for the fixed-stress split and two high-order methods: the two-pass and SDC methods. Then, in the numerical experiments, we take representative tests, such as Terzaghi's (1D) consolidation and strip-footing plane strain (2D) problems with isothermal linear poroelasticity. For spatial discretizations, we use the standard FEM for displacement and the FVM for pressure: the Q1P0 pair, aforementioned in the former chapter.

We show that both methods, as high-order methods in time integration, do not enhance the order of accuracy. For the two-pass algorithm, we find that the order reduction occurs because poromechanics results in a system of DAEs due to the geomechanics operator

working as the constraint to the flow operator. For the SDC method, the flow equation of poromechanics has its own structure that reduces the convergence rate, albeit correcting errors. Even though the errors are reduced by both methods, the computational effort required at each timestep is higher than that of the original system, thus we conclude that the fixed-stress split (a kind of one-pass method) itself is sufficient for the reservoir simulation in poromechanics.

4.2 Two-Pass and SDC Algorithms

Starting from the fixed-stree split, the Equation 2.35 in the Mathematical Formulations chapter, let the operators $\mathcal{A}_{ss}^{p}$ be Φ and $\mathcal{A}_{ss}^{u}$ be Ξ like Equation 2.27. It can be found that the fixed-stress split scheme itself solves the DAEs by operator splitting or the fractional step method and it is categorized as the one-pass method. In other words, the fixed-stress scheme has the sequence of operators as follows:

$$\cdots \Phi_h \circ \Xi_h \circ \Phi_h \circ \underbrace{\Xi_h \circ \Phi_h}_{timestep1}, \tag{4.1}$$

where Φ_h and Ξ_h are the discretized operators of Φ and Ξ respectively with timestep size h.

4.2.1 Two-pass algorithm

The two-pass algorithm is a type of symmetric operator splitting algorithm based on Strang's splitting where conserving the structure is the key for its stability and convergence. [76, 34]. Then for the two-pass algorithm with the fixed-stress split, we split only the first operator in half in Equation 4.1, since the fluid flow (Φ) is transient and the geomechanics (Ξ) is quasi-static based on our assumptions.

Then the two-pass algorithm for the fixed-stress is taking its form as follows:

$$\cdots \Phi_{h/2} \circ \Xi_h \circ \Phi_{h/2} \circ \underbrace{\Phi_{h/2} \circ \Xi_h \circ \Phi_{h/2}}_{timestep1}. \tag{4.2}$$

4.2.2 SDC algorithm

Dutt et al. [75] has proposed the SDC method modifying the classical DC or defect correction method [74]. Unlike the classical DC, the SDC doesn't need to take the derivative solving errors in error equations, thus it leads to numerically stable solutions [75].

Suppose we have an initial value problem,

$$u_t = Lu, \quad u(0) = u_0, \tag{4.3}$$

where u_t is time derivative of u and L is a differential operator, having Lipschitz-continuity in variable u and time t, through which the existence and the uniqueness of the solution are guaranteed [33, 72, 42]. The solution of the original ODE 4.3 can be written in terms of the Picard integral equation [72, 73] as

$$u(t) = u_a + \int_a^t Lu(\tau, u(\tau))d\tau, \tag{4.4}$$

where $u(t = t_a) = u_a$.

From Equation 4.4, we can define the residual function R to measure the quality of approximation of the time integration as:

$$R(t) \equiv u_a + \int_a^t Lu(\tau, \tilde{u}(\tau))d\tau - \tilde{u}(t), \tag{4.5}$$

where $\tilde{u}(t)$ is the approximation solution for $u(t)$.

Then we derive the error equation $e(t)$ for the SDC method as:

$$e(t) = R(t) + \int_a^t Lu(\tau, \tilde{u}(\tau) + e(\tau))d\tau - \int_a^t Lu(\tau, \tilde{u}(\tau))d\tau, \tag{4.6}$$

through which we can obtain the error without any numerical differentiation term leading to numerical stability.

Now we can obtain the error for the backward Euler (or implicit) method especially expressed as:

$$e_{i+1} = e_i + \Delta t(Lu(t_{i+1}, u_{i+1} + e_{i+1}) - Lu(t_{i+1}, u_{i+1})) + R(t_{i+1}) - R(t_i), \tag{4.7}$$

where $e_i = e(t_i)$ and

$$R(t_{i+1}) - R(t_i) = \int_{t_i}^{t_{i+1}} Lu(\tau, \tilde{u}(\tau))d\tau - (u_{i+1} - u_i). \tag{4.8}$$

Thus, from Equation 4.7 and 4.8, we can obtain the corrected new solution $u_{i+1,N}$ as:

$$\begin{aligned} u_{i+1,N} = u_{i+1} + e_{i+1} = u_i + e_i + \Delta t(Lu(t_{i+1}, u_{i+1} + e_{i+1}) - Lu(t_{i+1}, u_{i+1})) \\ + \int_{t_i}^{t_{i+1}} Lu(\tau, \tilde{u}(\tau))d\tau. \end{aligned} \tag{4.9}$$

having the same structure as the original time marching scheme, the inherent property of the deferred correction method.

Thus, Equation 4.9 is leading to how we perform the numerical approximation of the integral including $\int_{t_i}^{t_{i+1}} Lu(\tau, \tilde{u}(\tau))d\tau$ and it depends on the sub-nodes, the quadrature points between t_i and t_{i+1} and this is why it is called SDC.

If we have 1 to m sub-nodes for $[t_i, t_{i+1}]$ for example, then the numerical algorithm

for SDC is as:

1. Compute an approximation solution at the sub-nodes 1 to m

2. Compute successive corrections expressed as:

Do $j = 1$ to m

Do $k = 0$ to $m-1$

$$u_{i+1}^j + e_{i+1}^j = u_i^j + e_i^j + \Delta t(Lu(t_{i+1}^j, u_{i+1}^j + e_{i+1}^j) - Lu(t_{i+1}^j, u_{i+1}^j)) + \int_{t_k}^{t_{k+1}} Lu(\tau, \tilde{u}(\tau))d\tau$$

End Do

End Do (4.10)

4.3 Error Analysis of the Monolithic Method

Following [20], Equation 2.27 and 2.31 in the previous chapter can be expressed matrix form with $\boldsymbol{U}$and $\boldsymbol{P}$ which are spatially discretized before time discretization as[1]

$$\underbrace{\begin{bmatrix} \boldsymbol{K} & -\boldsymbol{L}^T \\ \boldsymbol{0} & \boldsymbol{T} \end{bmatrix}}_{\boldsymbol{C}} \underbrace{\begin{bmatrix} \boldsymbol{U} \\ \boldsymbol{P} \end{bmatrix}}_{\boldsymbol{x}} - \underbrace{\begin{bmatrix} \boldsymbol{0} & \boldsymbol{0} \\ \boldsymbol{L} & \boldsymbol{Q} \end{bmatrix}}_{\boldsymbol{D}} \underbrace{\begin{bmatrix} \dot{\boldsymbol{U}} \\ \dot{\boldsymbol{P}} \end{bmatrix}}_{\dot{\boldsymbol{x}}} = \underbrace{\begin{bmatrix} \boldsymbol{s}^u \\ \boldsymbol{s}^p \end{bmatrix}}_{\boldsymbol{s}}, \tag{4.11}$$

where $\boldsymbol{K}, \boldsymbol{L}, \boldsymbol{Q}$ are following Equation 2.32, 2.33, 2.34 and $\boldsymbol{T}$ are the transmissibility matrix. Note that for linear poroelasticity problem the whole system is expressed into a linear ODE by following the MOL approach with $\boldsymbol{C}, \boldsymbol{D}, \boldsymbol{s}$ and $\boldsymbol{x}$.

$$\boldsymbol{C}\boldsymbol{x} - \boldsymbol{D}\dot{\boldsymbol{x}} = \boldsymbol{s}. \tag{4.12}$$

[1] See Appendix A.

When $\tilde{\boldsymbol{x}}$ along with $\tilde{\boldsymbol{U}}$ and $\tilde{\boldsymbol{P}}$ is a discretized variable both in space and time, the Equation 4.11 and 4.12 is taking a discretized form with a backward Euler method as

$$\underbrace{(\Delta t\boldsymbol{C}-\boldsymbol{D})}_{\boldsymbol{A}}\tilde{\boldsymbol{x}}^{n+1}=\underbrace{-\boldsymbol{D}}_{\boldsymbol{B}}\tilde{\boldsymbol{x}}^{n}+\underbrace{\Delta t\boldsymbol{s}^{n+1}}_{\boldsymbol{f}}. \tag{4.13}$$

Then it can be expressed as

$$\tilde{\boldsymbol{x}}^{n+1}-\boldsymbol{A}^{-1}\boldsymbol{B}\tilde{\boldsymbol{x}}^{n}-\boldsymbol{A}^{-1}\boldsymbol{f}=\boldsymbol{0}. \tag{4.14}$$

Let us we have the true solution of $\boldsymbol{x}$ for $t=t_{n+1}$ and $t=t_n$ as $\boldsymbol{x}(t_{n+1})$ and $\boldsymbol{x}(t_n)$ and if $\tilde{\boldsymbol{x}}^{n+1}=\boldsymbol{x}(t_{n+1})$ as exact solution, then from Equation 4.14,

$$\boldsymbol{x}(t_{n+1})-\boldsymbol{A}^{-1}\boldsymbol{B}\boldsymbol{x}(t_n)-\boldsymbol{A}^{-1}\boldsymbol{f}=\boldsymbol{e}_{n+1}, \tag{4.15}$$

where $\boldsymbol{e}_{n+1}$ is the error due to truncation at $t=t_{n+1}$.

From Taylor expansion (Equation 2.1),

$$\boldsymbol{x}(t_n)=\boldsymbol{x}(t_{n+1})-\Delta t\dot{\boldsymbol{x}}(t_{n+1})+\frac{\Delta t^2}{2!}\ddot{\boldsymbol{x}}(t_{n+1})+O(\Delta t^3). \tag{4.16}$$

Since $\boldsymbol{x}(t_{n+1})$ as a true solution satisfies the following equation from Equation 4.12,

$$\boldsymbol{C}\boldsymbol{x}(t_{n+1})-\boldsymbol{D}\dot{\boldsymbol{x}}(t_{n+1})=\boldsymbol{s}, \tag{4.17}$$

then, from Equation 4.15, and 4.17,

$$\boldsymbol{e}_{n+1}=-\frac{1}{2}\ddot{\boldsymbol{x}}(t_{n+1})\Delta t^2+\frac{1}{2}\boldsymbol{A}^{-1}\boldsymbol{C}\ddot{\boldsymbol{x}}(t_{n+1})\Delta t^3+O(\Delta t^4), \tag{4.18}$$

where the local error of the monolithic is $\boldsymbol{e}_{n+1} \sim O(\Delta t^2)$, meaning that the global error is convergent to $O(\Delta t)$. This property will be addressed in more detail in the following section for the fixed-stress split error analysis.

4.4 Error Analysis of the Fixed-Stress Split

Before we perform the local and global error analysis for the fixed-stress split, here we first postulate a function ψ derived from the constraint function of geomechanics for momentum balance, g in Equation 2.27 that is for operator Ξ. Using the implicit function theorem[2], the following relations for near a solution are induced as:

$$\boldsymbol{U} = \psi(\boldsymbol{P}), \;\; \dot{\boldsymbol{U}} = \dot{\psi}(\boldsymbol{P}), \tag{4.19}$$

where $\dot{()}$ is time derivative of a function.

Then it is leading to a pure ODE system for flow expressed as:

$$\Phi : \dot{\boldsymbol{P}} = f(\dot{\psi}(\boldsymbol{P}), \boldsymbol{P}). \tag{4.20}$$

4.4.1 Local Error Analysis

Local error is defined as a discretized error between timesteps [72, 73]. From Equation 2.27 and 4.1, the variable $\boldsymbol{U}$ and $\boldsymbol{P}$ are approximated in space but not in time, yet. Here we study the local error of $\Xi_h \circ \Phi_h$ in Equation 4.1 for the fixed-stress split.

For the local error analysis of $\Xi_h \circ \Phi_h$, we perform Taylor expansion for $t \in [t_n, t_{n+1}]$.

[2]Implicit function theorem is a principle telling that if there is a solution where it is smooth enough to have partial derivatives for multivariable function on some conditions, then there is a implicit function around that solution satisfying such as Equation 4.19 although it is not explicitly expressed. Another example can be representing a graph of a function by relation between variables on specific regions or a coordinate transformation if mapping function is not singular, that is, the determinant of Jacobian is not zero.

From the exact or true solution of $\boldsymbol{P}(t_n)$ at $t = t_n$, Taylor expansion of $\boldsymbol{P}$ provides

$$\boldsymbol{P}(t_{n+1}) = \boldsymbol{P}(t_n) + \Delta t\dot{\boldsymbol{P}}(t_n) + \frac{\Delta t^2}{2!}\ddot{\boldsymbol{P}}(t_n) + O(\Delta t^3)$$

(from Equation 2.27)

$$= \boldsymbol{P}(t_n) + \Delta t f(\dot{\boldsymbol{U}}(t_n), \boldsymbol{P}(t_n)) + \frac{\Delta t^2}{2!}\ddot{\boldsymbol{P}}(t_n) + O(\Delta t^3)$$

(from Equation 4.19)

$$\begin{aligned} = \boldsymbol{P}(t_n) &+ \Delta t f(\dot{\psi}(\boldsymbol{P}(t_n)), \boldsymbol{P}(t_n)) \\ &+ \frac{\Delta t^2}{2!}\partial_{\boldsymbol{U}} f(\dot{\psi}(\boldsymbol{P}(t_n)), \boldsymbol{P}(t_n))\ddot{\psi}(\boldsymbol{P}(t_n)) \\ &+ \frac{\Delta t^2}{2!}\partial_{\boldsymbol{P}} f(\dot{\psi}(\boldsymbol{P}(t_n)), \boldsymbol{P}(t_n))\dot{\boldsymbol{P}}(t_n) + O(\Delta t^3), \end{aligned} \tag{4.21}$$

where $\partial_{\boldsymbol{U}} f = \frac{\partial f}{\partial \boldsymbol{U}}$ and $\partial_{\boldsymbol{P}} f = \frac{\partial f}{\partial \boldsymbol{P}}$.

If the approximate solution for $\boldsymbol{P}$ is $\tilde{\boldsymbol{P}}$ and we assume $\tilde{\boldsymbol{P}}_n$ satisfies $\tilde{\boldsymbol{P}}_n = \boldsymbol{P}(t_n)$ for the local error analysis starting from the exact solution, then for the discretized Φ_h where an approximate solution $\tilde{\boldsymbol{P}}_{n+1}$ at $t = t_{n+1}$ expressed as

$$\begin{aligned} \tilde{\boldsymbol{P}}_{n+1} =& \tilde{\boldsymbol{P}}_n + \Delta t f(\dot{\psi}(\tilde{\boldsymbol{P}}_n), \tilde{\boldsymbol{P}}_n) + \frac{\Delta t^2}{2!}\partial_{\boldsymbol{U}} f(\dot{\psi}(\tilde{\boldsymbol{P}}_n), \tilde{\boldsymbol{P}}_n)\partial_t\dot{\psi}(\tilde{\boldsymbol{P}}_n) \\ &+ \frac{\Delta t^2}{2!}\partial_{\boldsymbol{P}} f(\dot{\psi}(\tilde{\boldsymbol{P}}_n), \tilde{\boldsymbol{P}}_n)\dot{\tilde{\boldsymbol{P}}}(t_n) + O(\Delta t^3). \end{aligned} \tag{4.22}$$

Since we have the fixed constraint with true solution as $\boldsymbol{U}(t_n) = \psi(\boldsymbol{P}(t_n))$ and $\dot{\boldsymbol{U}}(t_n) = \dot{\psi}(\boldsymbol{P}(t_n))$ at $t = t_n$, fixing the rate of stress as $\delta\dot{\boldsymbol{\sigma}} = \boldsymbol{0}$ for the fixed-stress split, Equation 4.22 yields

$$\tilde{\boldsymbol{P}}_{n+1} = \boldsymbol{P}(t_n) + \Delta t f(\dot{\psi}(\boldsymbol{P}(t_n)), \boldsymbol{P}(t_n)) + \frac{\Delta t^2}{2!}\partial_{\boldsymbol{P}} f(\dot{\psi}(\boldsymbol{P}(t_n)), \boldsymbol{P}(t_n))\dot{\boldsymbol{P}}(t_n) + O(\Delta t^3). \tag{4.23}$$

Then the local error for $\boldsymbol{P}$ within $t \in [t_n, t_{n+1}]$, that is, $\tilde{\boldsymbol{P}}_{n+1} - \boldsymbol{P}(t_{n+1})$ is by extracting

Equation 4.21 from Equation 4.23 as

$$\tilde{\boldsymbol{P}}_{n+1} - \boldsymbol{P}(t_{n+1}) = \boldsymbol{e}_{n+1}\Delta t^2 + O(\Delta t^3), \tag{4.24}$$

where $\boldsymbol{e}_{n+1}$ is the error induced from the splitting (including the fixing the rate of stress change for the fixed-stress split).

Then, we move to the geomechanics operator Ξ_h as in Equation 4.1 seeking for the approximate solution of $\boldsymbol{U}(t_{n+1})$ expressed as $\tilde{\boldsymbol{U}}_{n+1}$. Since $\tilde{\boldsymbol{P}}_{n+1} = \boldsymbol{P}(t_{n+1}) + \boldsymbol{e}_{n+1}\Delta t^2 + O(\Delta t^3)$ (Equation 4.24) and using linear property of function ψ,

$$\begin{aligned} \tilde{\boldsymbol{U}}_{n+1} = \psi(\tilde{\boldsymbol{P}}_{n+1}) &= \psi(\boldsymbol{P}(t_{n+1}) + \boldsymbol{e}_{n+1}\Delta t^2 + O(\Delta t^3)) \\ &= \psi(\boldsymbol{P}_{n+1}) + \Delta t^2 \psi(\boldsymbol{e}_{n+1}) + O(\Delta t^3). \end{aligned} \tag{4.25}$$

Because the true solution for displacement is

$$\boldsymbol{U}_{n+1} = \psi(\boldsymbol{P}_{n+1}), \tag{4.26}$$

then from Equation 4.25 and 4.26, the local error for $\boldsymbol{U}$ becomes

$$\tilde{\boldsymbol{U}}_{n+1} - \boldsymbol{U}(t_{n+1}) = \Delta t^2 \psi(\boldsymbol{e}_{n+1}) + O(\Delta t^3). \tag{4.27}$$

Thus from Equation 4.24 and 4.27, $\Xi_h \circ \Phi_h$ has the local error of $O(\Delta t^2)$ from the true solutions, $\boldsymbol{P}(t_n)$ and $\boldsymbol{U}(t_n)$.

4.4.2 Global Error Analysis

Global error is attributed to the propagation and accumulation of the local errors. Assuming a standard Lipschitz condition for the local error, and for a single step method such as the Euler method, the convergence is obtained for the global error [72, 47]. Although

we do not perform the actual convergence analysis for error in this study, it can be done using the Gronwall's inequality [34].

Because the accumulation of the errors is proportional to the number of timesteps, which can be expressed as $O(\Delta t^{-1})$ for the uniformly discretized equation, we can easily infer the order of accuracy for global error by multiplying $O(\Delta t^{-1})$ to the order of accuracy for the local error obtained from the local error analysis.

Since the fixed-stress split has the local error of $O(\Delta t^2)$ starting from the exact solutions as analyzed above, we can deduce that the fixed-stress split, the one-pass algorithm, is globally the first-order of accuracy, $O(\Delta t)$, in time.

4.5 Error Analysis of the Two-Pass Algorithm

With the same manner of these error analysis for the fixed-stress split, we perform the error analysis of the two-pass algorithm for the fixed-stress split. As expressed with the discretized operators as Equation 4.2, the global error of the two-pass algorithm for the fixed-stress split can be analyzed with the local error analysis just as the same way as the one-pass algorithm, the fixed-stress split above.

Rather tedious but we can easily derive that the local error of the first step, $\Phi_{h/2} \circ \Xi_h \circ \Phi_{h/2}$ in Equation 4.2 has $O(\Delta t^2)$ likewise the one-pass fixed-stress split and thus globally $O(\Delta t)$ in time. Let us start with exact solutions $\boldsymbol{P}(t = t_n)$ and likewise Equation 4.24, we have

$$\tilde{\boldsymbol{P}}_{n+1/2} - \boldsymbol{P}(t_{n+1/2}) = O(\Delta t^2). \tag{4.28}$$

Using Equation 4.23 with fixing the rate of stress,

$$\begin{aligned}\tilde{\boldsymbol{P}}_{n+1} =& \tilde{\boldsymbol{P}}_{n+1/2} + \frac{\Delta t}{2} f(\dot{\psi}(\tilde{\boldsymbol{P}}_{n+1/2}), \tilde{\boldsymbol{P}}_{n+1/2}) \\ &+ \frac{\Delta t^2}{4 \cdot 2!} \partial_{\boldsymbol{P}} f(\dot{\psi}(\tilde{\boldsymbol{P}}_{n+1/2}), \tilde{\boldsymbol{P}}_{n+1/2}) \dot{\tilde{\boldsymbol{P}}}_{n+1/2} + O(\Delta t^3),\end{aligned} \tag{4.29}$$

and since originally it is true that

$$\begin{aligned}\boldsymbol{P}_{n+1} =& \boldsymbol{P}_{n+1/2} + \frac{\Delta t}{2} f(\dot{\psi}(\boldsymbol{P}_{n+1/2}), \boldsymbol{P}_{n+1/2}) \\ &+ \frac{\Delta t^2}{4 \cdot 2!} \partial_{\boldsymbol{U}} f(\dot{\psi}(\boldsymbol{P}_{n+1/2}), \boldsymbol{P}_{n+1/2}) \partial_t \dot{\psi}(\boldsymbol{P}_{n+1/2}) \\ &+ \frac{\Delta t^2}{4 \cdot 2!} \partial_{\boldsymbol{P}} f(\dot{\psi}(\boldsymbol{P}_{n+1/2}), \boldsymbol{P}_{n+1/2}) \dot{\boldsymbol{P}}(t_{n+1/2}) \\ &+ O(\Delta t^3),\end{aligned} \tag{4.30}$$

where $\boldsymbol{P}_{n+1/2} = \boldsymbol{P}(t_{n+1/2})$, the exact solution at $t = t_{n+1/2}$. Thus from Equation 4.28, 4.29 and 4.30,

$$\tilde{\boldsymbol{P}}_{n+1} - \boldsymbol{P}(t_{n+1}) = O(\Delta t^2). \tag{4.31}$$

The only difference is in Ξ_h. Unlike the one-pass split, when updating Ξ_h for $t = t_{n+1}$, we ought to use $\tilde{\boldsymbol{P}}_{n+1/2}$ in approximating $\boldsymbol{U}(t_{n+1})$ and obtain $\tilde{\boldsymbol{U}}_{n+1} = \psi(\tilde{\boldsymbol{P}}_{n+1/2})$, resulting in

$$\tilde{\boldsymbol{U}}_{n+1} - \boldsymbol{U}(t_{n+1}) = O(\Delta t). \tag{4.32}$$

Note that the local error of $\boldsymbol{P}$ is not affected by the the local error of $\boldsymbol{U}$ or vice versa. Although the local error for displacement is reduced, it can be regarded as the flow operator (or the pure ODEs with the implicit function theorem) eventually controls the local and global errors for the whole system. However, if the geomechanics operator does not work

as contraint and the whole system is the pure ODEs as one, then the two-pass algorithm will enhance the local and the global order of accuracy. Due to the constraint as it is shown, therefore, the two-pass algorithm for the fixed-stress split, does not enhance the order from the fixed-stress split. This is consistent with the following interpretation as [34]: the two-pass algorithm (Equation 4.2) can be expressed as

$$\begin{aligned}\cdots \Phi_{h/2}) \circ \Xi_h \circ (\Phi_{h/2} \circ \Phi_{h/2}) \circ \Xi_h \circ (\Phi_{h/2} \circ \Phi_{h/2}) \circ \Xi_h \circ \Phi_{h/2} \\ = \cdots \underbrace{\Phi_h \circ \Xi_h \circ \Phi_h \circ \Xi_h \circ \Phi_h \circ \Xi_h}_{first-order\ in\ global} \circ \underbrace{\Phi_{h/2}}_{initialization},\end{aligned} \tag{4.33}$$

where the operator $\Phi_{h/2}$ at the first timestep takes a role for initialization, and the rest operators lead to the global first-order of accuracy as the two-pass algorithm advances in time. The result also can be interpreted as the order reduction that occurs for stiff ODEs and DAEs problems [47].

4.6 Error Analysis of the SDC Algorithm

The operator splitting using SDC for our study can be expressed as

$$\cdots \Phi_h \circ \Xi_h \circ \S_h \circ \Phi_h \circ \underbrace{\Xi_h \circ \S_h \circ \Phi_h}_{timestep1}, \tag{4.34}$$

where $\S_h$ is the correction operator for the flow operator Φ_h.

The order of accuracy of SDC depends on the the numerical approximation of the integral including $\int_{t_i}^{t_{i+1}} Lu(\tau, \tilde{u}(\tau))d\tau$ and it depends on the sub-nodes between t_i and t_{i+1}, through which we take the quadrature formula for the numerical integration (Equation 4.10). As for this study, we employ the second-order SDC method, thus only two quadrature points which are just the two points t_i and t_{i+1} for $t \in [t_n, t_{n+1}]$ are needed.

From the local error analysis of $\Xi_h \circ \S_h \circ \Phi_h$, because the approximate value of $\boldsymbol{P}(t_{n+1})$,

$\tilde{\boldsymbol{P}}_{n+1}$ by the operator Φ_h satisfies $\tilde{\boldsymbol{P}}_{n+1} = \boldsymbol{P}(t_{n+1}) + \Delta t f(\dot{\psi}(\boldsymbol{P}(t_n)), \boldsymbol{P}(t_n)) + O(\Delta t^2)$, we obtain

$$\tilde{\boldsymbol{P}}^{O}_{n+1} = \boldsymbol{P}(t_{n+1}) + O(\Delta t^2), \tag{4.35}$$

where the superscript O in $\tilde{\boldsymbol{P}}^{O}_{n+1}$ indicates the previous value before correction (i.e., predictor). Then using Equation 4.10,

$$\tilde{\boldsymbol{P}}^{N}_{n+1} = \boldsymbol{P}(t_n) + \frac{\Delta t}{2}[f(\dot{\psi}(\boldsymbol{P}(t_n)), \boldsymbol{P}(t_n)) + f(\dot{\psi}(\boldsymbol{P}(t_{n+1}) + O(\Delta t^2)), \boldsymbol{P}(t_{n+1}) + O(\Delta t^2))], \tag{4.36}$$

where the superscript N in $\tilde{\boldsymbol{P}}^{N}_{n+1}$ indicates the new value after correction (i.e., corrector). Note that the SDC for the second-order accuracy has the same form as the modified Euler method for ODEs with predictor and corrector. The modified Euler is known to be second-order for the order of accuracy in time [43].

Hence, the order of accuracy for the local error of $\Xi_h \circ \S_h \circ \Phi_h$ becomes $O(\Delta t^3)$ from Equation 4.24 and 4.27 where the $\boldsymbol{e}_{n+1}\Delta t^2$(see Equation 4.35) is corrected by the deferred correction[3], leading to

$$||\boldsymbol{P}(t_{n+1}) - \tilde{\boldsymbol{P}}^{N}_{n+1}|| = O(\Delta t^3), \tag{4.37}$$

where $||\cdot||$ is an appropriate norm.

Strictly, however, we must consider the approximation term for poromechanics. While not only fixing the displacement but also fixing the rate of stress or strain, we approximate

[3]Thus we can interpret that the classical DC or SDC eliminates the accumulation of the local errors, thus the order of accuracy for global error is the same as that of the local error if the scheme works.

$\dot{\psi}$ in flow by discretization with staggered method[4] as

$$\dot{\psi} \approx \tilde{\psi}_n = \frac{\boldsymbol{P}_n - \boldsymbol{P}_{n-1}}{\Delta t}, \tag{4.38}$$

fixing the rate of stress change ($\delta\dot{\sigma} = 0$) for the fixed-stress split. Considering the discretization error working as another factor inhibiting the accuracy enhancement, $\tilde{\psi} = \dot{\psi} + O(\Delta t)$, the local error for the SDC for the fixed-stress split using fractional step (operator splitting) is polluted and can only be estimated as

$$\boldsymbol{P}(t_{n+1}) + O(\Delta t^3) < \tilde{\boldsymbol{P}}_{n+1} \leq \boldsymbol{P}(t_{n+1}) + O(\Delta t^2), \tag{4.39}$$

and we obtain the first-order of accuracy for global error.

4.7 Numerical Experiments

For the numerical test, we perform the same Terzaghi's (1D) and the strip-footing plane strain (2D) consolidation problem as Chapter 1. In these cases as well, we take a fully-saturated isothermal single-phase fluid flow with drainage boundary at the top.

For the spatial discretization in 2D, we use a mixed formulation pair of Q1P0, which is a typical pair for reservoir simulation as mentioned in the previous chapter. The diplacement is approximated with piecewise linear interpolation using bilinear basis functions at the element node and the same conforming standard Galerkin's method. The pressure is approximated with piecewise constant interpolation at the center of element volume using FVM (Figure 4.1).

All the properties are the same as Chapter 1 as well. We apply a traction of 2.125 [MPa] at the top drainage boundary. No displacement is assumed against the normal direction to

[4]Since we use the staggered method without iteration, there is high error occuring especially at the early stage of simulation for a large timestep size. However, this splitting or sequential error decreases exponentially when smaller timestep sizes are taken [38].

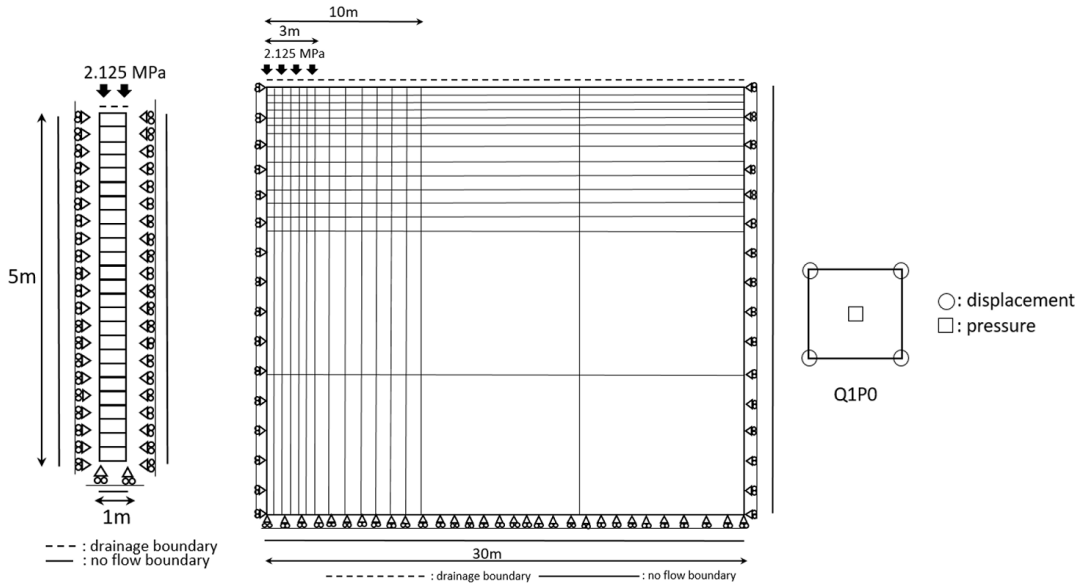

Figure 4.1: Domains of Terzaghi's problem (left), strip-footing plane strain problem (center), and the mixed formulation (Q1P0 pair) for spatial discretization (right).

all boundaries as well. In this study, we further assume isotropic homogeneous geomaterial with no gravitational effects and no stress dependence of flow properties. The rest input data for geomechanics and fluid flow parameters for both problems are shown in Table 4.1.

For the temporal discreization, we adopt the aforementioned backward Euler, a typical method in reservoir simulation. In order to calculate the global errors and the order of accuracy in time, we take numerical solutions by the monolithic method with a very tiny timestep size as two problems' reference solutions. Thus we can draw the effect of removing the errors that come from the spatial discretization and we can consider errors only from the temporal discretization. For this purpose, we take reference solutions of displacement and pressure values after total simulation time of 400 [s] with dt = 0.078125 [s] and the number of timesteps of 5120 for both problems. Then, we analze the erros from different solution strategies with 8 different timestep sizes and number of timesteps as shown in Table 4.2.

Table 4.1: Main input data

Property	Value	
Young's modulus	100	MPa
Poisson ratio	0	-
Biot's coefficient	1.0	-
porosity	0.3	-
permeability	50	mD
fluid density	1000	kg m^{-3}
fluid viscosity	1	cp
fluid compressibility	4.0×10^{-9}	Pa^{-1}

Table 4.2: Timestep size and number of timesteps for numerical tests

Timestep size (dt) [s]	Number of Timesteps
20	20
10	40
5	80
2.5	160
1.25	320
0.625	640
0.3125	1280
0.15625	2560

For the error analysis, we employ L2-norm to measure the errors, defined as follows:

$$||u(x)-U_h(x)||_{L^2} = \sqrt{\int_\Omega |u(x) - U_h(x)|^2 d\Omega} \approx \sqrt{\sum_{ele} \int_{x_{i-1}}^{x_i} |u(x) - U_h(x)|^2 dx}. \quad (4.40)$$

We first study the order of accuracy using both the monolithic and the fixed-stress split method. Then, we compare the two-pass algorithm and SDC for the fixed-stress split.

4.7.1 Order of accuracy for the monolithic and fixed-stress split methods

Figure 4.2 shows performance of convergence for the monolithic('MONO') and fixed-stress split('FSS') method for 1D (Figure 4.2a) and 2D (Figure 4.2b) problems, respectively. Since we employ the staggered method for the fixed-stress split, the absolute error itself is bigger than the monolithic. However, we identify that the errors decrease with the order of 1 for pressure and displacement, as the timestep size is refined and the number of timesteps increases. Therefore, the convergence rate in time follows the first-order in average, both for the monolithic and fixed-stress split method.

4.7.2 Order of accuracy for the two-pass and SDC methods

Figure 4.3 shows performance of convergence for the two-pass('2-Pass') and SDC methods for the same 1D (Figure 4.3a) and 2D (Figure 4.3b) problems, respectively. We find that both methods have the first-order of accuracy, being consistent with estimates from the mathematical analysis. Especially for displacement, we find the order of accuracy converges to that of pressure although the order of local error is not and is reduced by $\tilde{\boldsymbol{P}}_{n+1/2}$ for approximating $\boldsymbol{U}(t_{n+1})$ (Equation 4.32). And it can be found that the two-pass algorithm experiences order reduction into the first-order after the first two and three largest timestep sizes, especially for displacement, from the right of Figure 4.3a and from the right of Figure 4.3b, respectively. From the results, however, we cannot conclude that the two-pass algorithm or the SDC method is better than the other in terms of accuracy.

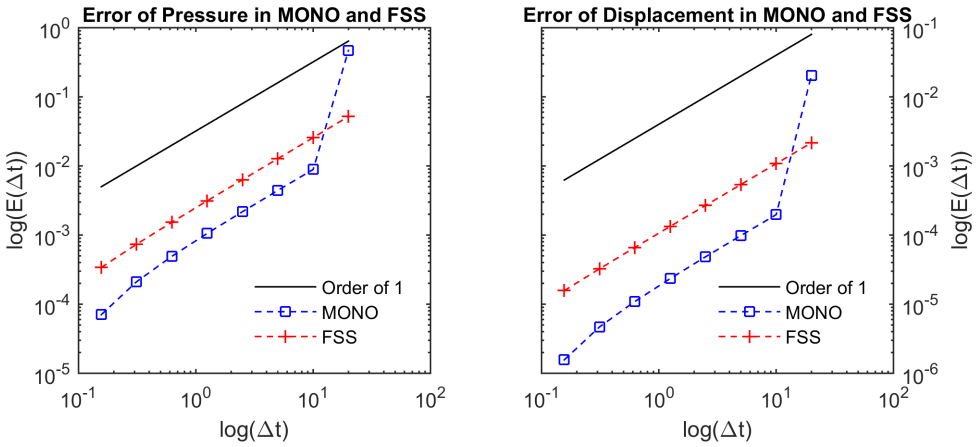

(a) Terzaghi's problem

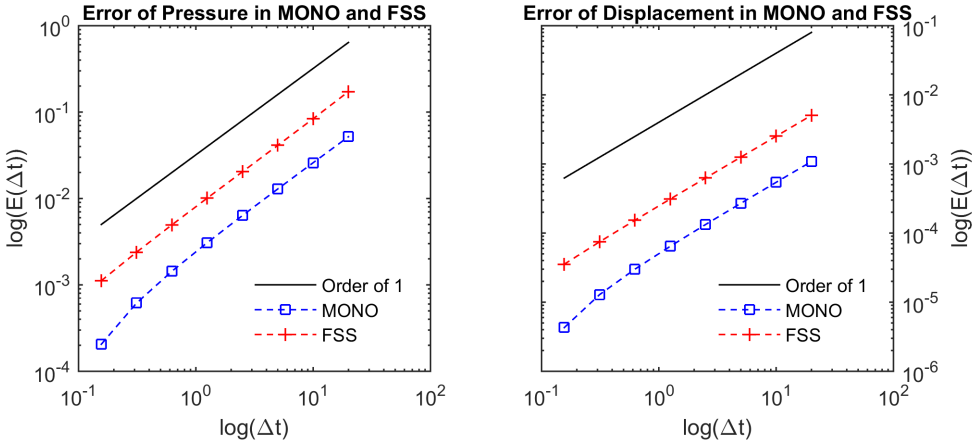

(b) strip-footing plane strain problem

Figure 4.2: The order of accuracy of the monolithic and fixed-stress split method for pressure (left) and for displacement (right).

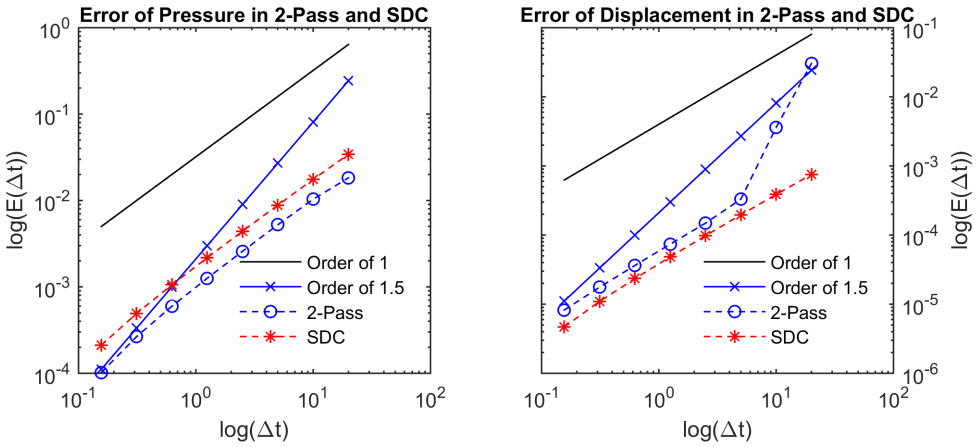

(a) Terzaghi's problem

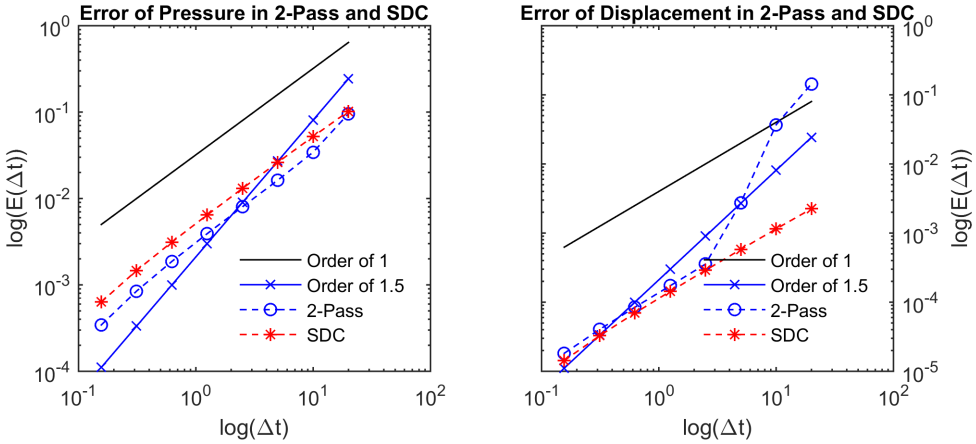

(b) strip-footing plane strain problem

Figure 4.3: The order of accuracy of the two-pass and SDC method for pressure (left) and for displacement (right).

4.8 Summary

In this chapter, we studied the possibility of high-order accuracy in time integration for poromechanics, by applying the fixed-stress split with the staggered fractional step (operator splitting scheme) to the two-pass and SDC methods. We found that both fixed-stress type two-pass and SDC methods reduce the absolute error values from the fixed-stress split. However, The two-pass method applied to the stiff ODEs does not provide high-order accuracy, causing the order reduction, because poromechanics problems result in the DAEs index-1 system. The SDC method can remove time discretization errors rapidly at the early times of simulation, because it stimulates convergence, correcting truncation errors. However, this method also does not improve the order of accuracy for poromechanics significantly. Because of the approximated total stress and its rate term in the flow equation, the order of accuracy stays the first-order even for the SDC method as well.

Thus, it is concluded that not only the operator itself can be a constraint to the whole system's accuracy, but also the numerical discretization itself can be another factor against the high-order method, which are both inherent structures for poromechanics. Considering that the computational cost for the two methods is higher than that of the original one-pass method, the one-pass fixed-stress split itself is sufficient for the reservoir simulation in poromechanics.

5. LARGE DEFORMATION SYSTEM

5.1 Introduction for Large Deformation System

Small deformation along with infinitesimal transformation is typically assumed in reservoir geomechanics simulation [78, 5, 4, 79]. This assumption is usually valid in reservoir engineering problems associated with rock, which include small deformation. However, the assumption might be invalid in largely deformable unconventional reservoirs, such as oceanic gas hydrate deposits and fractured/crashed salt domes [11, 80]. Furthermore, anisotropic reservoirs are profoundly sensitive to substantial changes in reservoir configuration, having full-tensor permeability and elastic moduli during deformation. This causes non-orthogonal grids in flow simulation. However, the modeling of largely deformable anisotropic reservoirs has little been investigated.

In this chapter,we employ the total Lagrangian method for coupled flow and geomechanics. Through the method, the coordinate system remained fixed both for flow and geomechanics. Instead, the deformation gradient reflects the change of reservoir configuration, which yields mathematical equivalence to the updated Lagrangian method [29, 81, 82]. The total Lagrangian method also induces full-tensor permeability from the Piola transformation, even if the initial permeability tensor is diagonal [83]. To accurately model full-tensor permeability, we use the multi-point flux approximation (MPFA) method [35]. Then, the total Lagrangian method with MPFA method can provide high accurate and rigorous modeling, honoring the objective stress rates (i.e., Lie derivatives) [84]. Thus, we consider the total Lagrangian method with MPFA method as the reference model in this study.

We first compare the reference model with the two-point flux approximation (TPFA) method, while the total Lagrangian method is still employed. TPFA method is typi-

cally used in reservoir simulation, but causes numerical errors for high anisotropic non-orthogonal grid systems [36], for example, near the stimulated or fractured wellbore area. Then, we also compare the reference model with an approach that updates the coordinate system each time step (without the total Lagrangian method) whereas employing small deformation assumption with TPFA method. This updated method, not the same with updated Lagrangian method, is intuitive, tracking the deformation of the grid system, but it might not honor the objectiveness of stress properly[1]. Additionally, numerical errors can be also caused by TPFA method. Thus, we will show numerical results and comparisons for these three numerical methods, taking various anisotropy ratios in initial permeability and elastic modulus for the numerical examples in this chapter.

5.2 Mathematical Formulations for Large Deformation System

We consider two configurations:

- the reference (or initial) configuration[2]
- the current (or deformed) configuration[3]

as shown in Figure 5.1.

To describe the motion of a body, we introduce the deformation gradient $\boldsymbol{F}$ as follows [82, 84, 85, 86, 87]:

$$\begin{aligned} \boldsymbol{F}(=F_{aA}) = \mathbf{GRAD}(\boldsymbol{x}) = \frac{\partial \boldsymbol{x}}{\partial \boldsymbol{X}}\Big(= \frac{\partial x_a}{\partial X_A}\Big) = \mathbf{1} + \frac{\partial \boldsymbol{u}}{\partial \boldsymbol{X}}, \\ \boldsymbol{x}(=\varphi(\boldsymbol{X}, t)) = \boldsymbol{X} + \boldsymbol{u}, \end{aligned} \tag{5.1}$$

where $\boldsymbol{X}$ and $\boldsymbol{x}$ are the coordinates of the reference and current configurations. **GRAD** is the gradient operator of the reference configuration, and $\boldsymbol{u}$ is the displacement from the

[1] See the detail in Appendix F.

[2] Also called as material coordinates or Lagrangian description.

[3] Also called as spatial coordinates or Eulerian description. At the initial time ($t = 0$), it is identical with the reference configuration.

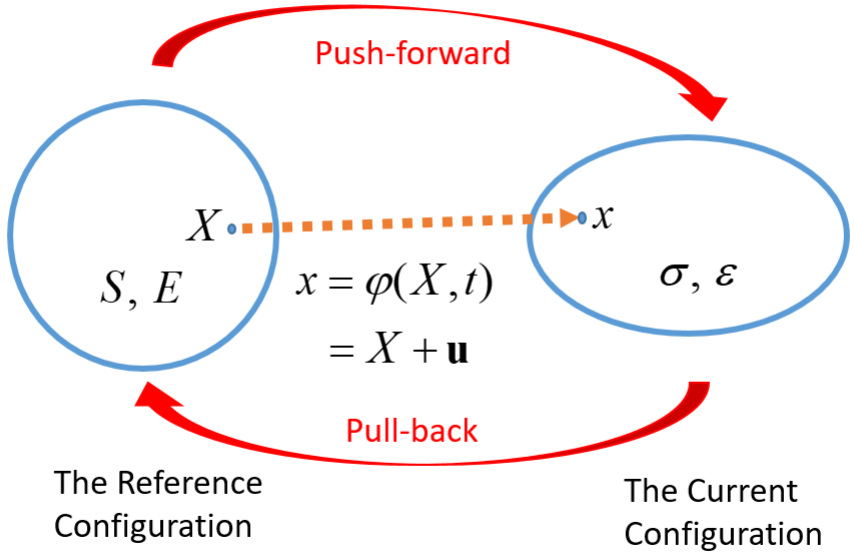

Figure 5.1: Mapping between the current and reference configurations (domains).

reference configuration. $\mathbf{1}$ is the rank-2 identity tensor. The Green-Lagrangian strain ($\boldsymbol{E}$) and right Cauchy-Green tensors ($\boldsymbol{C}$) are defined respectively as,

$$\boldsymbol{E} = \frac{1}{2}(\mathbf{GRAD}(\boldsymbol{u}) + \mathbf{GRAD}^T(\boldsymbol{u}) + \mathbf{GRAD}^T(\boldsymbol{u}) \cdot \mathbf{GRAD}(\boldsymbol{u})), \tag{5.2}$$

$$\boldsymbol{C} = \boldsymbol{F}^T\boldsymbol{F}, \tag{5.3}$$

The governing equations for geomechanics in the current and reference configurations are written respectively as,

$$\mathbf{div} \cdot \boldsymbol{\sigma}^{\boldsymbol{t}} + \rho_b^t \boldsymbol{g}^t = \mathbf{0}, \ \mathbf{DIV} \cdot \boldsymbol{P} + \rho_b^0 \boldsymbol{G}^0 = \mathbf{0}, \tag{5.4}$$

$$\boldsymbol{P} = J\boldsymbol{\sigma}\boldsymbol{F}^{-T}, \ J = \det(\boldsymbol{F}) = d\Omega^t/d\Omega^0, \tag{5.5}$$

where superscripts t and 0 indicate the current and reference configurations. $\boldsymbol{\sigma}$ is total Cauchy stress, $\boldsymbol{P}$ is the first Piola total stress, J is the Jacobian between the configurations ($J|_{t=0} = 1$). ρ_b is bulk density, $\boldsymbol{G}$ is the gravity vector, and **div** and **DIV** are the divergence operators in the current and reference configurations, respectively. Tensile stress is positive. Two equations of Equation 5.4 are related by mapping one equation to the other domain (i.e., push-forward and pull-back).

Two equations of Equation 5.4 can be transformed into the weak forms, respectively, written as,

$$\int_{\Omega^t} \boldsymbol{\sigma^t} : \boldsymbol{d}\, d\Omega^t = \int_{\Omega^t} \rho_b^t \boldsymbol{g}^t \cdot \dot{\boldsymbol{u}}\, d\Omega^t + \int_{\Gamma^t} \bar{\boldsymbol{t}}^t \cdot \dot{\boldsymbol{u}}\, d\Gamma^t, \tag{5.6}$$

$$\int_{\Omega^0} \boldsymbol{S} : \dot{\boldsymbol{E}}\, d\Omega^0 = \int_{\Omega^0} \rho_b^0 \boldsymbol{G}^0 \cdot \dot{\boldsymbol{u}}\, d\Omega^0 + \int_{\Gamma^0} \bar{\boldsymbol{t}}^0 \cdot \dot{\boldsymbol{u}}\, d\Gamma^0, \tag{5.7}$$

where $\boldsymbol{d}$ in Equation 5.6 is corresponding to the Cauchy infinitesimal strain (i.e., $\boldsymbol{d} = sym[\dot{\boldsymbol{F}}\boldsymbol{F}^{-1}]$, the spatial rate of deformation). $\bar{\boldsymbol{t}}^t$ is the traction vector on the boundary Γ of the domain Ω and $\boldsymbol{S}$ in Equation 5.7 is the second Piola total stress which can be expressed as $\boldsymbol{S} = J\boldsymbol{F}^{-1}\boldsymbol{\sigma}\boldsymbol{F}^{-T}$. See the conjugate pairs between the variables. The first term of Equation 5.6 can also be expressed showing the path-independent behavior (invariant) of the internal (virtual) work per unit mass as,

$$\int_{\Omega^t} \boldsymbol{\sigma^t} : \boldsymbol{d}\, d\Omega^t = \int_{\Omega^0} \boldsymbol{\tau} : \boldsymbol{d}\, d\Omega^0, \tag{5.8}$$

where $\boldsymbol{\tau}(= J\boldsymbol{\sigma^t})$ is the Kirchhoff total stress.

The governing equations of isothermal single flow in the current and reference configurations are written respectively in the integral forms as [83, 45],

$$\frac{d}{dt}\int_{\Omega^t} m_f\, d\Omega^t + \int_{\Omega^t} \mathbf{div} \cdot \boldsymbol{w}_f^t\, d\Omega^t + \int_{\Omega^t} q_f^t\, d\Omega^t = 0, \tag{5.9}$$

$$\frac{d}{dt}\int_{\Omega^0} M_f \, d\Omega^0 + \int_{\Omega^0} \mathbf{DIV} \cdot \boldsymbol{W}_f^0 \, d\Omega^0 + \int_{\Omega^0} Q_f^0 \, d\Omega^0 = 0, \tag{5.10}$$

where $m_f, q_f, \boldsymbol{w}_f^t$ are fluid mass, source, mass flux in the current configuration and M_f, Q_f, and $\boldsymbol{W}_f^0$ are corresponding variables in the reference configuration. $\boldsymbol{w}_f^t$, and $\boldsymbol{W}_f^0$ are related to pressure via the constitutive relation of Darcy's law, written as,

$$\boldsymbol{w}_f^t = \rho_f^t \boldsymbol{v}_f^t, \; \boldsymbol{v}_f^t = \frac{\boldsymbol{k}^t}{\mu_f} \cdot (\mathbf{grad}\, p_f - \rho_f^t \boldsymbol{g}^t), \tag{5.11}$$

$$\boldsymbol{W}_f^0 = \rho_f^0 \boldsymbol{V}_f^0, \; \boldsymbol{V}_f^0 = \frac{\boldsymbol{K}^0}{\mu_f} \cdot (\mathbf{GRAD}\, p_f - \rho_f^0 \boldsymbol{F}^T \boldsymbol{G}^0), \tag{5.12}$$

where p_f, ρ_f are fluid pressure and density. $\mathbf{grad}, \boldsymbol{k}^t, \boldsymbol{v}_f^t$ are gradient operator, intrinsic permeability tensor, volumetric flux in the current configuration and **GRAD** are gradient operator within the reference configuration and $\boldsymbol{K}^0, \boldsymbol{V}_f^0$ intrinsic permeability tensor, volumetric flux mapped on the reference configuration. Specifically,

$$\boldsymbol{K}^0 = J\boldsymbol{F}^{-1}\boldsymbol{k}^{\boldsymbol{t}}\boldsymbol{F}^{-T}, \tag{5.13}$$

where $\boldsymbol{k}^{\boldsymbol{t}}$ itself can depend on deformation requiring full-tensor permeability calculation. Following [83], the strong form of Equation 5.9 on $d\Omega^0$ is as,

$$\dot{M}_f + J\mathbf{div} \cdot \boldsymbol{w}_f^t + Jq_f = 0. \tag{5.14}$$

We describe coupling between single phase flow and geomechanics in a rate and spatial form, using poromechanics theory [83, 45] as,

$$L_v\boldsymbol{\tau} = L_v\boldsymbol{\tau}' - b_B\dot{p}_f\mathbf{1} \quad on \quad d\Omega^0, \; L_v\boldsymbol{\tau}' = \boldsymbol{c}^t : \boldsymbol{d}, \tag{5.15}$$

$$\begin{aligned} \frac{\dot{m}_f}{\rho_f^t} = b_B \dot{\varepsilon}_v + \frac{1}{M_B}\dot{p}_f \quad on \quad d\Omega^t,\ \dot{\varepsilon}_v = \boldsymbol{d} : \boldsymbol{1}, \\ \varepsilon = logJ,\ \frac{1}{M_B} = \phi c_f + \frac{b_B - \phi}{K_S}, \end{aligned} \tag{5.16}$$

where $\boldsymbol{\tau}'$ indicates the effective stress. b_B and M_B are the Biot coefficient and modulus. $\boldsymbol{c}^t$ is the spatial elasticity tensor. L_v is the Lie derivative for an objective stress rate, specifically written as,

$$L_v\boldsymbol{\tau} = \boldsymbol{F}\dot{\boldsymbol{S}}\boldsymbol{F}^T,\ L_v\boldsymbol{\tau}' = \boldsymbol{F}\dot{\boldsymbol{S}}'\boldsymbol{F}^T, \tag{5.17}$$

The above constitutive equations can also be rewritten in the reference configuration as,

$$\dot{\boldsymbol{S}} = \underbrace{\boldsymbol{C^0} : \dot{\boldsymbol{E}}}_{\dot{\boldsymbol{S}}'} - b_B \boldsymbol{B}_B \dot{p_f} \quad on \quad d\Omega^0, \tag{5.18}$$

$$\frac{\dot{M}_f}{\rho_f^0} = b_B \frac{\dot{J}}{J} + \frac{J}{M_B^0}\dot{p}_f \quad on \quad d\Omega^0,\ \frac{J}{M_B^0} = \frac{1}{M_B}, \tag{5.19}$$

where $\dot{M}_f d\Omega^0 = \dot{m}_f d\Omega^t$ and $\rho_f^0 d\Omega^0 = \rho_f^t d\Omega^t$. Then, the elasticity tensor in the reference configuration, $\boldsymbol{C}^0$, is related to $\boldsymbol{c}^t$ as [84],

$$c^t_{abcd}(= \boldsymbol{c}^t) = F_{aA}F_{bB}F_{cC}F_{dD}C^0_{ABCD},\ \boldsymbol{C}^0 = C^0_{ABCD}, \tag{5.20}$$

where $\boldsymbol{c}^t$ itself can depend on deformation as well.

5.3 Methodology: Numerical Discretizations for Large Deformation System

We employ the fixed-stress type sequential method proposed by Kim [88] for large defomation system. The proposed sequential method freezes the second Piola-Kirchhoff total stress field, $\boldsymbol{S}$, leading to one of the fixed-stress split in large deformation, which

yields

$$\frac{M_f^{n+1} - M_f^n}{\rho_f^0} = \Big(\frac{1}{M_B} + \frac{b_B^2}{K_{dr}}\Big)(p_f^{n+1} - p_f^n) - \frac{b_B^2}{K_{dr}}(p_f^n - p_f^{n-1}) + b_B(\varepsilon_v^{n+1} - \varepsilon_v^n),$$
$$K_{dr} = \alpha\frac{\mathbf{1} : \boldsymbol{c}^t : \mathbf{1}}{9}, \tag{5.21}$$

where α is an additional stabilization term for anisotropic elasticity (e.g.,transverse isotropy). By using the above discretized equation, we solve flow first, followed by geomechanics.

In space discretization, the FVM is used, whereas the FEM is used for geomechanics as a typical pair. There are two approaches in modeling full-tensor permeability: Two-point flux approximation (TPFA) and multi-point flux approximation (MPFA). For example, when the flux of fluid at an interface is calculated in two dimensions, TPFA uses two adjacent grid blocks, while MPFA uses six grid blocks [35], as shown in Figure 5.2.

To implement the total Lagrangian method for finite-strain geomechanics (large deformation), we refer to [82, 81].

5.4 Numerical Examples

We investigate coupled flow and geomechanics for anisotropic reservoirs such as fractured geological formations. Transverse isotropy can typically be employed for fractured/layered reservoirs. Then, for a set of horizontal fractures or layers, the spatial elasticity tensor under plane strain condition is given in an engineering notation as [89],

$$\begin{bmatrix} \sigma'_{xx} \\ \sigma'_{zz} \\ \sigma'_{zx} \end{bmatrix} = \frac{1}{H}\begin{bmatrix} \frac{1-\nu_{pz}\nu_{zp}}{E_pE_z} & \frac{\nu_{zp}+\nu_p\nu_{zp}}{E_pE_z} & 0 \\ \frac{\nu_{pz}+\nu_p\nu_{pz}}{E_p^2} & \frac{1-\nu_p^2}{E_p^2} & 0 \\ 0 & 0 & G_{zp} \end{bmatrix}\begin{bmatrix} d_{xx} \\ d_{zz} \\ 2d_{zx} \end{bmatrix},$$
$$H = \frac{(1+\nu_p)(1-\nu_p-2\nu_{pz}\nu_{zp})}{E_p^2E_z},\ \frac{\nu_{pz}}{E_p} = \frac{\nu_{zp}}{E_z}, \tag{5.22}$$

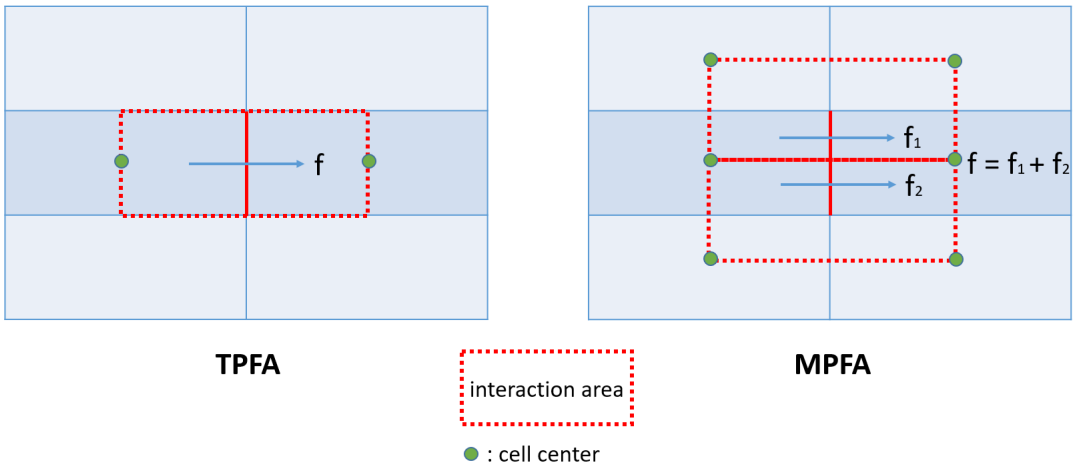

Figure 5.2: Schematics of calculation of transmissibility by using TPFA (left) and MPFA (right) for 2D regular grids.

where E_p and ν_p are Young's modulus and Poisson's ratio in the horizontal (x-)plane, respectively, while E_{pz} and ν_{pz} are those in the vertical (z-)direction. G_{zp} is shear modulus of the x-z plane.

Then, we test three methods for various anisotropic reservoirs:

1. Total Lagrangian method with MPFA: TL-MPFA,
2. Total Lagrangian method with TPFA: TL-TPFA,
3. Infinitesimal transformation with TPFA: IT-TPFA.

Since TL-MPFA is more accurate, it is the reference solution, because MPFA provides accurate solution, while TPFA can cause error due to non-orthogonality between permeability and the grid interface [35, 36]. Along with these three methods, we investigate two cases:

- deformation-independent spatial intrinsic Young's modulus (E) and permeability $(\boldsymbol{k}^t)$
- deformation-dependent spatial intrinsic Young's modulus (E) and permeability $(\boldsymbol{k}^t)$

We consider two cases for numerical experiments. Both domains take 27×27 grid blocks in x- and z-directions, respectively with non-uniform grid spacing, as shown in Figure 5.3 and Figure 5.4. The lengths of each domain in the x- and z-directions are both 100 [m]. We have a single layer in the y-direction, and its thickness is 1 [m] for both cases.

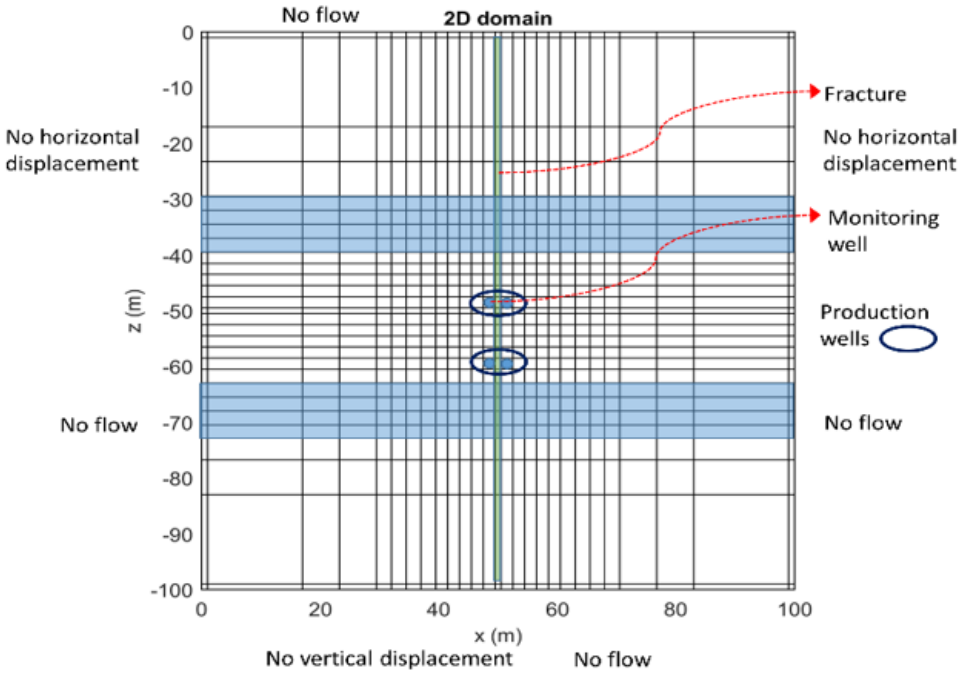

Figure 5.3: Domain of simulation with no stimulated zones (homogeneous): Case 1.

For Case 1 geomechanics, we consider two weak layers, having $E_{p2} = 50$ [MPa] from 29.5 [m] to 39.5 [m] and from 60.5 [m] to 70.5 [m] in the z-direction (section colored blue in Figure 5.3). The rest of areas have $E_{p1} = 900$ [MPa]. We take $\nu_p = 0.1, E_{pz} = 100$ [MPa], $\nu_{pz} = 0.01, G_{zp} = 45.5$ [MPa] (see Equation 5.22). The Biot's coefficient, $b_B = 1.0$. No gravity is considered for both flow and geomechanics.

For flow, the initial porosity is 0.3. The density, viscosity, and compressibility of fluid are 1000 $[kg/m^3]$, 10^{-3} [Pa.s], 4.4×10^{-10}[Pa^{-1}], respectively. For permeability, we consider center-line fracture in the z-direction only, which has width of 1 [m] and it has $k_{xx} = k_{zz} = 10$ [mD] (section colored green in Figure 5.3). The domain has 1 [m]-surrounding layers to employ no flow boundary condition (i.e., zero permeability). For the other areas, we use take the following permeability: $k_{xx} = 0.1$ [mD], $k_{zz} = 0.00001$ [mD], $k_{xz} = k_{zx} = 0$ [mD].

We have four production wells at the center area (oval-shaped blue line in Figure 5.3), where the rate is 0.5 $[kg/m^3/s]$ for each well, thus the total production rate for 4 wells is 2.0 $[kg/m^3/s]$. The production period is for 3.47 days. Initial pressure and total stress are both 10 [MPa], and overburden stress is 12 [MPa]. We have $\alpha = 0.2$ for stable coupled flow and geomechanics simulation.

We also consider another geological system: Case 2 (Figure 5.4). The difference between Case 1 and Case 2 lies in anisotropic permeability ratio and heterogeneity of permeability. For Case 2, we consider the stimulated zones between 29.5 [m] and 70.5 [m] in each direction. The zone is composed of two outer zones, which are from 29.5 [m] to 39.5 [m] and from 60.5 [m] to 70.5 [m] in the z-direction, respectively (section colored green in the middle square area in Figure 5.4). One inner zone is located between the two (section colored red in the middle square area in Figure 5.4). The two outer (green area) zones have $k_{xx} = 0.1$ [mD], $k_{zz} = 0.001$ [mD] and the inner zone has $k_{xx} = 0.1$ [mD], $k_{zz} = 0.01$ [mD]. Even for these zones, we have the same value for $k_{xz} = k_{zx} = 0$ [mD]

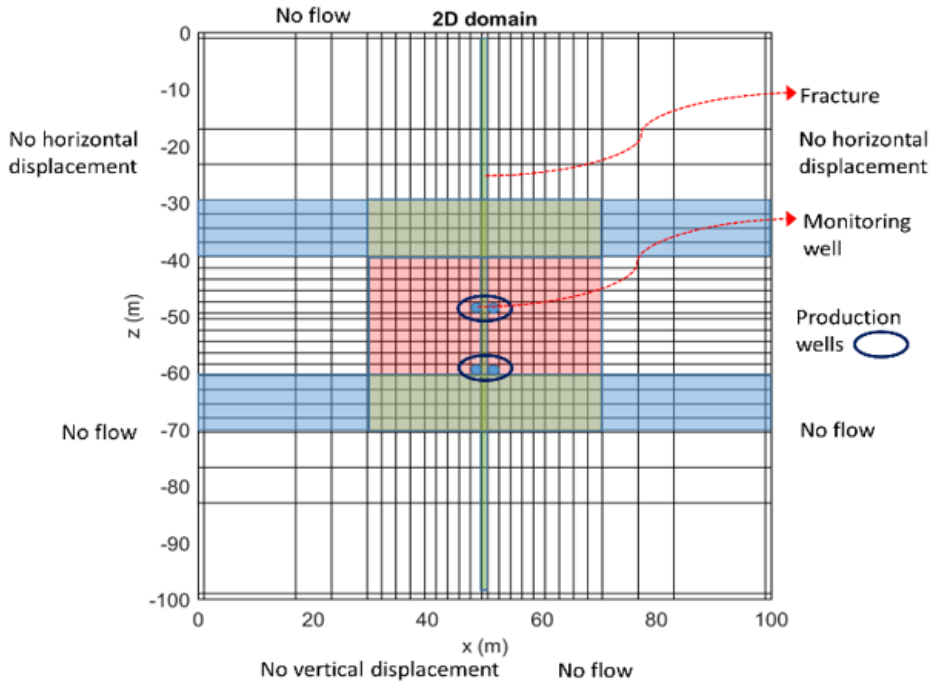

Figure 5.4: Domain of simulation with the stimulated zones (heterogeneous): Case 2.

as well. Thus, when we define the anisotropy ratio of permeability as $\lambda = k_{xx}/k_{zz}$, the outer stimulated zones have $\lambda = 100$ and the inner zone has $\lambda = 10$ in Figure 5.4. The rest areas of Case 2 have the same permeability as those of Case 1 with $\lambda = 10000$: $k_{xx} = 0.1$ [mD], $k_{zz} = 0.00001$ [mD], $k_{xz} = k_{zx} = 0$ [mD].

In other words, we have small anisotropy ratio for the stimulated zone in Case 2. We also consider the same fracture zone as $k_{xx} = k_{zz} = 10$ [mD] in the center.

5.4.1 Deformation-independent elasticity moduli and permeability

Figure 5.5 shows deformation of the reservoir for Case 1 by using TL-MPFA. Due to the center fracture which has higher permeability ($k_{xx} = k_{zz} = 10$ [mD]), the largest subsidence occurs along the center line of the domain. We also identify subsidence, which cannot validate the assumption of infinitesimal transformation (small deformation).

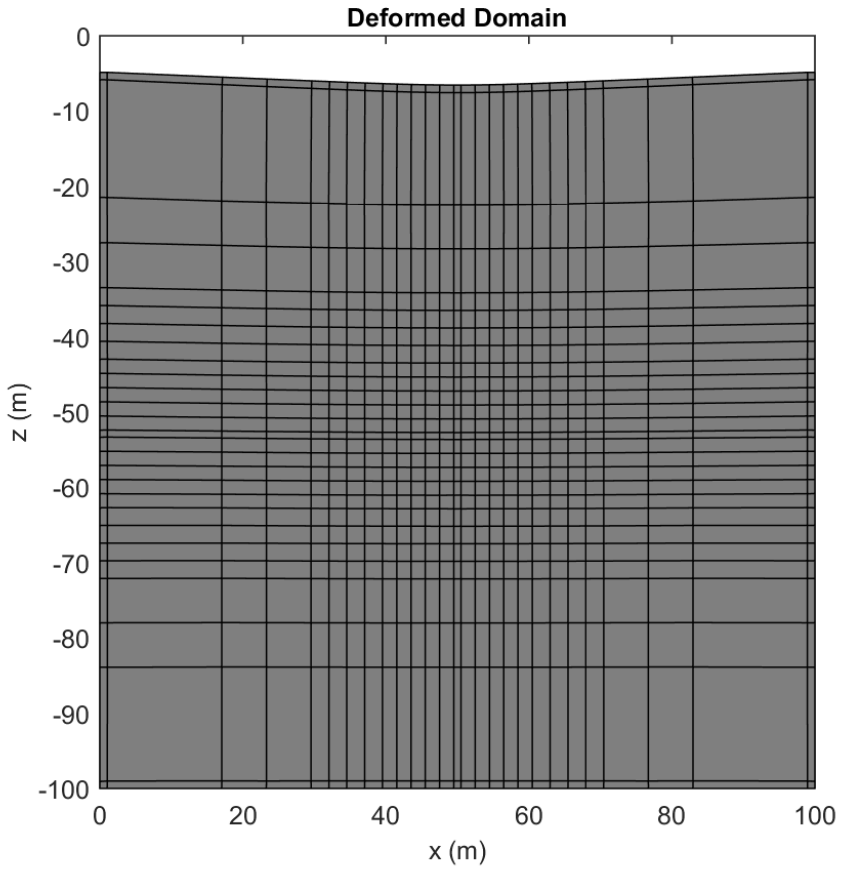

Figure 5.5: Deformation of the reservoir with TL-MPFA for Case 1.

From Figure 5.6, we find that IT-TPFA induces noticeable differences in displacements, compared to TL-TPFA and TL-MPFA, because the assumption of infinitesimal transformation is no longer valid.

In Figure 5.7, we also identify some errors in spatial distributions of volumetric strain and pressure between TL-MPFA and TL-TPFA. Specifically, the maximum difference in volumetric strain is over 0.01 (1 %), and the maximum relative difference in pressure is around 0.14 (14 %). Those errors are considerable and cannot be ignored. The errors occur mainly in the upper left and right sides, where large shear deformation occurs. This

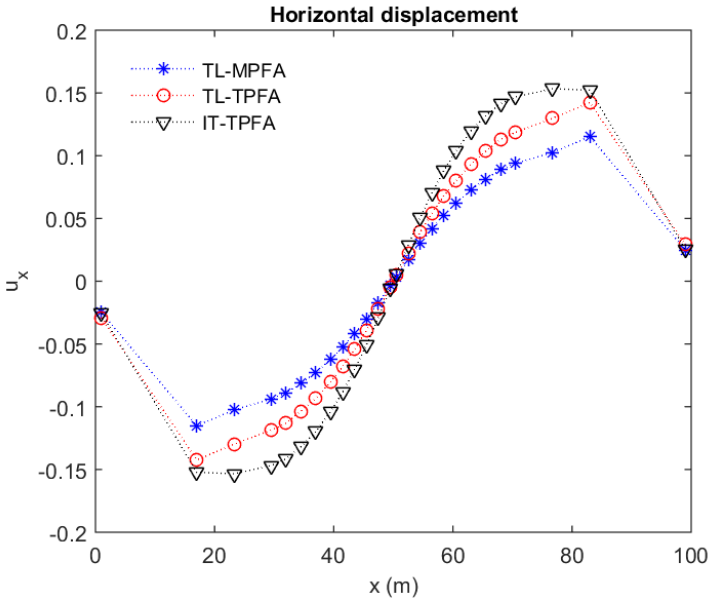

(a) Displacements in x-direction

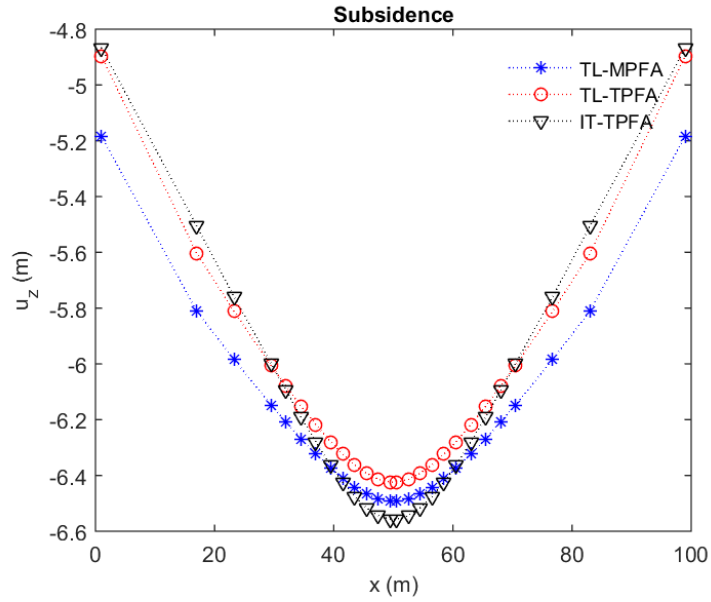

(b) Displacements in z-direction

Figure 5.6: Displacements of x (a) and z (b) directions at the top for Case 1.

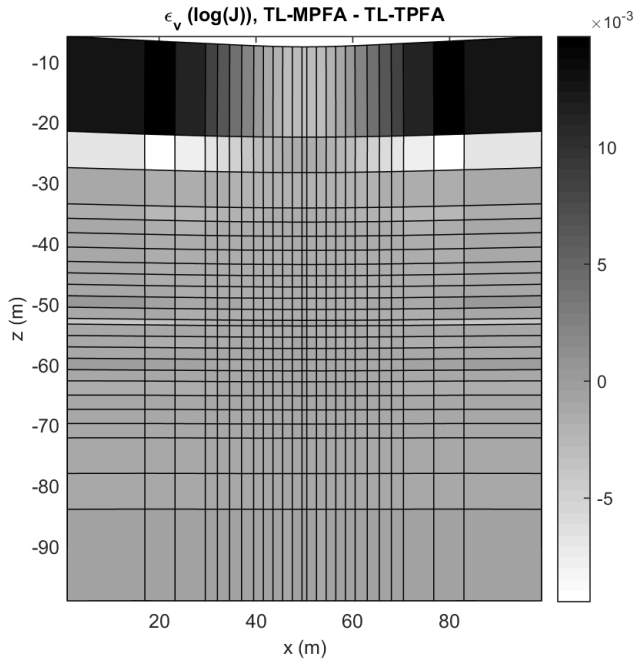

(a)

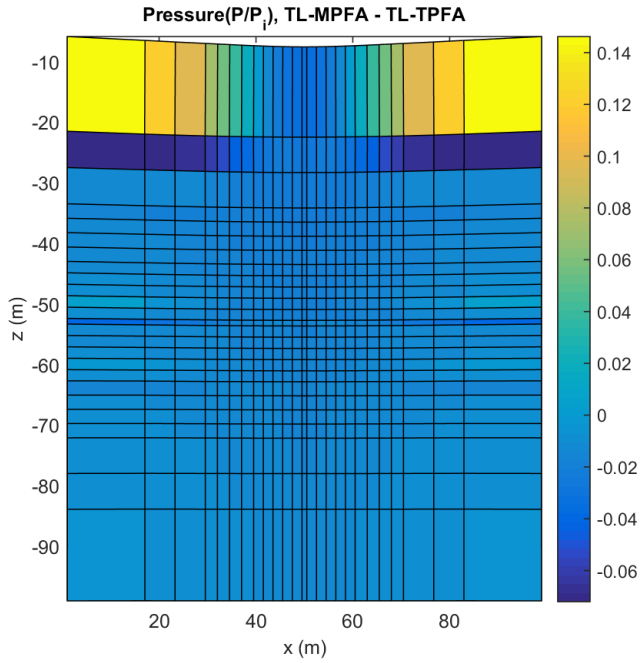

(b)

Figure 5.7: Comparison between MPFA and TPFA in deformation-independent elasticity moduli and permeability for Case 1 (large λ): volumetric strain (top) and pressure (bottom).

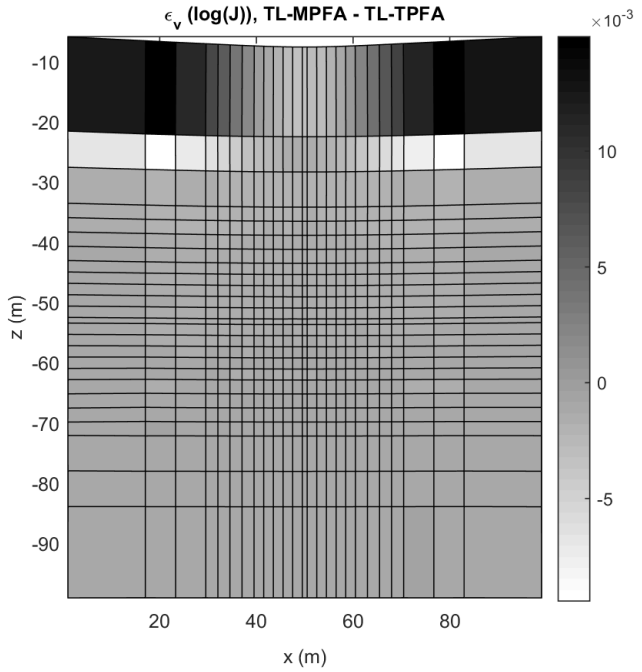

(a)

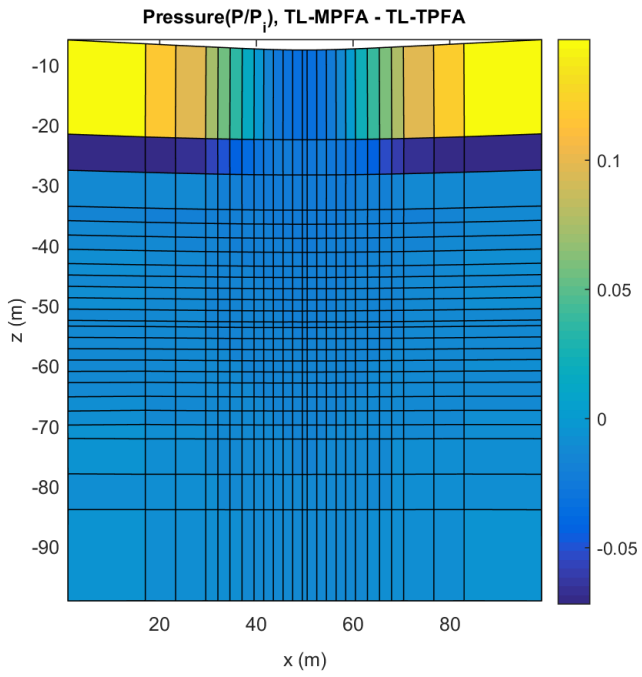

(b)

Figure 5.8: Comparison between MPFA and TPFA in deformation-independent elasticity moduli and permeability for Case 2 (small λ): volumetric strain (top) and pressure (bottom).

large shear deformation changes configuration of the domain, yielding full-tensor $\boldsymbol{K}^0$.

For Case 2, we observe less errors between TL-MPFA and TL-TPFA, compared to Case 1, because small anisotropic ratio in x-direction and z-direction is assigned in the stimulated zone (green and red colored section at the center square in Figure 5.4). Still, the maximum relative error in pressure is beyond 0.1 (10 %) (see Figure 5.8), which is significant. As the anisotropic ratio increases, permeability becomes more sensitive to deformation.

5.4.2 Deformation-dependent elasticity moduli and permeability

The intrinsic elasticity tensor and permeability can depend on deformations, such as rotation. Thus, we use rotation-dependent elasticity and permeability in this section. We take polar decomposition following [84].

$$\boldsymbol{F} = \boldsymbol{R}\boldsymbol{U}, \tag{5.23}$$

where $\boldsymbol{R}$ is the rotational tensor and $\boldsymbol{U}$ is the right stretch tensor. When $\boldsymbol{c}^t$ is rotation-dependent, written as

$$c^t_{abcd}(=\boldsymbol{c}^t) = R_{am}R_{bn}R_{cp}R_{dq}c^{t,ini}_{mnpq}, \tag{5.24}$$

where $c^{t,ini}_{mnpq}$ is the initial intrinsic spatial elasticity tensor. Then, we have

$$c^t_{abcd}(=\boldsymbol{c}^t) = U_{aA}U_{bB}U_{cC}U_{dD}C^0_{ABCD}. \tag{5.25}$$

Similarly, when permeability, $\boldsymbol{k}^t$, is rotation-dependent, written as

$$\boldsymbol{k}^t = \boldsymbol{R}\boldsymbol{k}^{t,ini}\boldsymbol{R}^T, \tag{5.26}$$

where $\boldsymbol{k}^{t,ini}$ is the initial intrinsic permeability, then we obtain

$$\boldsymbol{K}^0 = J\boldsymbol{U}^{-1}\boldsymbol{k}^{t,ini}\boldsymbol{U}^{-T}. \tag{5.27}$$

Figure 5.9 and 5.10 show differences between TL-MPFA and TL-TPFA for Cases 1 and 2, respectively, which are both noticeable.

From the results of Cases 1 and 2, as the anisotropy increases, the differences in volumetric strain and pressure between the two methods become larger, but they are less than those from the deformation-independent case.

For the case of the rotation-dependent elasticity and permeability, we find smaller differences between TL-MPFA and TL-TPFA compared the rotation-independent elasticity and permeability in their absolute values. For example, the maximum error in volumetric strain is 0.004 (0.4 %) and the maximum relative error in pressure is around 0.04 (4 %). However, the errors have pattern that is distributed over the domain especially around the center where more rotation may occur (as showed in Figure 5.5) with relatively high heterogeneity of permeability and flow is occuring actively due to stimulation, thus still those errors cannot be neglected.

Especially for Case 2, between the rotation-independent and rotation-dependent cases, the errors are slightly scattered in the rotation-dependent case, although the absolute value itself decreases (Figure 5.10).

5.5 Summary

Through this chapter, we proposed and investigated numerical methods of largely deformable anisotropic reservoirs in the context of two-way coupled flow and geomechanics. We compared the three methodologies to solve problems for the large deformation system sensitive to anisotropic properties: the total Lagrangian method with MPFA, the total Lagrangian method with TPFA, and the method based on infinitesimal transformation with

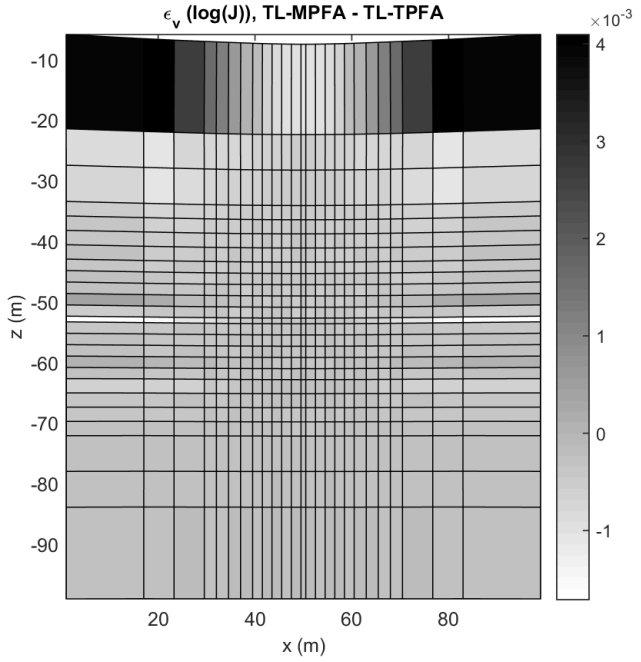

(a)

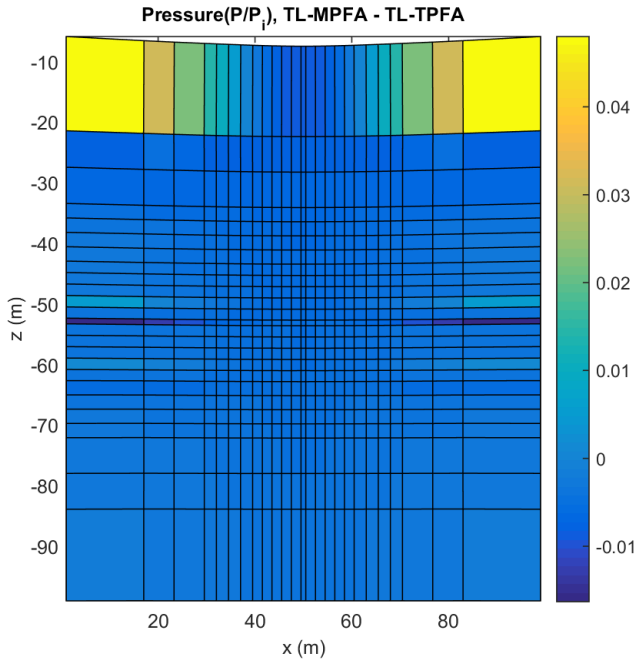

(b)

Figure 5.9: Comparison between MPFA and TPFA in deformation-dependent elasticity moduli and permeability for Case 1 (large λ): volumetric strain (top) and pressure (bottom).

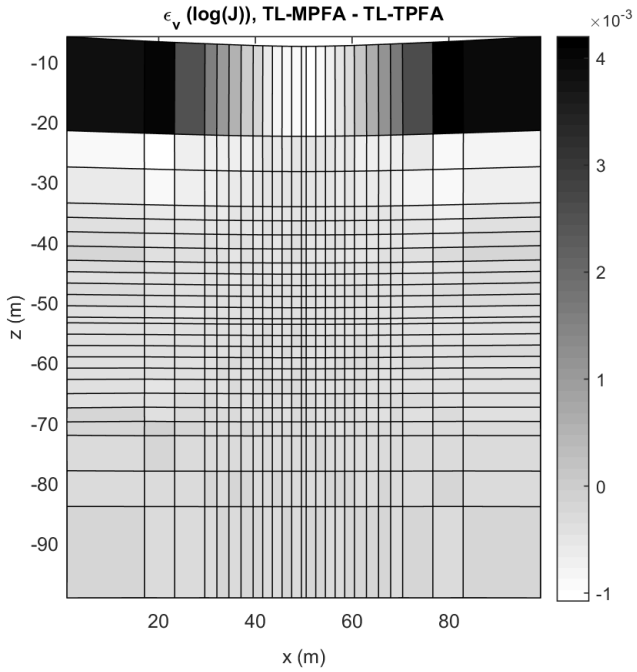

(a)

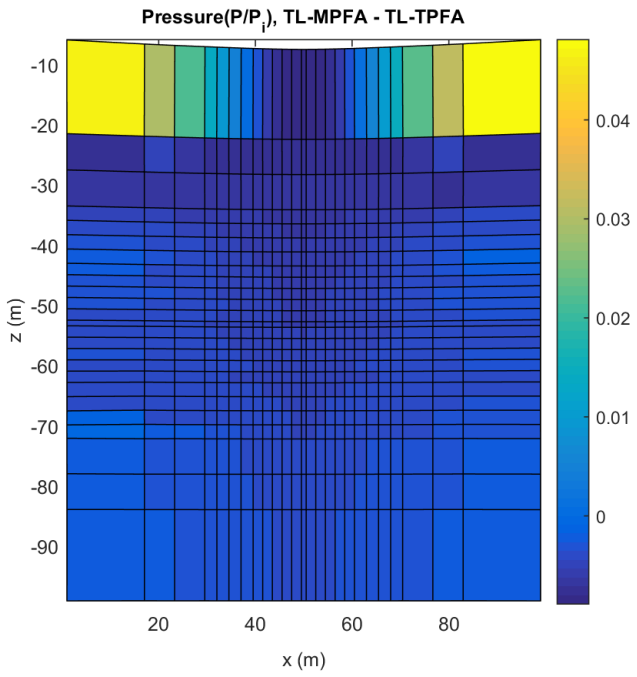

(b)

Figure 5.10: Comparison between MPFA and TPFA in deformation-dependent elasticity moduli and permeability for Case 2 (small λ): volumetric strain (top) and pressure (bottom).

TPFA. From numerical tests, we found there were considerable differences between the total Lagrangian method and the method of the infinitesimal transformation. We also identified noticeable differences between the MPFA and the TPFA. Although more complicated or realistic scenarios for large deformation need to be investigated in the future, and we tested only limited cases for the study, we found out that severe mesh deformation with considerable configuration changes or non-linear elastic behavior can be highly sensitive to the anisotropic properties of geomechanics and fluid flow. It can be said that for more accuracy in the anisotropic large deformation system for poromechanics, appropriate mixed formulations, such as the total Lagrangian with the MPFA methods, are needed in seeking more accurate solutions close to the true or real physics.

6. APPLICATION WITH LARGE SCALE SIMULATION

In this chapter, as an application, large scale numerical simulations for a real field and their results are addressed. The objective is to estimate the in-situ stress distribution by honoring the well data over the domain.

The usual unconstrained mechanics have no delimitation existing in the scope of solution or in the degree of freedom as long as the solution vector satisfies the prime equation, the momentum balance. For this chapter, constraints are added to the unconstrained mechanics with measured stress data at well locations. As we consider the linear case without any non-linearity, this constrained mechanics belongs to the linear constraint problem.

Through the study, we find that this is mathematically the same type of problem as the saddle point problem aforementioned in the study, and in order to overcome the constraint and obtain the feasible and accurate solution, we employ the Uzawa's algorithm (Equation 3.19 and 3.20).

6.1 Considerations for the Simulation

6.1.1 Assumptions

In order to estimate the in-situ stress distribution in the TAMU field depth near 6000 m, there are several assumptions that need to be set up for the numerical simulation. The assumptions are the followings:

- No interaction with fluid exists.
- The pressure is constant over the domain as a single value for the initial state.
- No explicit faults (geometry, properties) are considered.
- Constant geomechanical parameters are considered: linear elastic problem.

- The reservoir is perfectly horizontal and its thickness is constant having the same overburden stress for the top layer.

6.1.2 Numerical conditions and input data

The target domain for the simuation is only PETE formation in the TAMU field[1]. The domain is discretized with over 1 M cells, thus the super computing system within Texas A&M High Performance Research Computing (TAMU HPRC) center is utilized. The concrete figures for the domain and its discretization are as Table 6.1 below. Since we only consider the reservoir formation, PETE, the simulation domain is rotated 36.9° toward the north, the direction with y-axis in green arrow, along with z-axis, the direction with blue arrow in Figure 6.1, respectively.

Table 6.1: Discretization figures for the simulation targeting PETE.

Parameters	Value	Unit
Length(Δx)	28,957.5	m
Width(Δy)	23,400.0	m
Thickness(Δz)	500.0	m
Number of gridblocks in x	405	-
Number of gridblocks in y	312	-
Number of gridblocks in z	8	-
Number of gridblocks in total	1,010,880($= 405 \times 312 \times 8$)	-
dx	71.5	m
dy	75.0	m
dz	62.5	m

The average values such as principal stresses, fluid pressure and other geomechanical parameters for the PETE are shown in Table 6.2. The average maximum horizontal stress direction is along the y-axis direction in Figure 6.1. We adopt the Young's modulus and

[1]The original field data are restricted to publish. Thus we name it as PETE for the reservoir and as TAMU for the field.

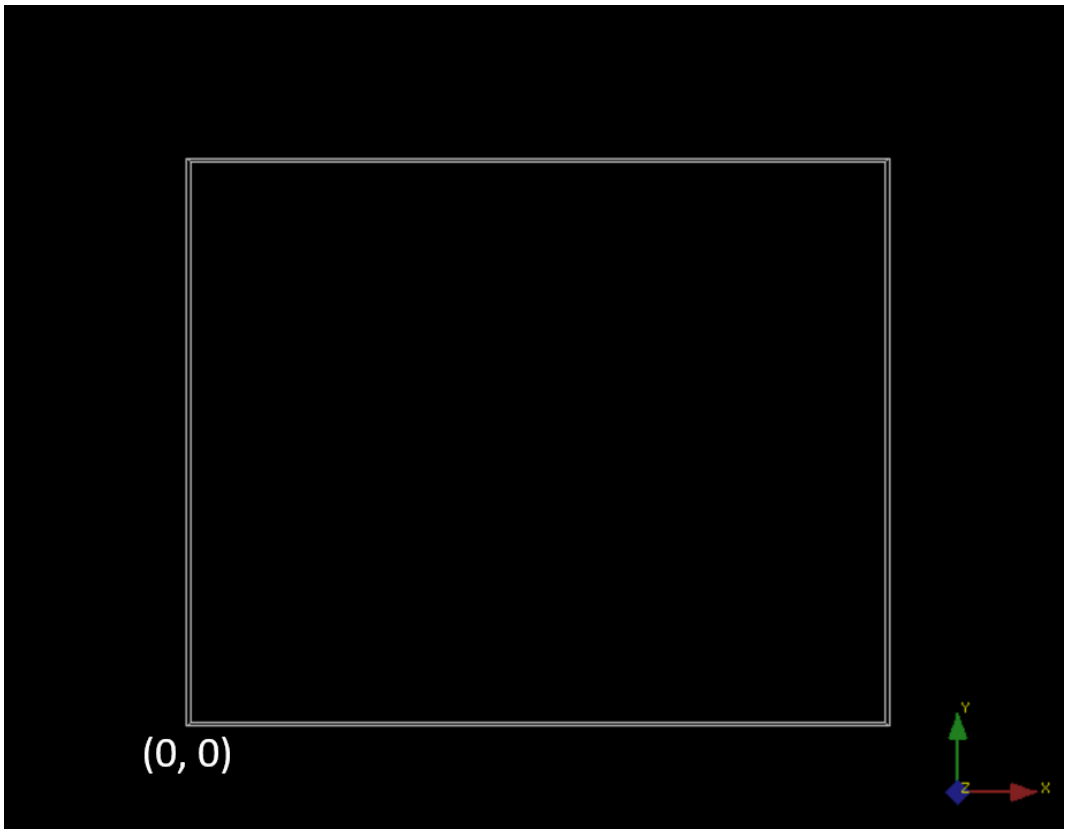

Figure 6.1: The top view of PETE reservoir domain in TAMU field (36.9°rotated in azimuth): the lower left corner has coordinates of $(0, 0)$ for its x- and y-directions.

Poisson's ratio value as representative and use them for all cells over the domain (homogeneous). Since we don't consider any change in geomechanical parameters being initial conditions over time, the simulation is a typical linear problem.

Boundary conditions for the geomechanics is no displacement boundary (Dirichlet boundary) toward each layer's normal direction except the top layer where the traction boundary (Neumann boundary) is given, and boundary conditions for flow is no flow boundary all over the domain.

Table 6.2: Average properties for the simulation.

Parameters	Value	Unit
σ_{Hmax}	131.0	MPa
σ_{hmin}	110.0	MPa
σ_V	148.0	MPa
Overburden stress (traction)	144.0	MPa
Fluid pressure (p)	72.5	MPa
Young's modulus (E)	25.0	GPa
Poisson's ratio (ν)	0.25	-
Bulk density (ρ_b)	2,600	kg/m^3
Biot's coefficient	1.0	-

6.1.3 Well data

Total 11 wells are located in the PETE formation (Table 6.3) and their locations are indicated in the Figure 6.2.

Table 6.3: Well data for the simulation.

Well Number	Name	Locations in (x, y)	Type
1	Well 1	(25838.6, 9003.1)	full data
2	Well 2	(28064.1, 9491.2)	full data
3	Well 3	(9728.4, 11694.6)	full data
4	Well 4	(28607.5, 2808.8)	full data
5	Well 5	(22981.6, 10517.8)	full data
6	Well 6	(20640.0, 7663.4)	full data
7	Well 7	(7885.6, 8333.4)	full data
8	Partial Well 1	(13130.7, 21820.2)	partial data
9	Partial Well 2	(6863.3, 18481.0)	partial data
10	Partial Well 3	(10164.1, 18038.3)	partial data
11	Zero Well	(15627.1, 12708.9)	no data

The type in the last column for (Table 6.3) is indicating data existence of each well such that 'full data' type means a well has both principal stresses data and average maxi-

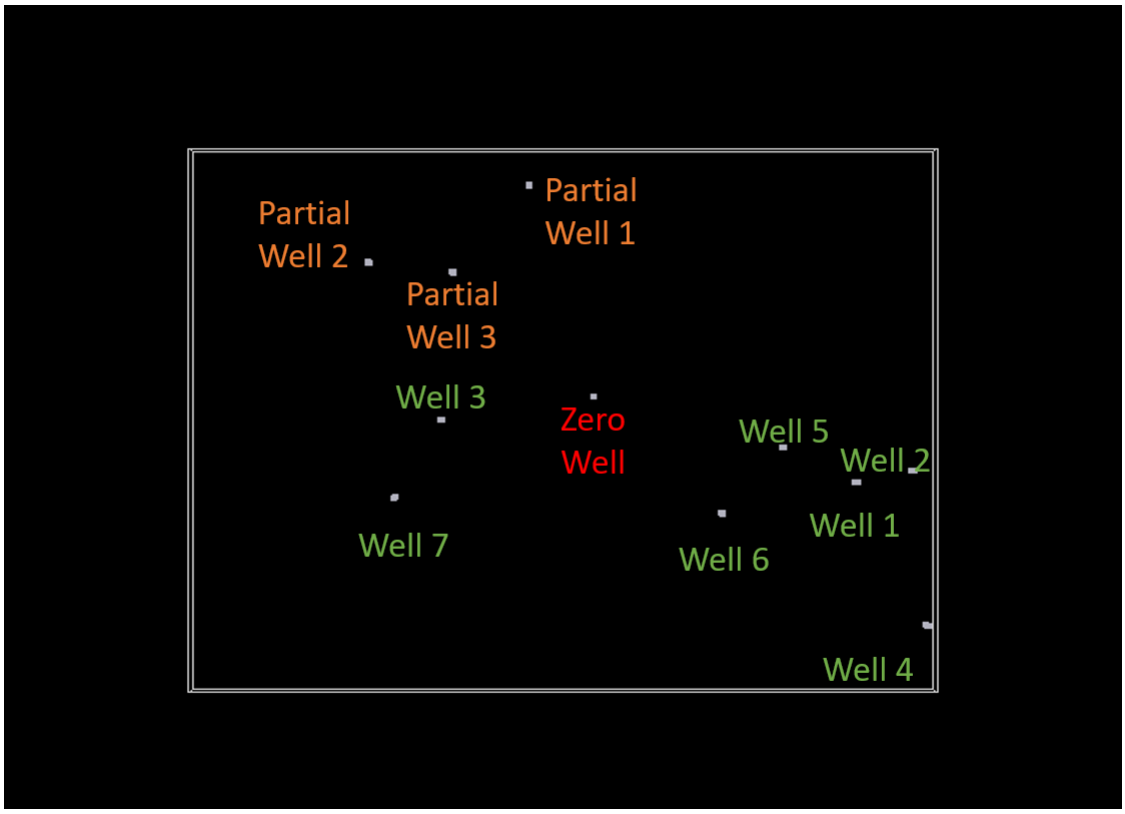

Figure 6.2: Wells in PETE: green wells have full data, yellow wells have partial data without maximum stress direction and no data for the red well.

mum stress direction but 'partial data' type means a well has no average maximum stress direction values but principal stresses. They are figured with colors in Figure 6.2: green, yellow and red. For example, the Zero Well, which is in red has no data at all. The first 7 wells are to be the constraints for the constrained mechanics where further case study is discussed.

Each grid block that belongs to each well location has a single value for each principal stress which are volume averaged from the raw data. Since the domain of PETE for the simulation has been rotated, the maximum stress direction of each well must take into account the rotation angle, 36.9°, and we consider the 6 components of stress data or geographic coordinate system stresses from principal stresses, applying the tensor rotation

(transformation) formula (Equation 6.1, [5]).

$$\boldsymbol{S_g} = \boldsymbol{R_s^T S_s R_s}, \tag{6.1}$$

where $\boldsymbol{S_s}$ is principal stresses and $\boldsymbol{S_g}$ is stresses in geographic coordinate system. And

$$\boldsymbol{R_s} = \begin{bmatrix} \cos\beta\cos\gamma + \sin\alpha\sin\beta\sin\gamma & -\cos\alpha\sin\gamma & -\sin\beta\cos\gamma + \sin\alpha\cos\beta\sin\gamma \\ \cos\beta\sin\gamma - \sin\alpha\sin\beta\cos\gamma & \cos\alpha\cos\gamma & -\sin\beta\sin\gamma - \sin\alpha\cos\beta\cos\gamma \\ \cos\alpha\sin\beta & \sin\alpha & \cos\alpha\cos\beta \end{bmatrix},$$

where α, β, and γ is rotation angle along the x-, y-, z-axis respectively.

6.2 Case Study

We deal with a total of 4 case studies for the simulation. Figure 6.3 is showing the frame chart for methodology for 4 cases. There are the two different strategies: one is about the heterogeneity and the other one is about the constraint. We start with the base case, Case 0, where initial input stress is homogeneous and no well data is constrained.

For homogeneous stress distribution cases (Case 0 and Case 1) the following averaged gradient values are used for principal stresses and fluid pressure (Table 6.4). Table 6.2 in the previous section has the same values in MPa at 6250 m with the gradient values in Table 6.4 which are the input for Case 0 and Case 1 (Figure 6.3).

Table 6.4: Gradient values for homogeneous stress input.

Parameters	Gradient Value	Unit
σ_{Hmax}	2.10	g/cc
σ_{hmin}	1.75	g/cc
σ_V	2.40	g/cc
Fluid pressure (p)	1.16	g/cc

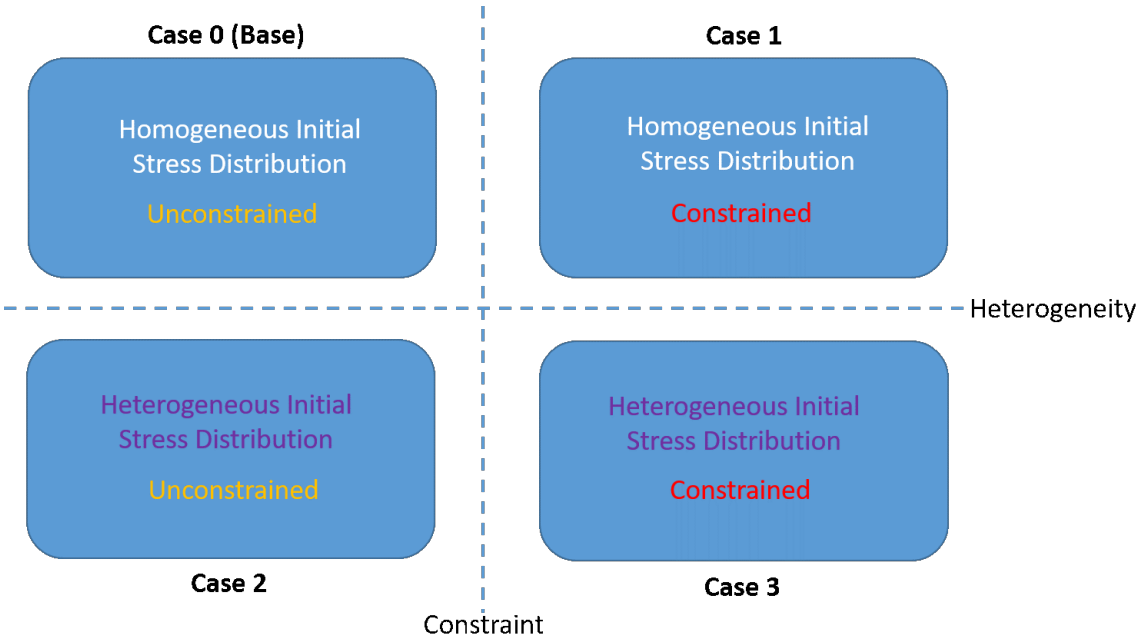

Figure 6.3: Case study chart.

Case 1 and Case 3 are the constrained mechanics against the unconstrained mechanics. In these cases, efforts have been made to honor the well data (see Table 6.5) which are volume averaged from the measured real data over the well locations. In order to overcome the saddle point problem, we use the Uzawa's iteration method mentioned earlier.

For heterogeneous stress distribution cases, we have Case 2 and Case 3 for heterogeneous stress distribution as initial input data where we use ordinary Kriging method, and for that purpose we generate the data using an open source software for geostatistics, SGeMS (Stanford Geostatistical Modeling Software), based on the same well data in Table 6.5. From Case 0 through Case 3, other geomechanical parameters such as Young's modulus and Poisson's ratio including fluid pressure are the same for all cases as Table 6.2 which are constant variables following the assumptions previously stated.

Table 6.5: Seven constrained well data: volume-averaged $\sigma_{Hmax}, \sigma_{hmin}, \sigma_V$ in [MPa] and constant mean azimuth degree of σ_{Hmax}

Well 1

Depth $[m]$	$\sigma_{Hmax}\,[MPa]$	$\sigma_{hmin}\,[MPa]$	$\sigma_V\,[MPa]$	Mean azimuth of σ_{Hmax}
6031.25	121.11	100.09	144.75	248.2
6093.75	124.19	102.95	146.78	248.2
6156.25	127.35	105.96	148.37	248.2
6218.75	128.98	107.36	149.87	248.2
6281.25	129.50	107.65	151.64	248.2
6343.75	130.16	108.06	153.52	248.2
6406.25	128.86	106.45	155.03	248.2
6468.75	129.89	107.25	156.54	248.2

Well 2

Depth $[m]$	$\sigma_{Hmax}\,[MPa]$	$\sigma_{hmin}\,[MPa]$	$\sigma_V\,[MPa]$	Mean azimuth of σ_{Hmax}
6031.25	120.58	99.57	144.75	183.1
6093.75	122.68	101.41	146.58	183.1
6156.25	124.40	102.91	148.37	183.1
6218.75	126.00	104.67	149.87	183.1
6281.25	127.31	105.37	151.38	183.1
6343.75	128.33	106.18	152.88	183.1
6406.25	129.55	107.17	154.39	183.1
6468.75	130.64	108.05	156.04	183.1

Well 3

Depth $[m]$	$\sigma_{Hmax}\,[MPa]$	$\sigma_{hmin}\,[MPa]$	$\sigma_V\,[MPa]$	Mean azimuth of σ_{Hmax}
6031.25	128.22	107.98	144.75	185.3
6093.75	126.55	105.52	146.42	185.3
6156.25	126.56	105.26	148.37	185.3
6218.75	128.99	107.50	149.87	185.3
6281.25	130.69	109.00	151.38	185.3
6343.75	133.10	111.23	152.88	185.3
6406.25	133.04	110.87	154.92	185.3
6468.75	131.79	109.33	156.54	185.3

Table 6.5: Continued

Well 4

Depth $[m]$	$\sigma_{Hmax}\,[MPa]$	$\sigma_{hmin}\,[MPa]$	$\sigma_V\,[MPa]$	Mean azimuth of σ_{Hmax}
6031.25	122.19	101.12	144.75	246.2
6093.75	124.80	103.57	146.61	246.2
6156.25	126.19	104.72	148.37	246.2
6218.75	126.29	104.59	149.87	246.2
6281.25	129.16	107.25	151.38	246.2
6343.75	129.50	107.37	152.88	246.2
6406.25	132.07	109.73	154.95	246.2
6468.75	133.82	111.31	156.54	246.2

Well 5

Depth $[m]$	$\sigma_{Hmax}\,[MPa]$	$\sigma_{hmin}\,[MPa]$	$\sigma_V\,[MPa]$	Mean azimuth of σ_{Hmax}
6031.25	121.20	100.18	144.75	250.3
6093.75	123.43	102.21	146.25	250.3
6156.25	124.79	103.34	147.83	250.3
6218.75	128.12	106.52	149.87	250.3
6281.25	129.05	107.24	151.38	250.3
6343.75	126.81	104.78	152.88	250.3
6406.25	131.41	109.14	154.39	250.3
6468.75	132.09	109.55	155.90	250.3

Well 6

Depth $[m]$	$\sigma_{Hmax}\,[MPa]$	$\sigma_{hmin}\,[MPa]$	$\sigma_V\,[MPa]$	Mean azimuth of σ_{Hmax}
6031.25	121.05	100.10	144.75	211.7
6093.75	122.77	101.61	146.34	211.7
6156.25	125.98	104.59	148.37	211.7
6218.75	126.97	105.31	149.87	211.7
6281.25	129.61	107.79	151.38	211.7
6343.75	130.97	109.01	152.88	211.7
6406.25	131.86	109.60	154.39	211.7
6468.75	136.02	113.82	155.90	211.7

Table 6.5: Continued

Well 7

Depth $[m]$	$\sigma_{Hmax}\,[MPa]$	$\sigma_{hmin}\,[MPa]$	$\sigma_V\,[MPa]$	Mean azimuth of σ_{Hmax}
6031.25	122.59	101.60	145.01	350.0
6093.75	124.63	103.41	146.86	350.0
6156.25	125.97	104.50	148.37	350.0
6218.75	127.95	106.25	149.87	350.0
6281.25	129.69	107.77	151.38	350.0
6343.75	130.90	108.72	152.88	350.0
6406.25	132.69	110.29	154.39	350.0
6468.75	132.92	110.25	155.90	350.0

6.3 Results and Discussion

In the section, we put some results for the case study. For visualization purpose only, we plot each result at the domain where $i = 15, 30, \cdots, 405$ (group of 27), $j = 12, 24, \cdots, 312$ (group of 26) for the layers in which $k = 1$ and $k = 5$ (group of 2) where the depth of reservoir is from 6000 to 6062.5 $[m]$ and from 6250 to 6312.5 $[m]$, respectively. All the result figure plots are rotated with the original azimuth (36.9°).

6.3.1 σ_{Hmax} and σ_{hmin} for CASE 0: homogeneous stress distribution with unconstrained data

The following are result plots of and for the base case, Case 0. Since we simulate with the volume-averaged single value as in Table 6.2 or Table 6.4, we do not have much variation and difference over the domain.

6.3.2 σ_{Hmax} and σ_{hmin} for CASE 1: homogeneous stress distribution with constrained data

Next are result plots of σ_{Hmax} and σ_{hmin} for Case 1 where the well data is constrained and honored. Although we simulate with the same input as Case 0, we have a bit more

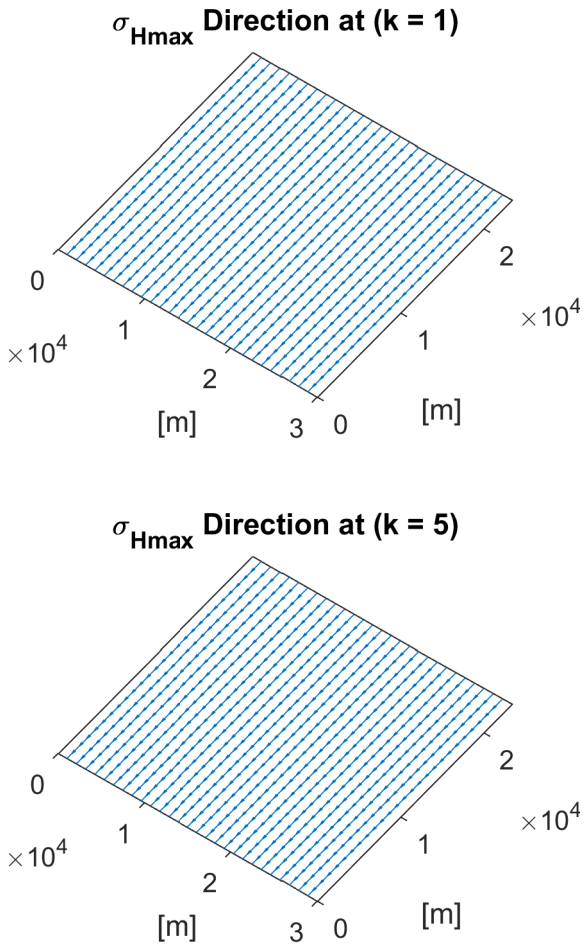

Figure 6.4: Direction of σ_{Hmax} for CASE 0.

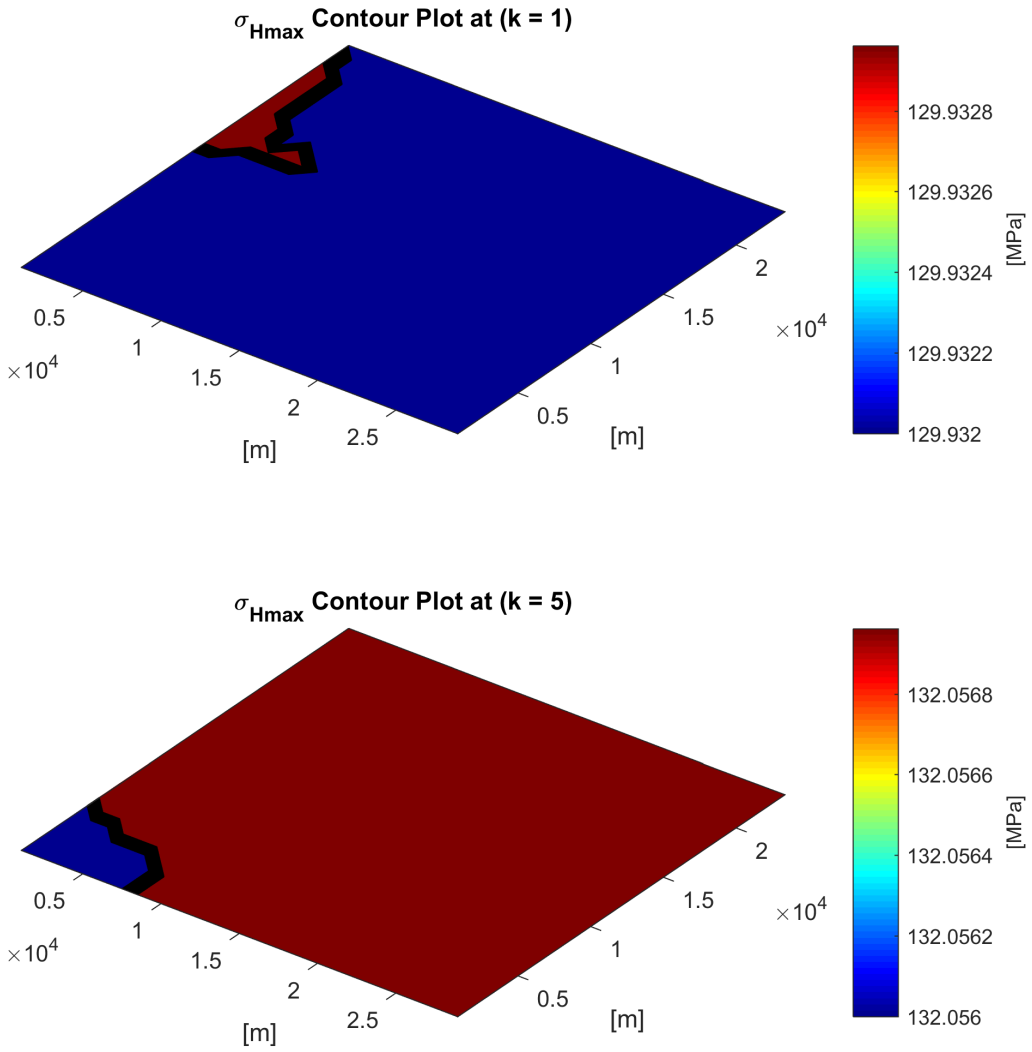

Figure 6.5: σ_{Hmax} values for CASE 0.

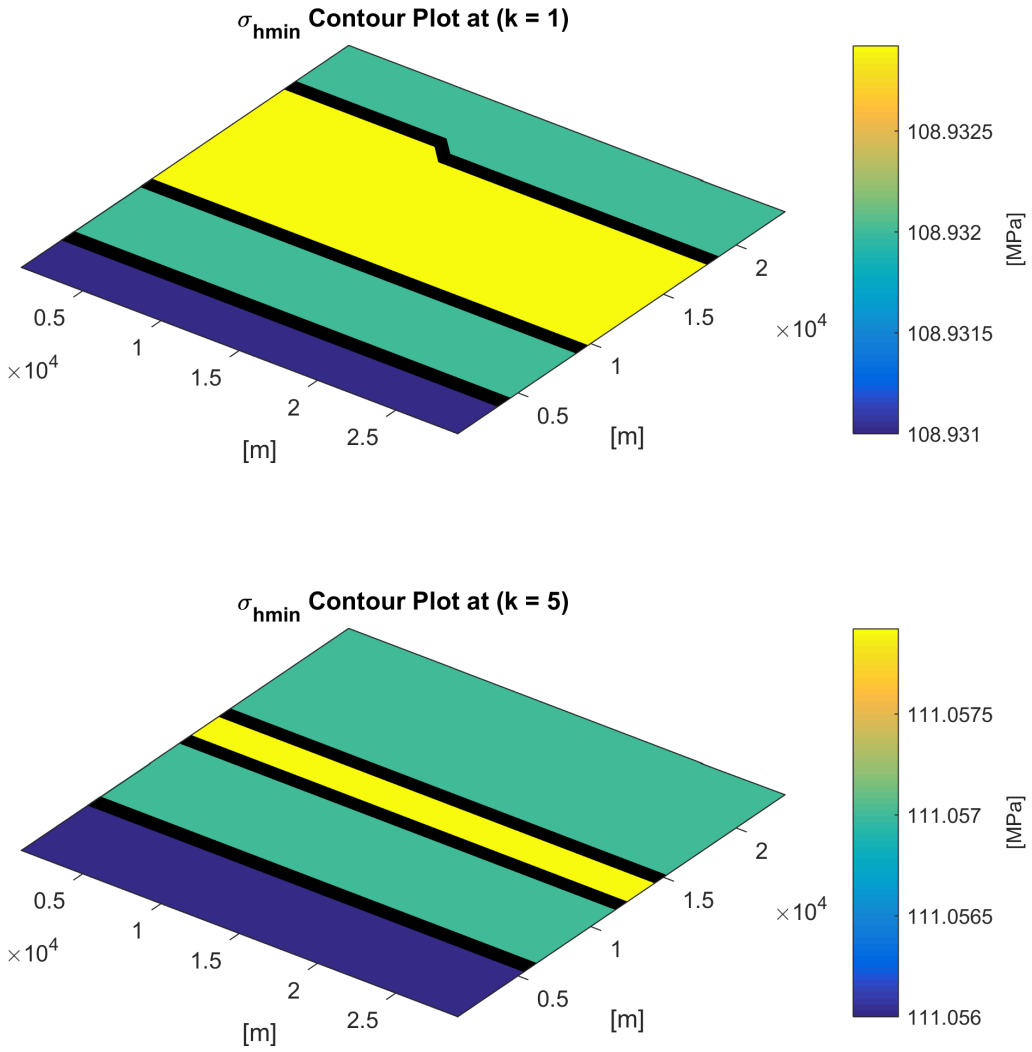

Figure 6.6: σ_{hmin} values for CASE 0.

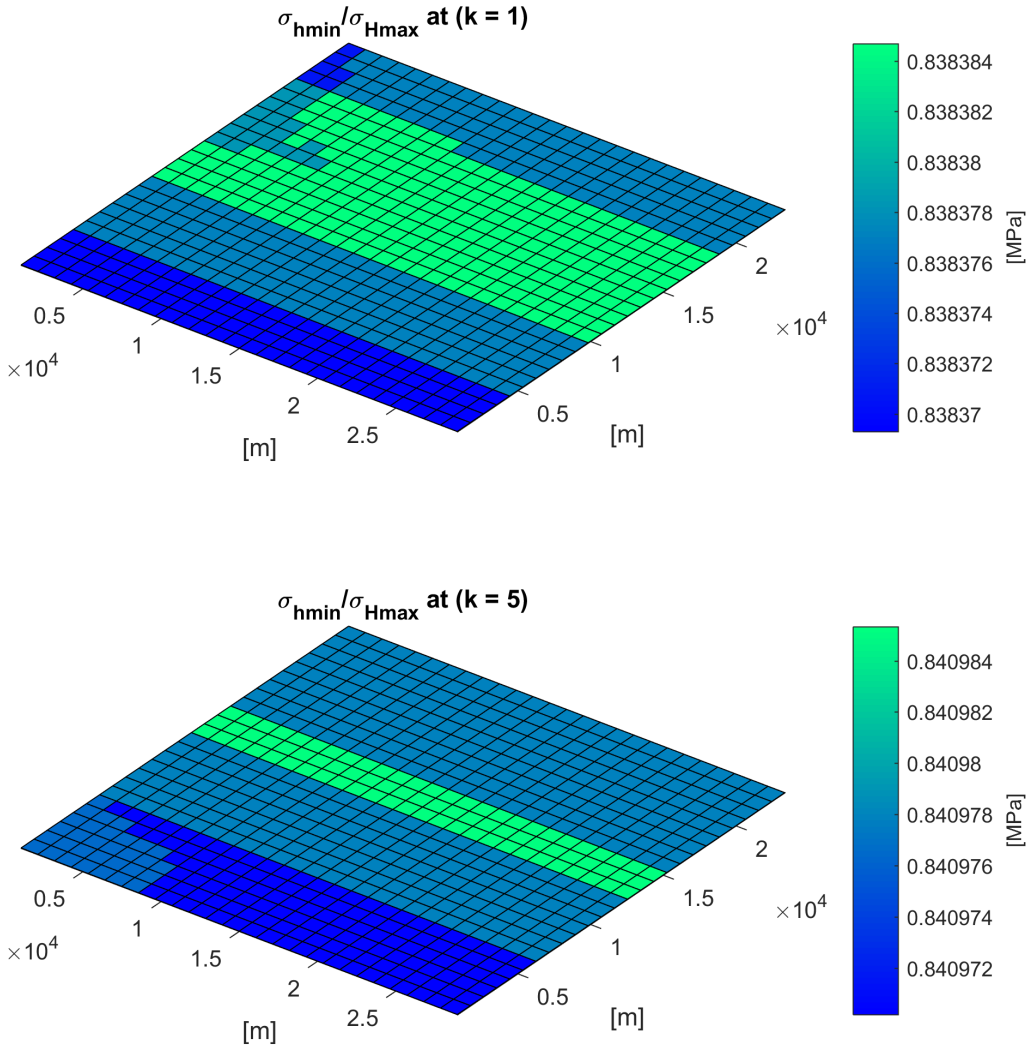

Figure 6.7: $\sigma_{hmin}/\sigma_{Hmax}$ ratio for CASE 0.

variation of σ_{Hmax} and σ_{hmin} over the domain, especially around the 7 well locations that are constrained. Note that σ_{Hmax} direction is identical as Case 0 which is the average direction for the whole domain.

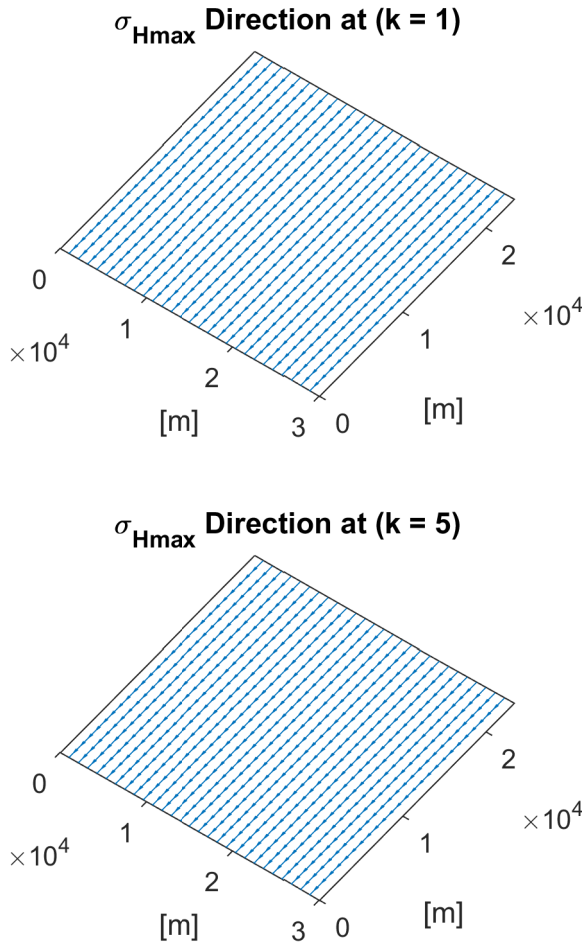

Figure 6.8: Direction of σ_{Hmax} for CASE 1.

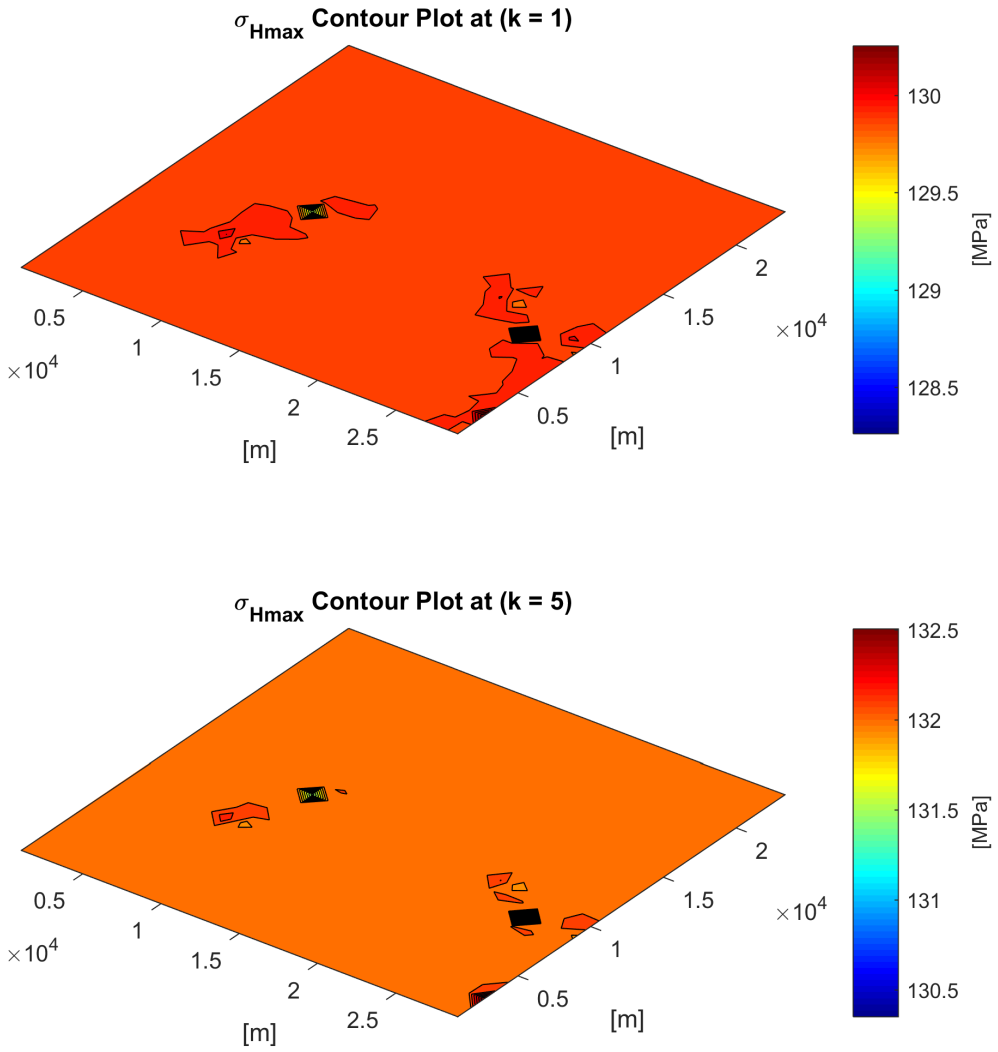

Figure 6.9: σ_{Hmax} values for CASE 1.

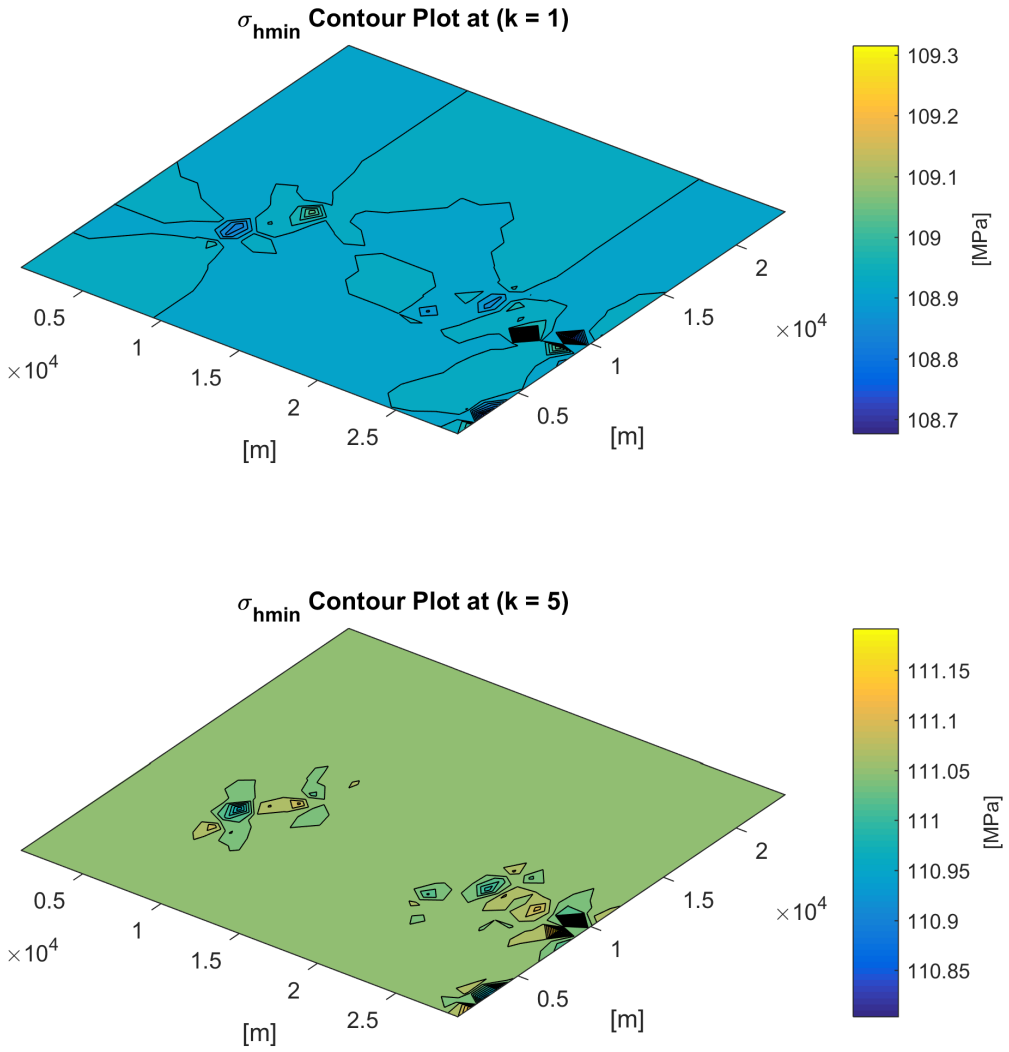

Figure 6.10: σ_{hmin} values for CASE 1.

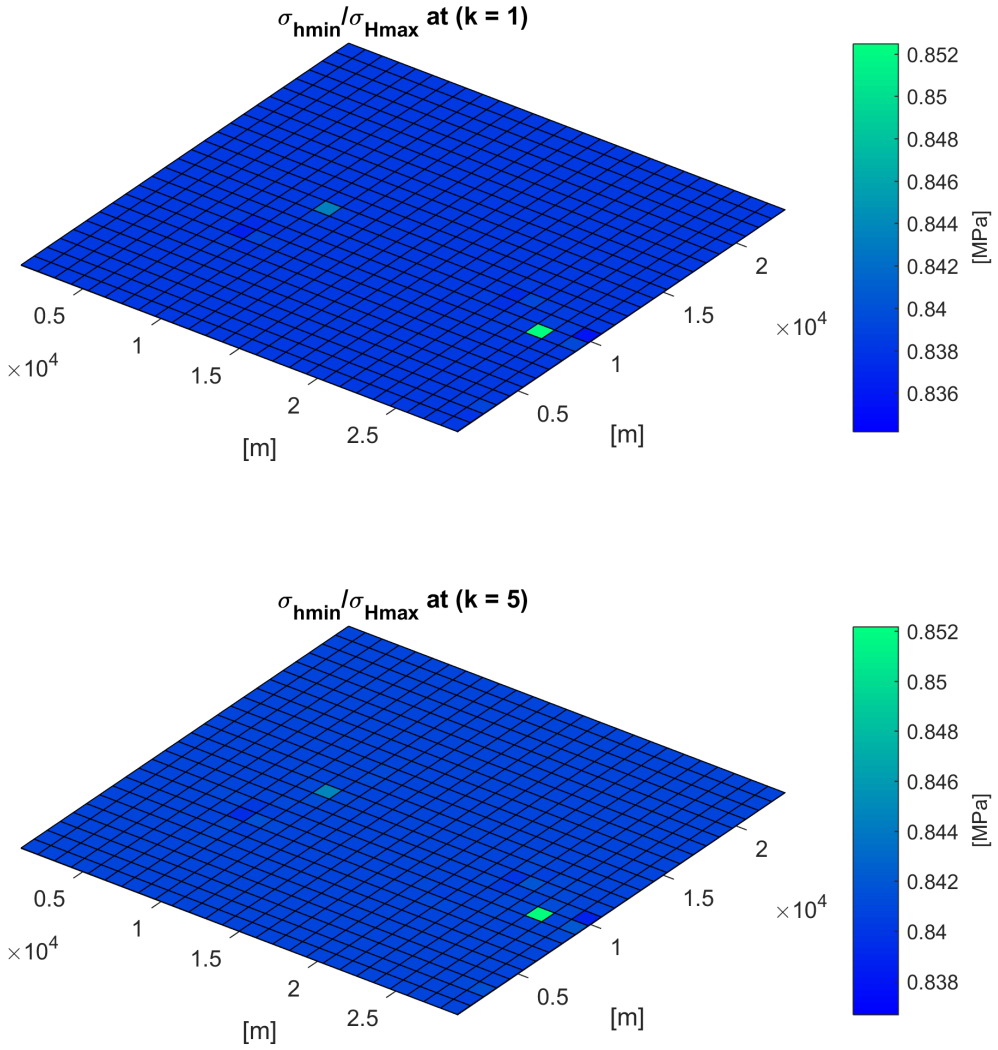

Figure 6.11: $\sigma_{hmin}/\sigma_{Hmax}$ ratio for CASE 1.

6.3.3 σ_{Hmax} and σ_{hmin} for CASE 2: heterogeneous stress distribution with unconstrained data

The plots that follow are result plots of σ_{Hmax} and σ_{hmin} for Case 2 where we generated initial input stress data using ordinary Kriging method. In this case, we do not constrain any well data. We can see severe variations due to heterogeneity not only in σ_{Hmax} direction and value but also in σ_{hmin} with their ratio.

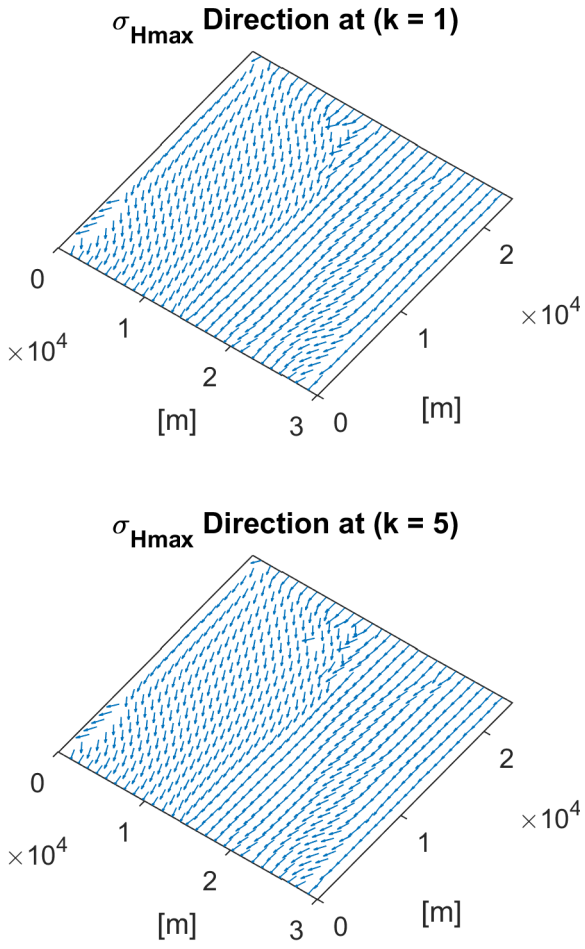

Figure 6.12: Direction of σ_{Hmax} for CASE 2.

6.3.4 σ_{Hmax} and σ_{hmin} for CASE 3: heterogeneous stress distribution with constrained data

The last is the result plots of σ_{Hmax} and σ_{hmin} for Case 3 where we generated initial input stress data using Kriging method and we constrain all the 7 well data. For these results of σ_{Hmax} and σ_{hmin} distribution plots, however, not much difference can be detected from Case 2, since the variations occur around the constrained well locations.

6.3.5 Differences between input and output: initial guess and result data of σ_{Hmax} distributions for all CASEs

We calculate the absolute difference values between input and output in σ_{Hmax} value by just subtracting the result values from the input data in each case. As we can see from Case 0 through Case 3, the delta values are increasing by heterogeneity and the constrained data, although not much differences between Case 2 and Case 3 are shown in the plots as well.

6.3.6 7 constrained well data for homogeneous and heterogeneous cases

In this section, we plot the stress distribution of σ_{Hmax}, σ_{hmin} and σ_V for 7 constrained sets of well data over the layers, $k = 1, 2, \cdots, 8$. The black lines indicate the measured data and we can see that the red lines are well honoring the same data for all cases, homogeneous and heterogeneous. Since we use the single averaged value for direction, vertical straight lines are plotted for the direction values. Unlike the homogenous case where σ_{Hmax}, σ_{hmin} and σ_V are linearly plotted, we see the zig-zag or nonlinear distribution of them for constrained well data over the depth due to honoring the well data.

6.4 Summary

We simulated total 4 cases using unconstrained and constrained mechanics with homogeneous and heterogeneous stress distribution for initial input data. For constrained

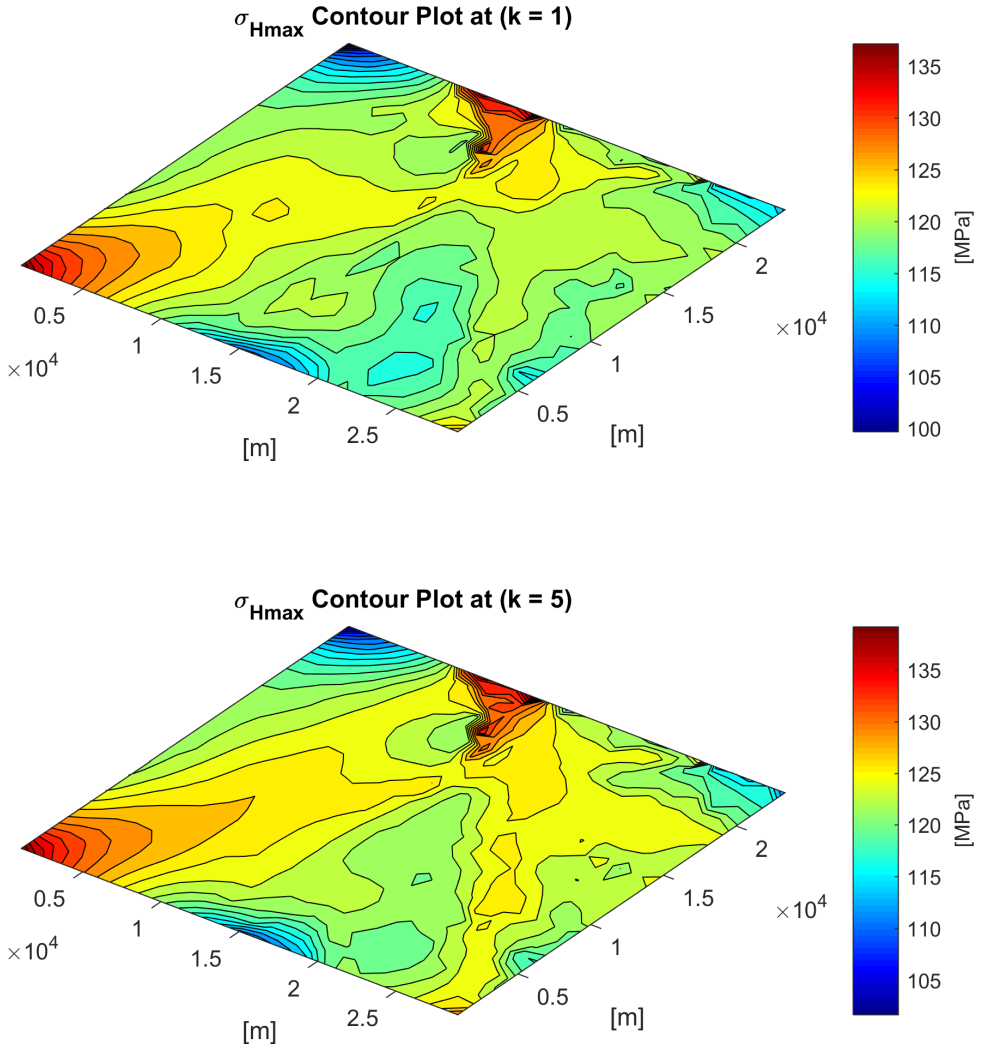

Figure 6.13: σ_{Hmax} values for CASE 2.

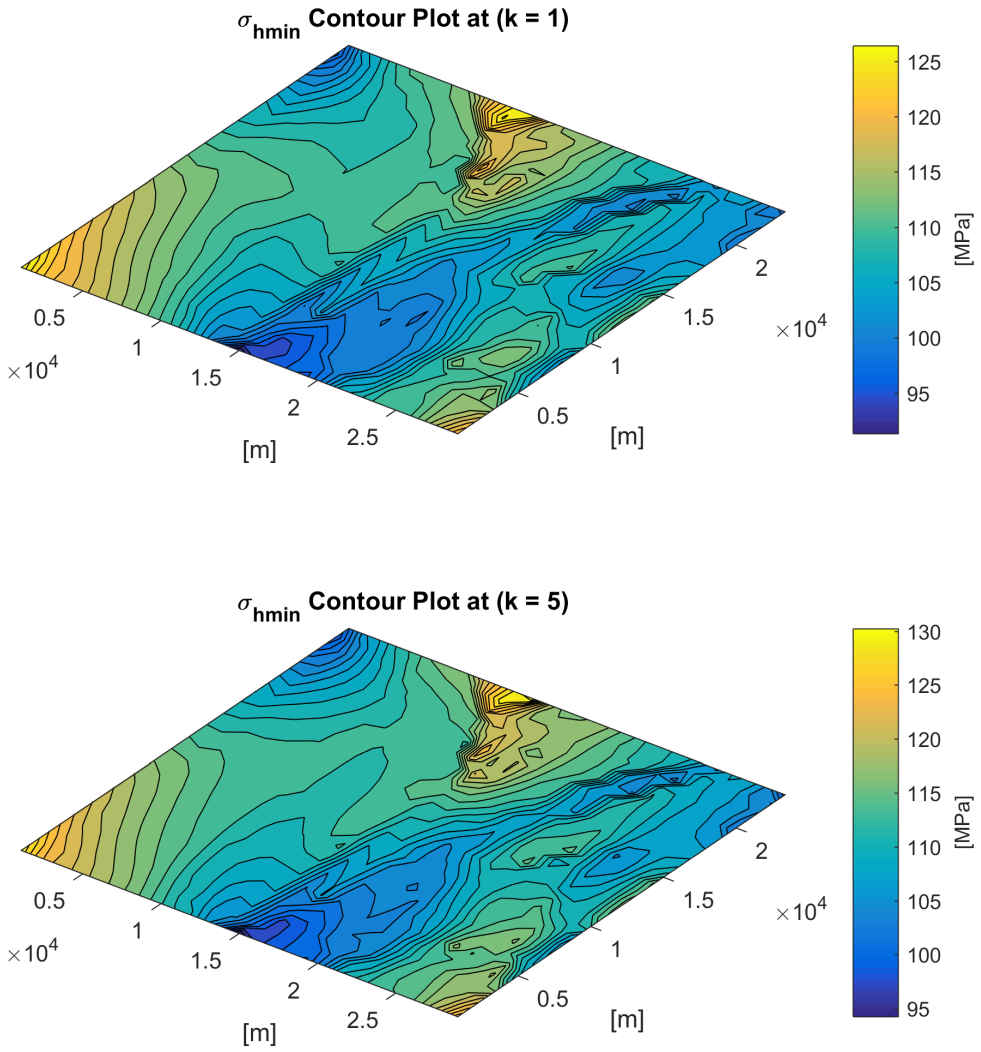

Figure 6.14: σ_{hmin} values for CASE 2.

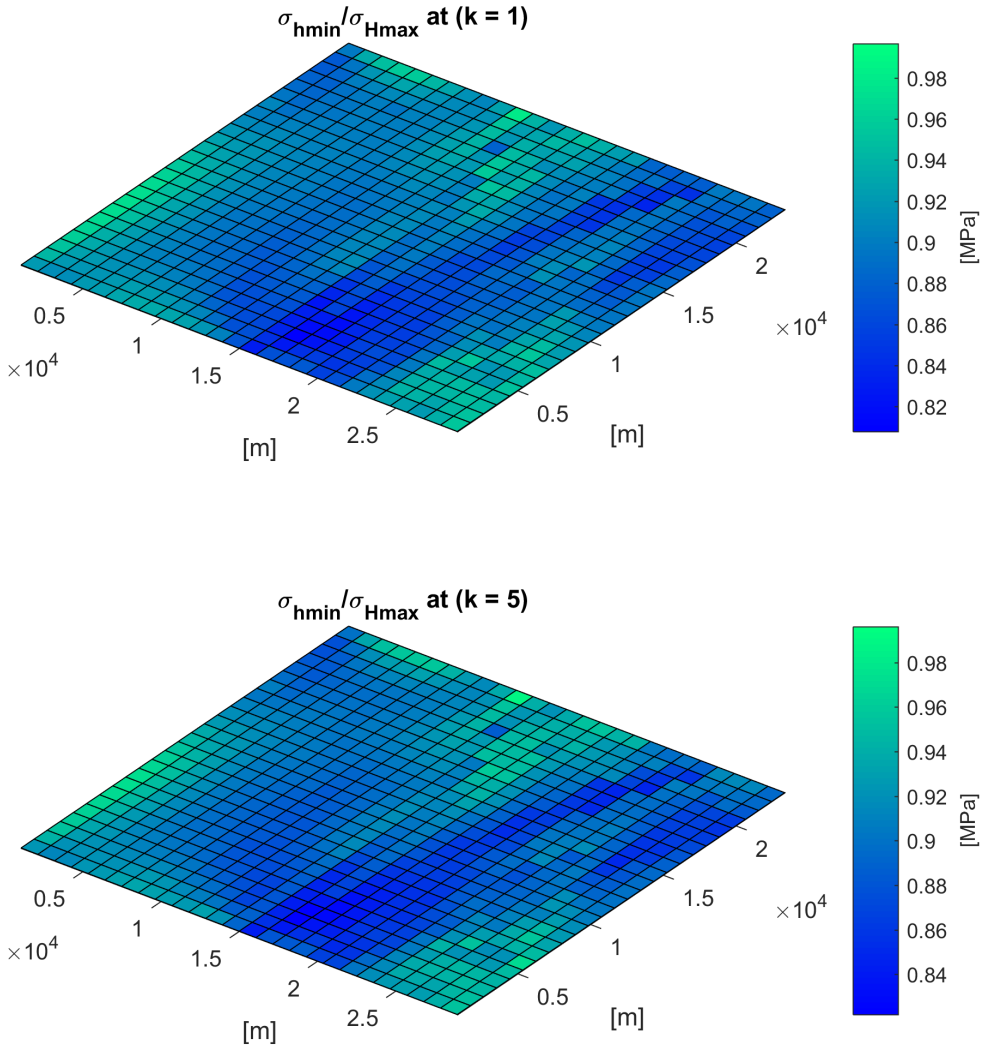

Figure 6.15: $\sigma_{hmin}/\sigma_{Hmax}$ ratio for CASE 2.

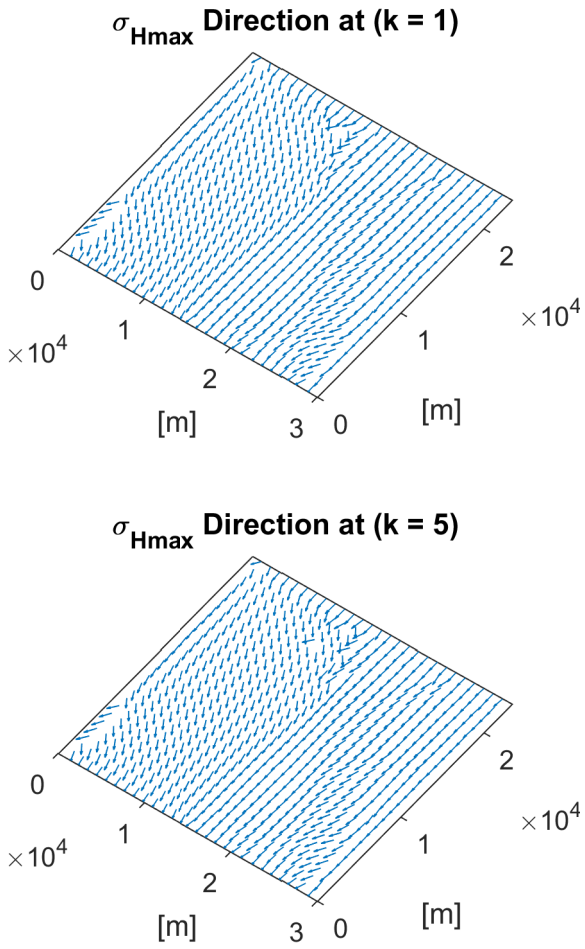

Figure 6.16: Direction of σ_{Hmax} for CASE 3.

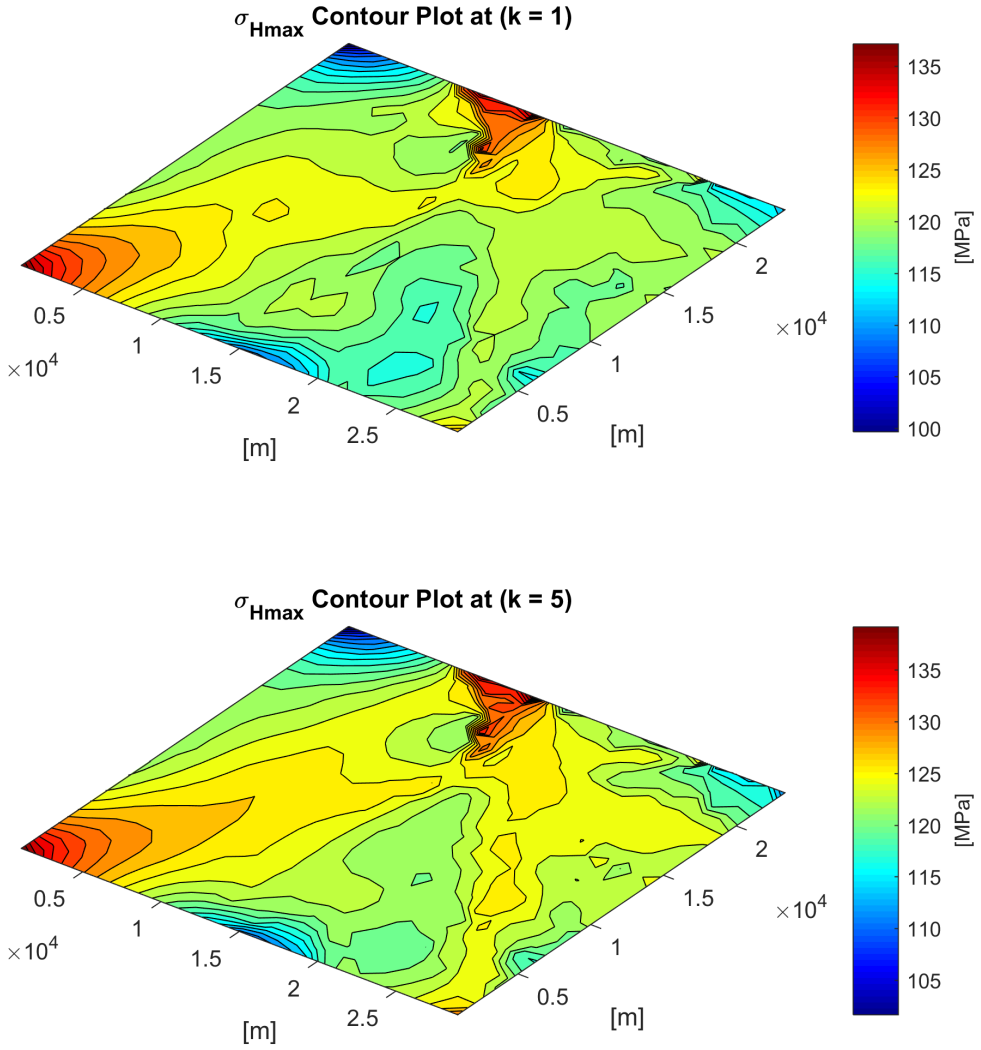

Figure 6.17: σ_{Hmax} values for CASE 3.

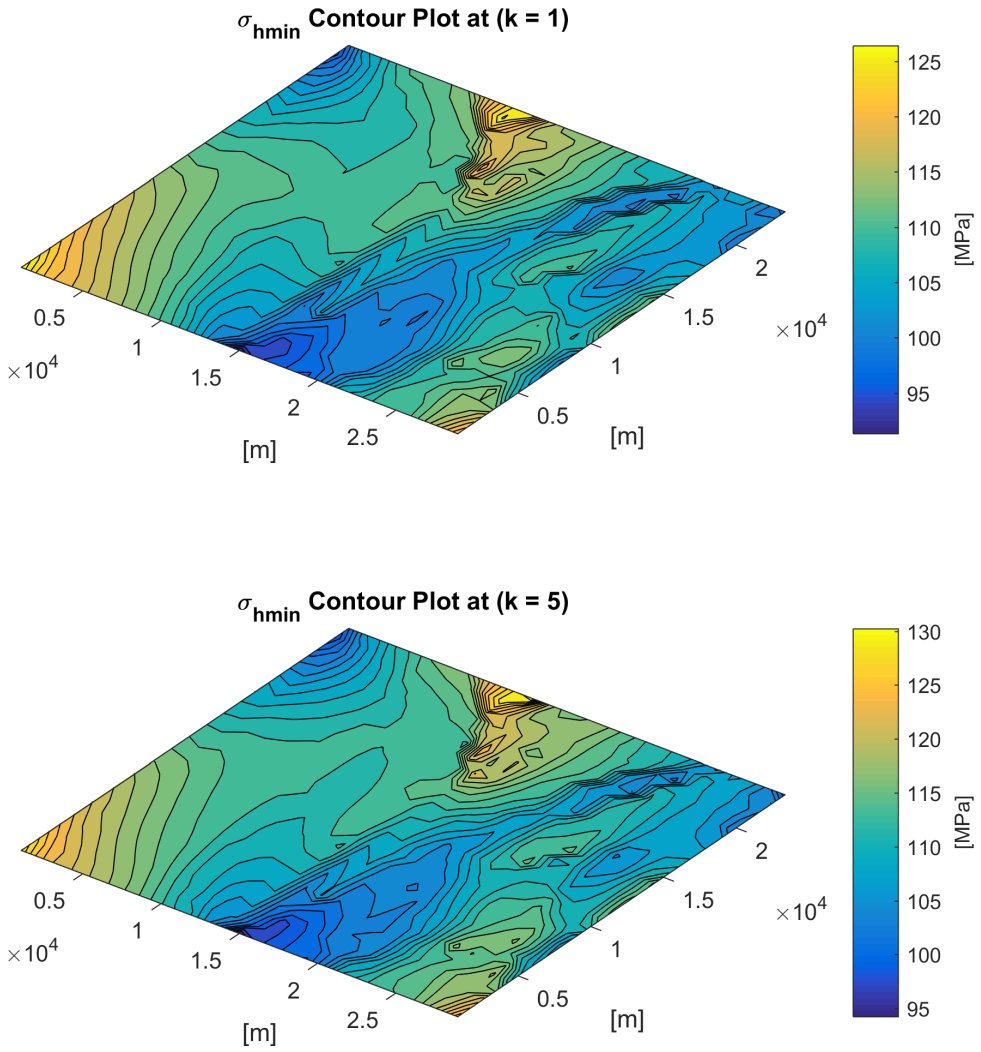

Figure 6.18: σ_{hmin} values for CASE 3.

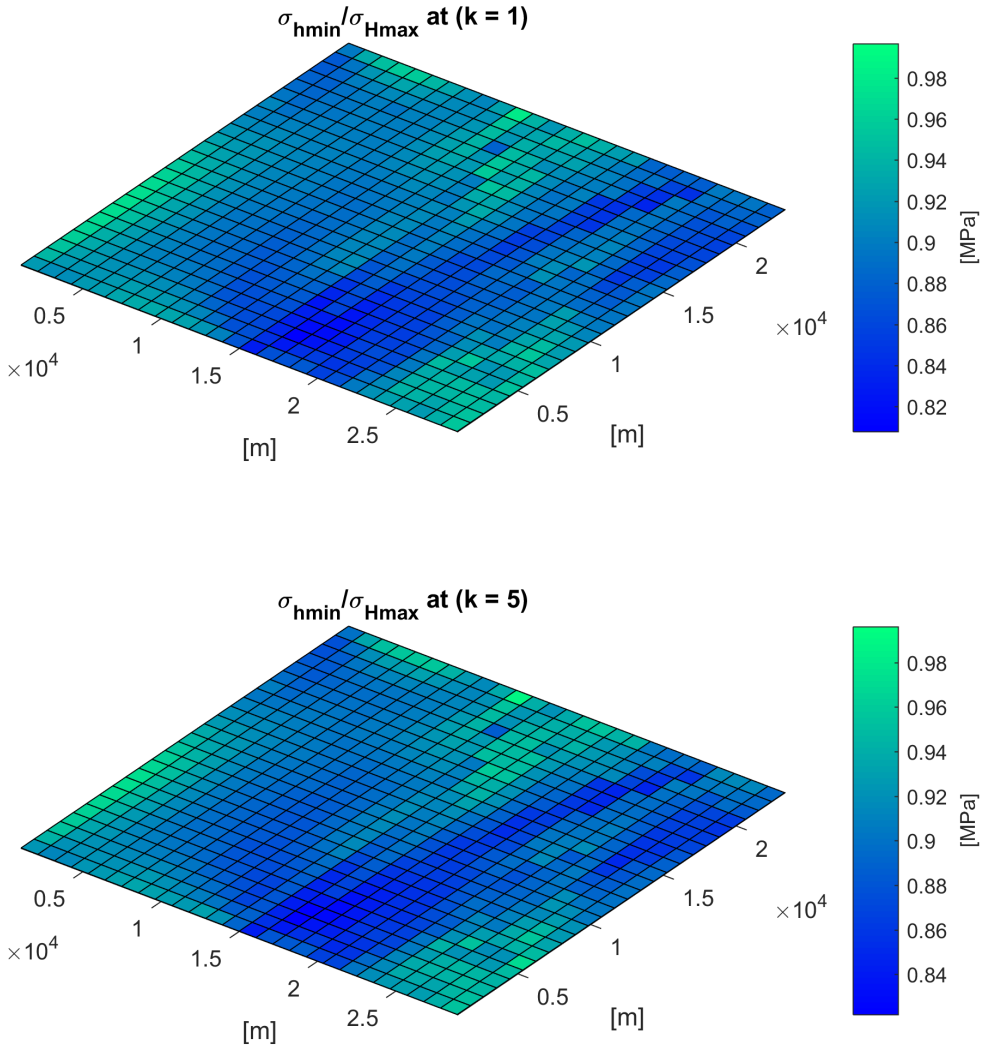

Figure 6.19: $\sigma_{hmin}/\sigma_{Hmax}$ ratio for CASE 3.

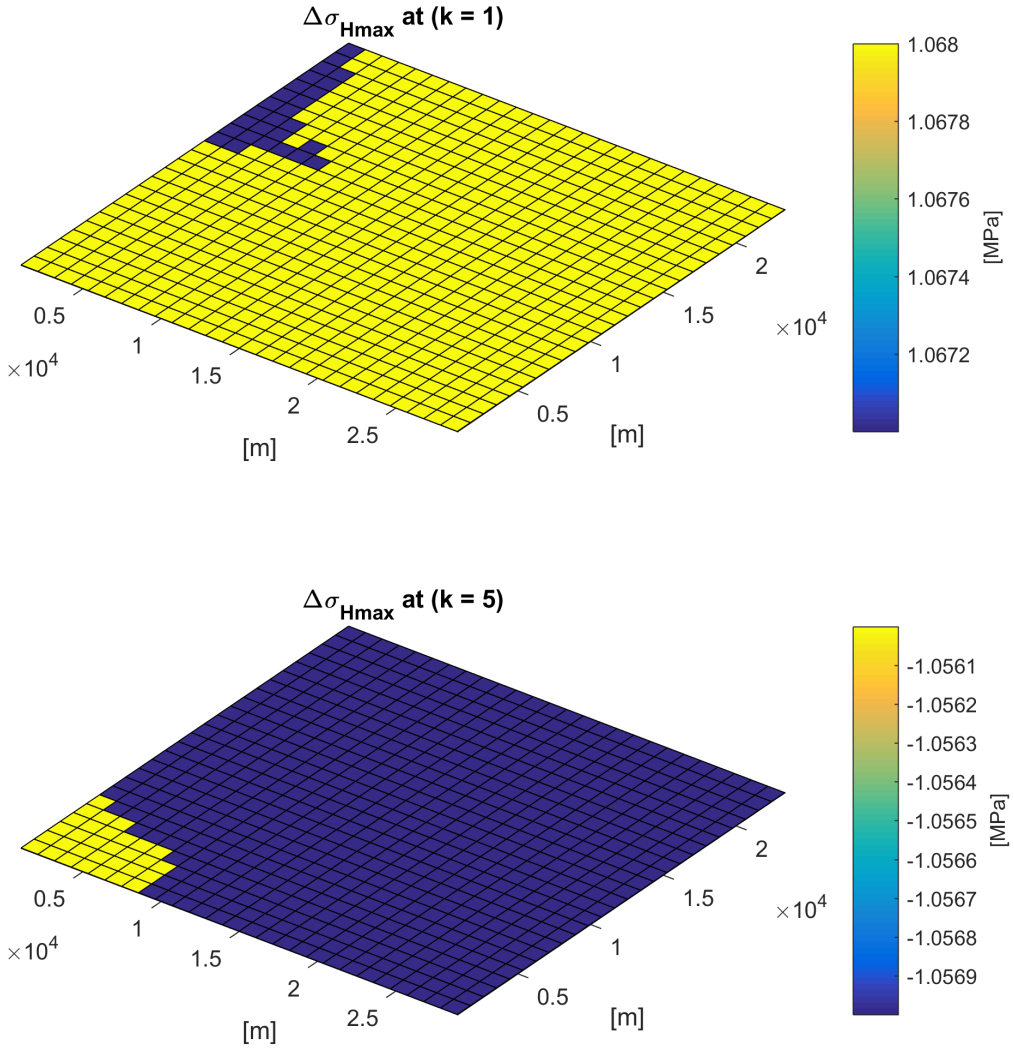

Figure 6.20: $\Delta\sigma_{Hmax}$ for CASE 0.

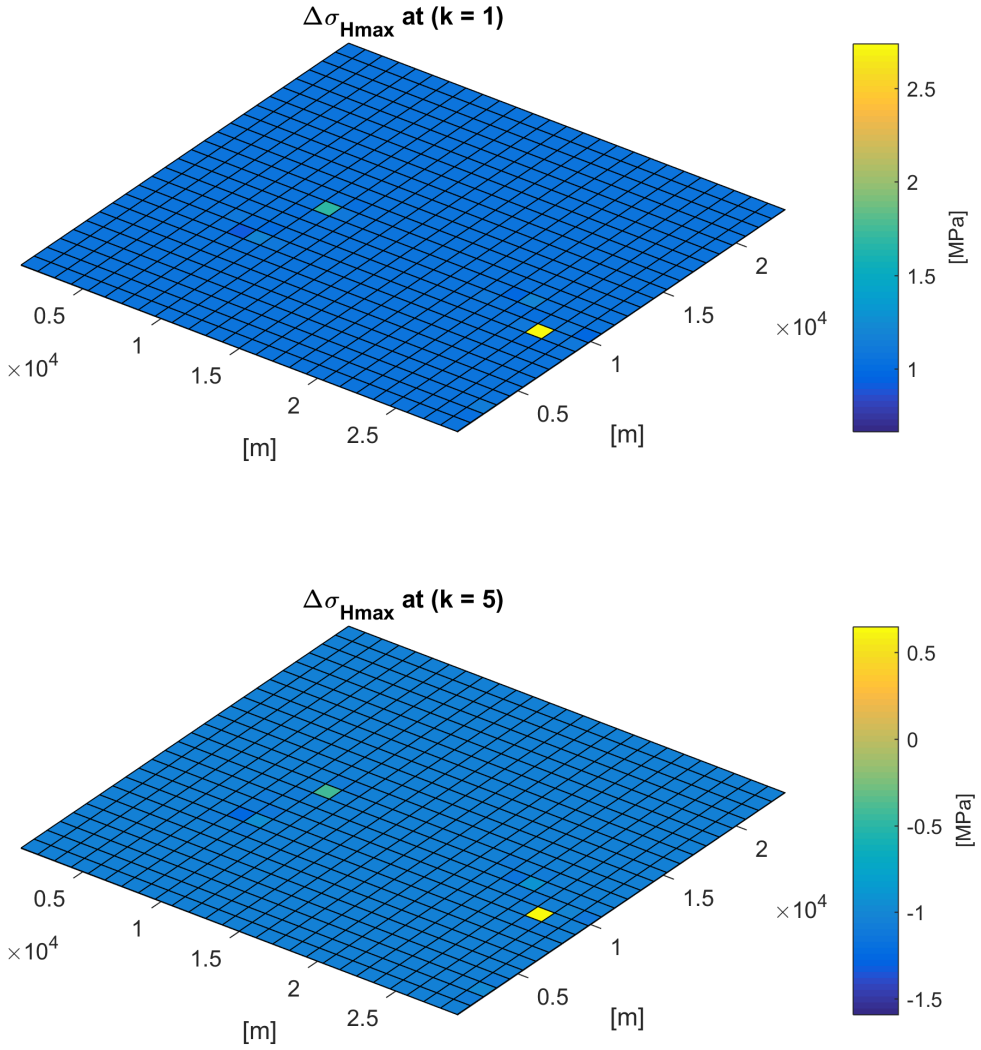

Figure 6.21: $\Delta\sigma_{Hmax}$ for CASE 1.

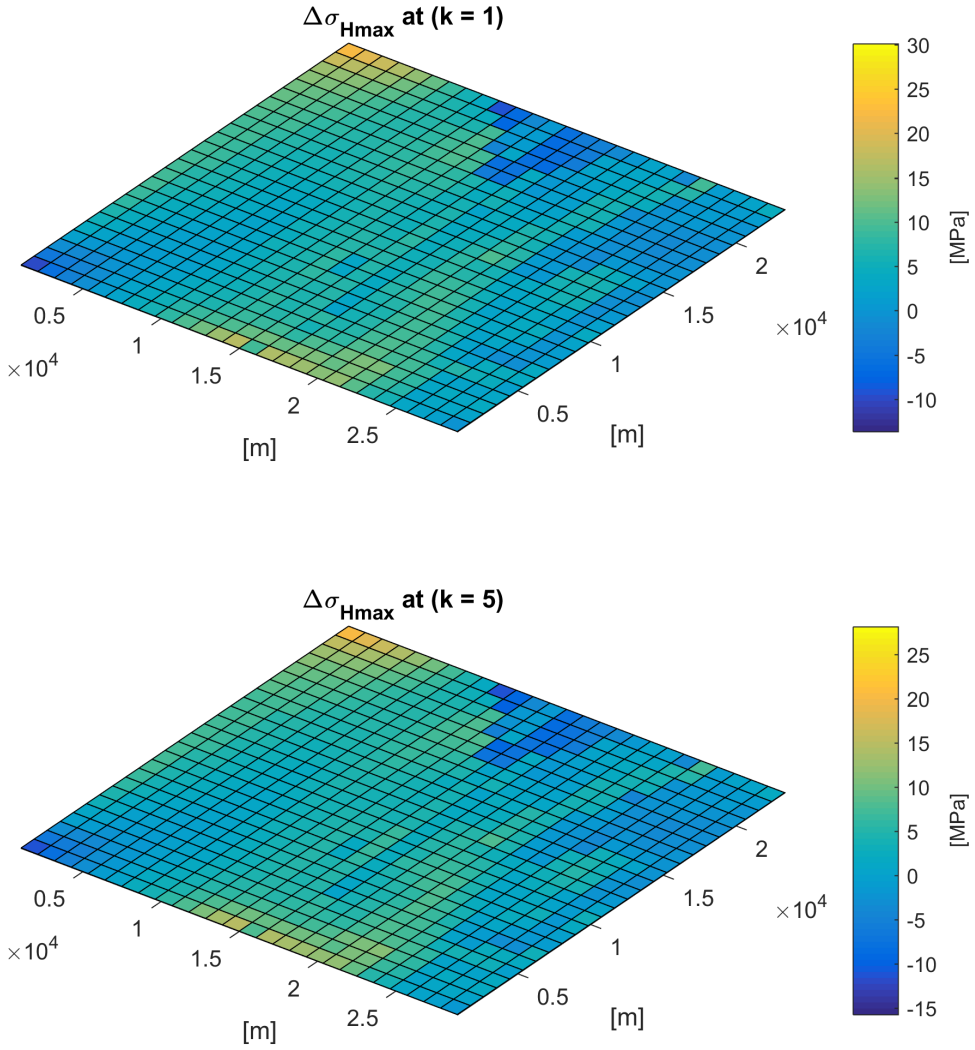

Figure 6.22: $\Delta\sigma_{Hmax}$ for CASE 2.

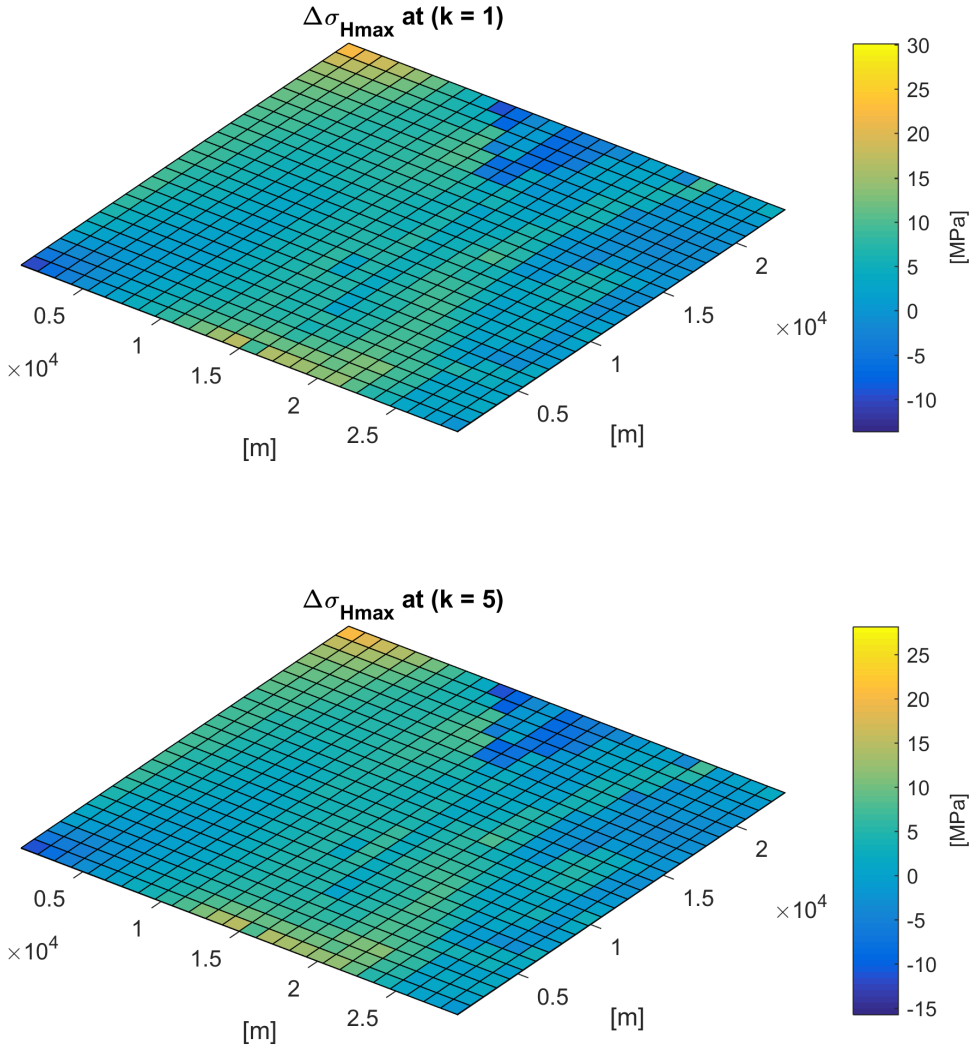

Figure 6.23: $\Delta\sigma_{Hmax}$ for CASE 3.

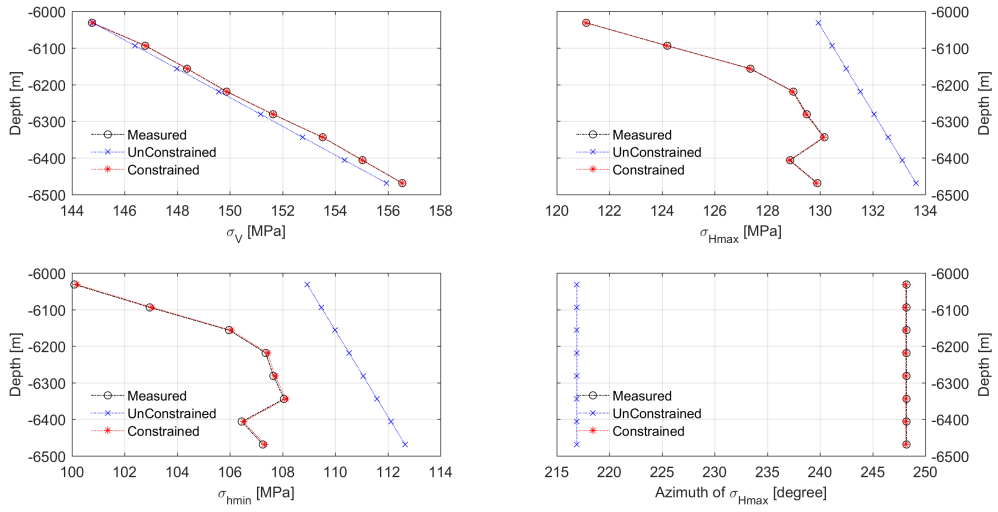

(a) homogeneous for Well 1

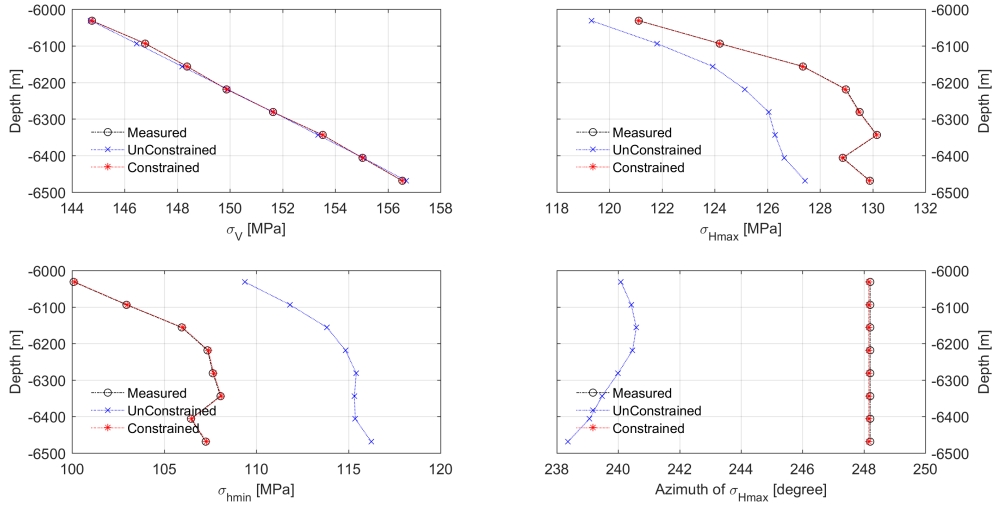

(b) heterogeneous for Well 1

Figure 6.24: Well 1 data and simulation results for σ_{Hmax}, σ_{hmin} and σ_V.

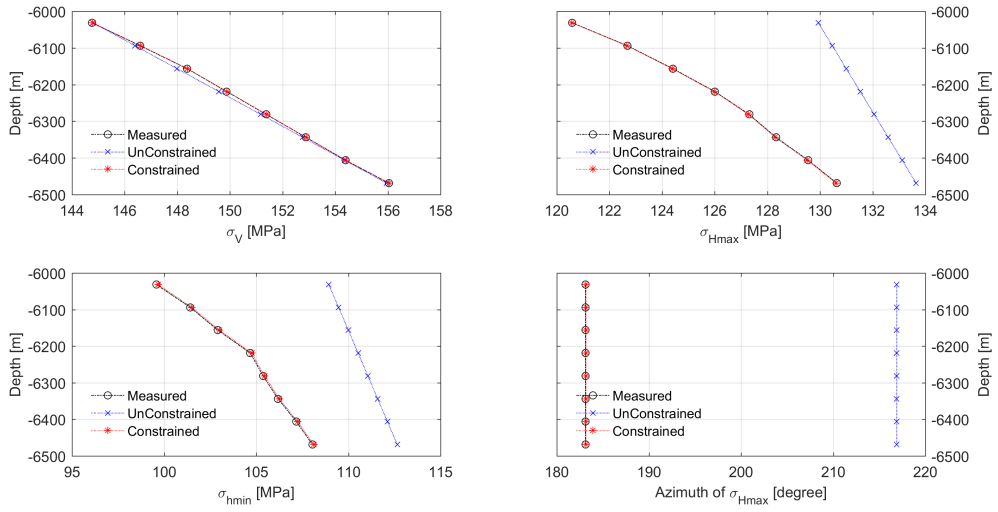

(a) homogeneous for Well 2

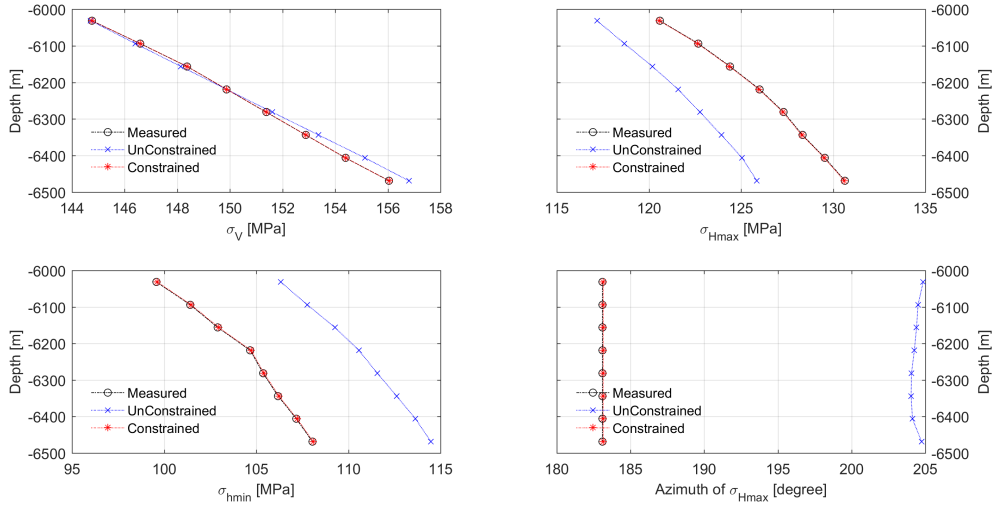

(b) heterogeneous for Well 2

Figure 6.25: Well 2 data and simulation results for σ_{Hmax}, σ_{hmin} and σ_V.

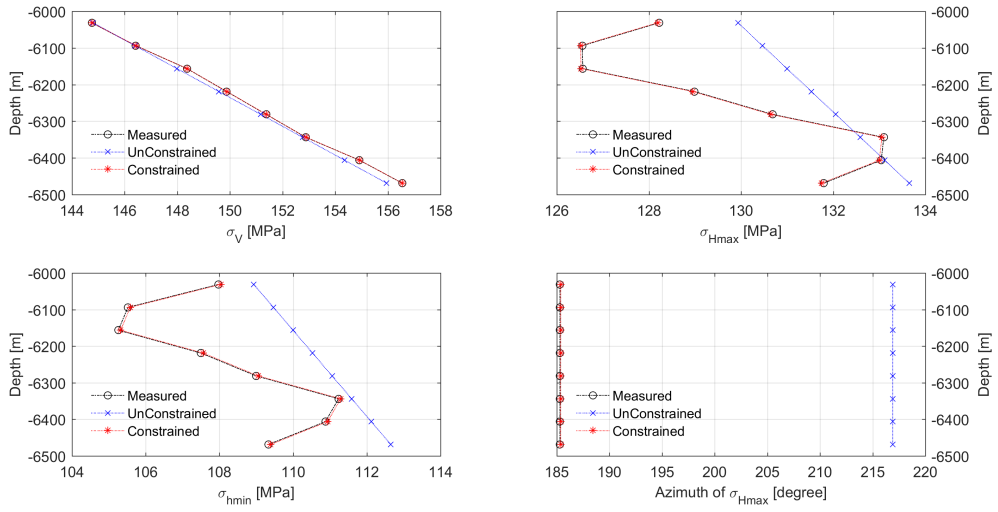

(a) homogeneous for Well 3

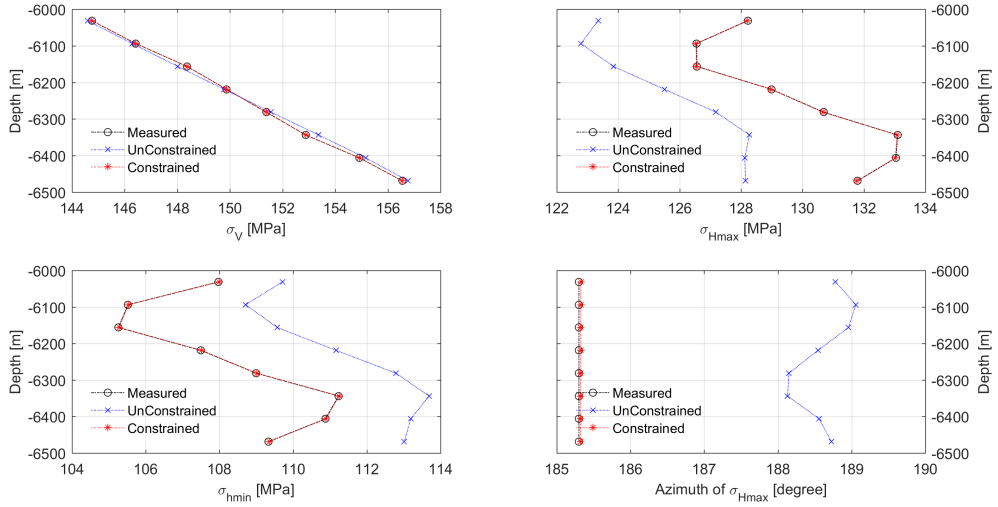

(b) heterogeneous for Well 3

Figure 6.26: Well 3 data and simulation results for σ_{Hmax}, σ_{hmin} and σ_V.

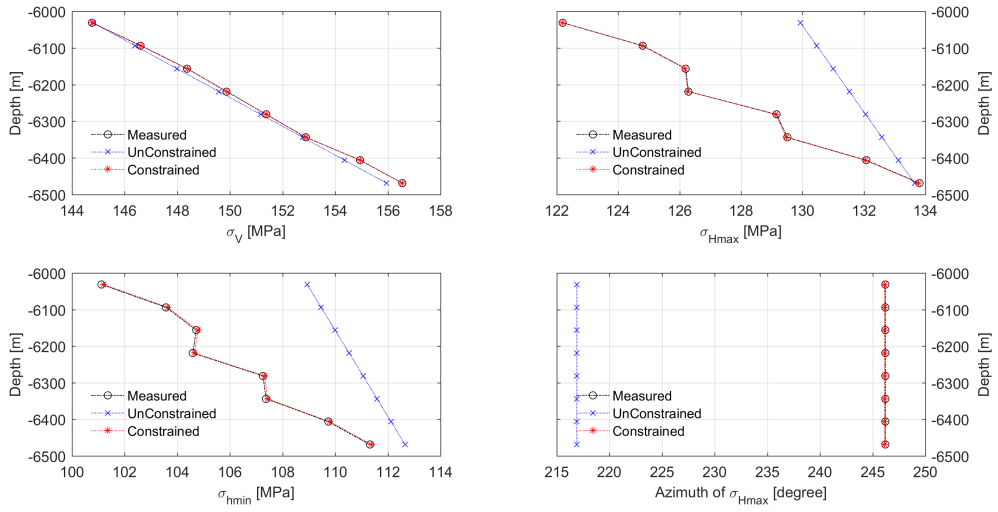

(a) homogeneous for Well 4

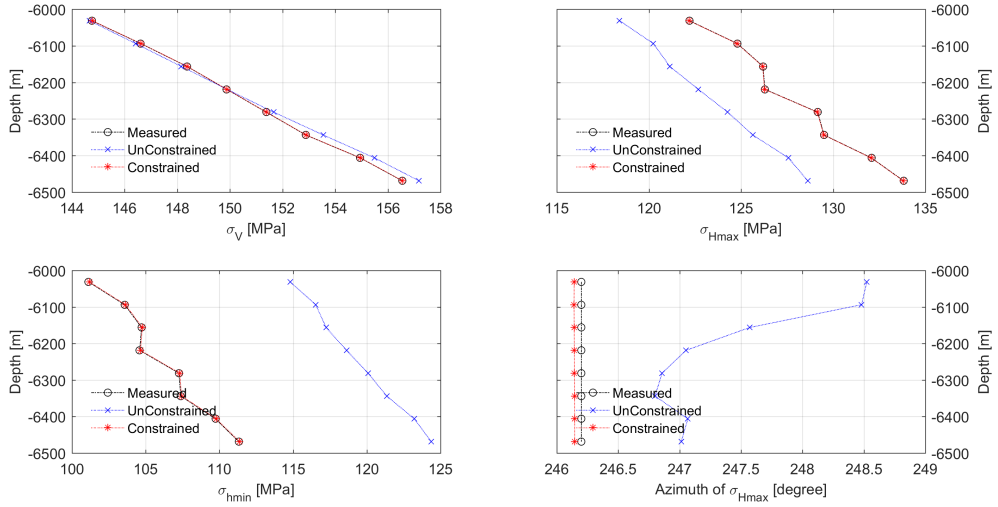

(b) heterogeneous for Well 4

Figure 6.27: Well 4 data and simulation results for σ_{Hmax}, σ_{hmin} and σ_V.

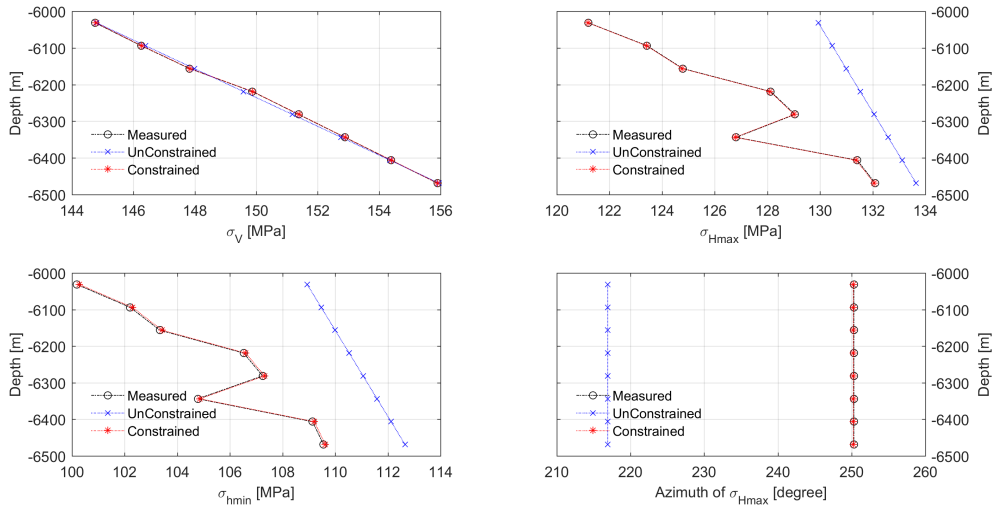

(a) homogeneous for Well 5

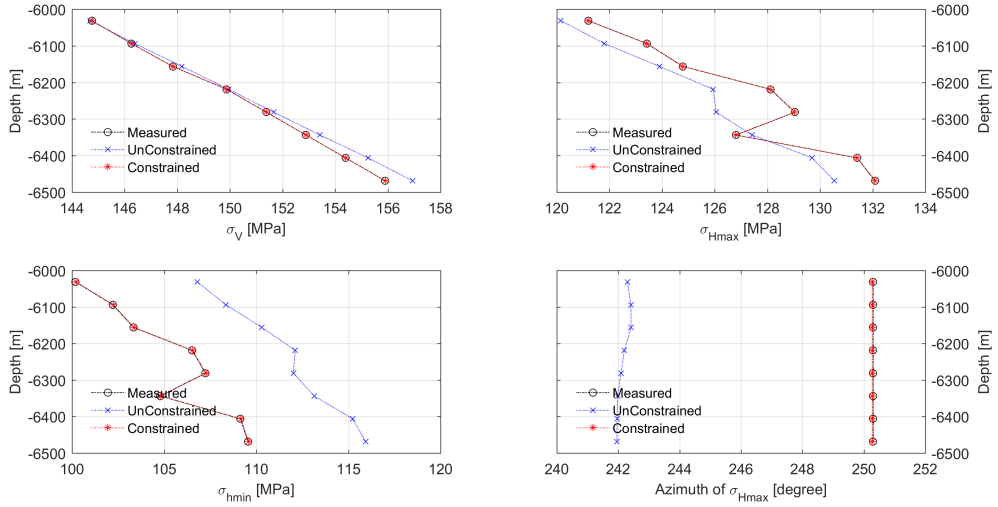

(b) heterogeneous for Well 5

Figure 6.28: Well 5 data and simulation results for σ_{Hmax}, σ_{hmin} and σ_V.

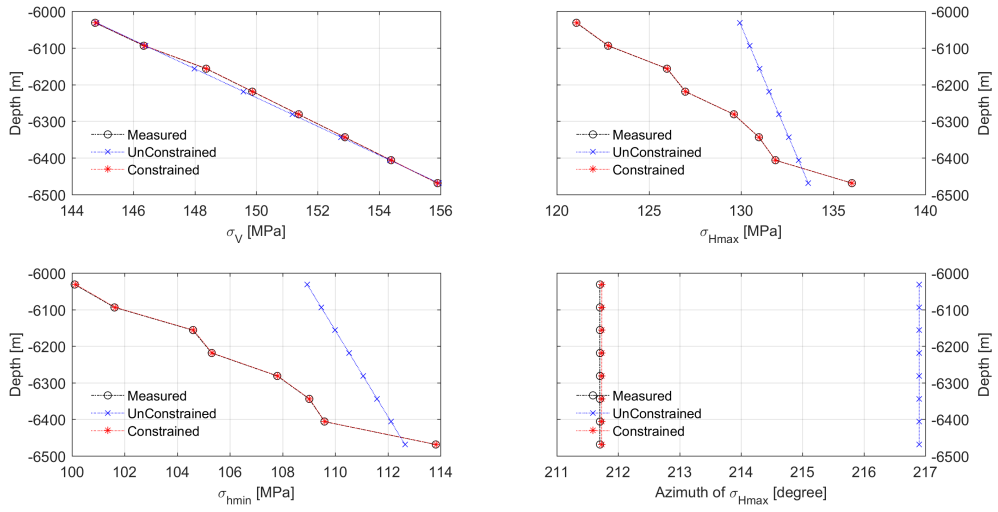

(a) homogeneous for Well 6

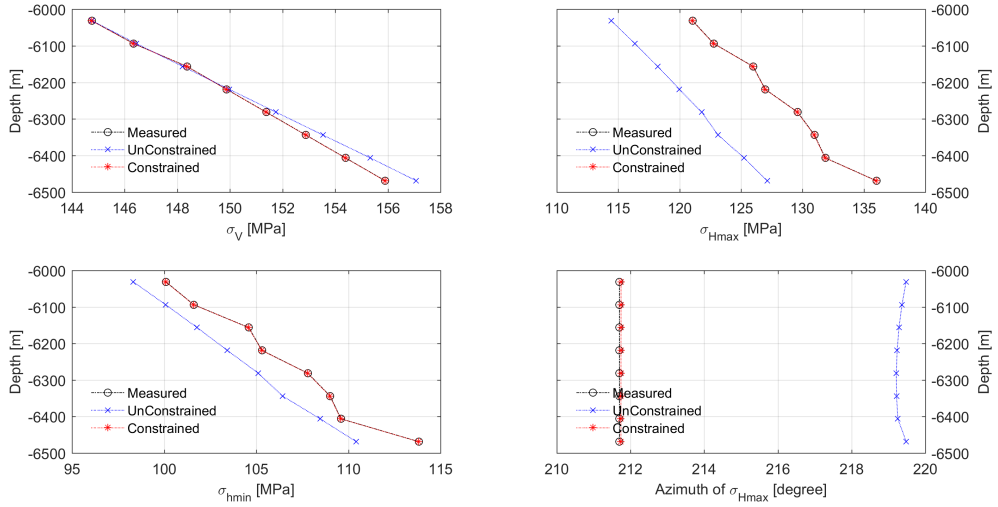

(b) heterogeneous for Well 6

Figure 6.29: Well 6 data and simulation results for σ_{Hmax}, σ_{hmin} and σ_V.

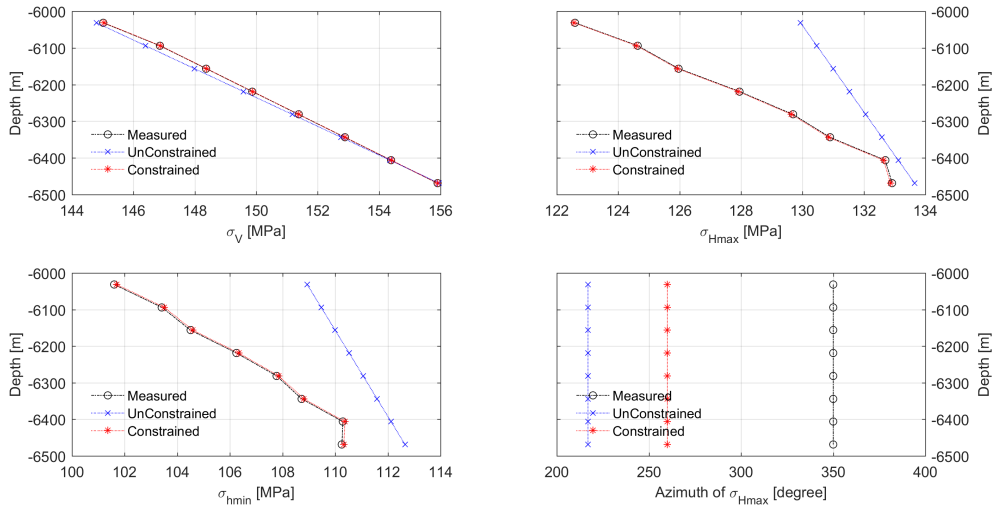

(a) homogeneous for Well 7

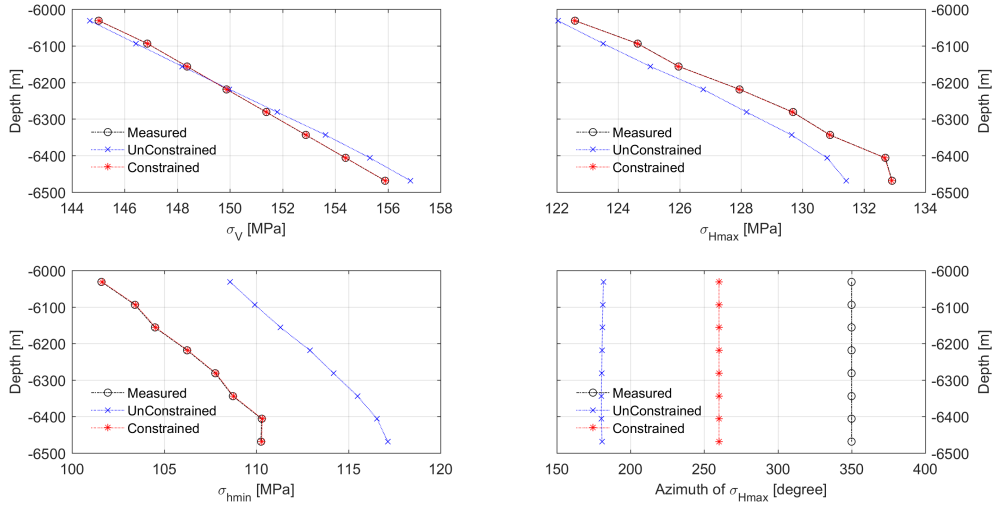

(b) heterogeneous for Well 7

Figure 6.30: Well 7 data and simulation results for σ_{Hmax}, σ_{hmin} and σ_V.

mechanics, we used the Uzawa iteration algorithm to overcome the saddle point problem. For heterogeneity, ordinary Kriging method was applied. Through the simulations, we obtained satisfying results of the in-situ initial stress distribution for the domain, and we conclude that input data and the constrained mechanics are the key for the estimation. Through this application, we find out that honoring the real data in poromechanics can work as a constraint against the accurate calculations. Using an appropriate formulation of a numerical algorithm, however, we can honor the data correctly and obtain more feasible and accurate solution.

7. SUMMARY AND CONCLUSIONS

With gaining importance of geomechanics in petroluem engineering nowadays, the accurate prediction of reservoir performance with geomechanical effects is getting highly critical. From both the a-priori and the a-posteriori analysis, with mathematical formulations and numerical experiments of this study, we found that there can be several numerical and physical issues inhibiting accurate calculations, accompanied with poromechanics, all of which are working against the precise and accurate solution.

As the spatial stability issue, for an early time of simple consolidation simulation, we found that there can be the discontinuity condition in pressure at the drainage boundary and even that the whole system sometimes can lead to the incompressible system, related to the inf-sup condition. Violating either condition leads to severe instabilities with oscillations in space, even to the non-uniqueness of solution. In order to obtain the accurate numerical solutions, appropriate spatial discretizations with proper solution strategy must be chosen, and specifically for reservoir simulation, the Q1P0 with the fixed-stress split is recommended through our study.

Furthermore, poromechanics itself possess the inherent structures working against the accuracy, especially when we seek the higher-order of accuracy in time integration using operator splitting schemes. We applied the two higher-order operator splitting methods using the two-pass and SDC methods, but we found out that both methods do not work, due to two different factors: the DAEs index-1 system and the numerical approximation with fixing the rate. Thus, for the computational efficiency, the fractional-stepping, the one-step fixed-stress split method itself is recommended.

For the large deformation system with the non-linear elastic mechanical response, we found that the system can be highly sensitive to anisotropic properties with geomechanics

and fluid flow. Through numerical experiments, we found out that the inaccuracy within the system can be overcome with the total Lagrangian method for the configuration change and the MPFA for the flux approximation.

Finally as shown in an application, we performed a large field scale simulation with real well data. Through the study, we confirmed that appropriate formulation of the algorithm, such as the Uzawa's algorithm for the constrained mechanics with the saddle point problem, is recommended for overcoming the constraint while honoring data and for more feasible and accurate solutions.

In this study, we investigated various mixed formulations in space and time for the fixed-stress split method in poromechanics. Possessing the natural stabilization and convergence properties, we found out that the fixed-stress split method is a proper way to obtain more accurate solutions over some inhibiting issues. Further in-depth study should be followed, such as rigorous stability and convergence of the mixed formulations for more realistic conditions and problems. Nevertheless, through the study, along with appropriate mixed formulations in space and time discretizations for poromechanics, it is concluded that the fixed-stress split method can be the efficient and accurate strategy, compared to other methods.

REFERENCES

[1] C. Boyer, J. K. Suarez-Rivera, R. E. Lewis, and G. Waters, "Producing gas from its source," *Oilfield Review*, 2006.

[2] N. P. Roussel and M. M. Sharma, "Role of stress reorientation in the success of refracture treatments in tight gas sands," *SPE Journal*, 2012.

[3] A. Settari and F. Mourits, "A coupled reservoir and geomechanical simulation system," *SPE Journal*, vol. 3, pp. 219–226, 1998.

[4] A. Settari and D. A. Walters, "Advances in coupled geomechanical and reservoir modeling with applications to reservoir compaction," *SPE Journal*, vol. 6, no. 3, pp. 334–342, 2001.

[5] M. D. Zoback, *Reservoir Geomechanics*. Cambridge, UK: Cambridge University Press, 2007.

[6] J. Rutqvist and O. Stephansson, "The role of hydromechanical coupling in fractured rock engineering," *Hydrogeology Journal*, vol. 11, pp. 7–40, 2003.

[7] J. Rutqvist and G. J. Moridis, "Numerical studies on the geomechanical stability of hydrate-bearing sediments," *SPE Journal*, vol. 14, no. 2, pp. 267–282, 2009.

[8] D. Y. J. R. Jihoon Kim, G.J. Moridis, "Numerical studies on two-way coupled fluid flow and geomechanics in hydrate deposits," *SPEJ*, 2012.

[9] A. Masui, H. Haneda, Y. Ogata, and K. Aoki, "The effect of saturation degree of methane hydrate on the shear strength of synthetic methane hydrate sediments," in *International Conference on Gas Hydrates (ICGH 2005)*, (Trondheim, Norway), 12ï£¡16 June 2005.

[10] A. Masui, K. Miyazaki, H. Haneda, and K. Aoki, "Mechanical characteristics of natural and artificial gas hydrate bearing sediments," in *International Conference on*

Gas Hydrates (ICGH 2008), (Vancouver, Canada), 6ï£¡10 July 2008.

[11] G. Moridis, J. Kim, M. Reagan, and S. Kim, "Feasibility of gas production from a gas hydrate accumulation at the ubgh2-6 site of the ulleung basin in the korean east sea," *Journal of Petroleum Science and Engineering*, vol. 108, pp. 180–210, 2013.

[12] J. R. F. Cappa, "Impact of co2 geological sequestration on the nucleation of earthquakes," *Geophysical Research Letters*, vol. 38, 2011.

[13] M. D. Zoback and S. M. Gorelick, "Earthquake triggering and large-scale geologic storage of carbon dioxide," *PNAS*, vol. 109, no. 26, pp. 10164ï£¡–10168, 2012.

[14] J. Rutqvist, F. Cappa, A. Rinaldi, and M. Godano, "Modeling of induced seismicity and ground vibrations associated with geologic co2 storage, and assessing their effects on surface structures and human perception," *International Journal of Greenhouse Gas Control*, vol. 24, pp. 64ï£¡–77, 2014.

[15] B. Jha and R. Juanes, "Coupled multiphase flow and poromechanics: a computational model of pore-pressure effects on fault slip and earthquake triggering," *Water Resources Research*, vol. 50, pp. 3776ï£¡–3808, 2014.

[16] J. Rutqvist, A. Rinaldi, F. Cappa, and G. Moridis, "Modeling of fault reactivation and induced seismicity during hydraulic fracturing of shale-gas reservoirs," *Journal of Petroleum Science and Engineering*, vol. 107, pp. 31ï£¡–44, 2013.

[17] P. Jeanne, J. Rutqvist, C. Hartline, J. Garcia, P. Dobson, and M. Walters, "Reservoir structure and properties from geomechanical modeling and microseismicity analyses associated with an enhanced geothermal system at the geysers, california," *Geothermics*, vol. 51, pp. 460ï£¡–469, 2014.

[18] J. Rutqvist, A. Rinaldi, F. Cappa, and G. Moridis, "Modeling of fault activation and seismicity by injection directly into a fault zone associated with hydraulic fracturing of shale-gas reservoirs," *Journal of Petroleum Science and Engineering*, 2015. In press, online Feb. doi:10.1016/j.petrol.2015.01.019.

[19] O. Coussy, *Poromechanics*. Chichester, England: John Wiley and Sons, 2004.

[20] R. W. Lewis and B. A. Schrefler, *The finite element method in the static and dynamic deformation and consolidation of porous media*. Chichester, England: Wiley, second ed., 1998.

[21] Y. C. Fung, *A First Course in Continuum Mechanics*. Prentice-Hall, Inc., 1994.

[22] K. Terzaghi, *Theoretical Soil Mechanics*. New York: Wiley, 1943.

[23] M. A. Biot, "General theory of three-dimensional consolidation," *Journal of Applied Physics*, vol. 12, pp. 155–164, 1941.

[24] M. A. Biot and D. G. Willis, "The elastic coefficients of the theory of consolidation," *Journal of Applied Physics*, pp. 594–ï£¡601, 1957.

[25] S. E. Benzley, "Representation of singularities with isoparametric finite elements," *International Journal for Numerical Methods in Engineering*, 1974.

[26] M. S. T. J. R. Hughes, "Techniques for developing special finite element shape functions with particular references to singularities.," *Internatinoal Journal for Numerical Methods in Engineering*, 1980.

[27] J. Wan, *Stabilized finite element methods for coupled geomechanics and multiphase flow*. Ph.D. Dissertation, Stanford University, 2002.

[28] J. White and R. I. Borja, "Stabilized low-order finite elements for coupled solid-deformation/fluid-diffusion and their application to fault zone transients," *Computer Methods in Applied Mechanics and Engineering*, vol. 197, p. 4353ï£¡4366, 2008.

[29] P. A. Vermeer and A. Verruijt, "An accuracy condition for consolidation by finite elements," *International Journal for Numerical and Analytical Methods in Geomechanics*, vol. 5, pp. 1–14, 1981.

[30] A. Truty and T. Zimmermann, "Stabilized mixed finite element formulations for materially nonlinear partially saturated two-phase media," *Computer Methods in Applied Mechanics and Engineering*, vol. 195, pp. 1517–ï£¡1546, 2006.

[31] T. J. R. Hughes, *The Finite Element Method: Linear Static and Dynamic Finite Element Analysis*. Englewood Cliffs, NJ: Prentice-Hall, 1987.

[32] M. Fortin and F. Brezzi, *Mixed and Hybrid Finite Element Methods*. Springer, 1991.

[33] L. C. Evans, *Partial Differential Equations*. American Mathematical Society, 1998.

[34] P. K. Vijalapura, J. Strain, and S. Govindjee, "Fractional step methods for index-1 differential-algebraic equations," *Journal of Computational Physics*, vol. 203, pp. 305–320, 2005.

[35] I. Aavatsmark, "An introduction to multipoint flux approximations for quadrilateral grids," *Computational Geosciences*, vol. 6, pp. 405–432, 2002.

[36] R. Juanes, J. Kim, S. F. Matringe, and L. K. Thomas, "Implementation and application of a hybrid multipoint flux approximation for reservoir simulation on corner-point grids," in *SPE Annual Technical Conference and Exhibition (SPE 95928)*, (Dallas), Sep. 2005.

[37] J. Kim, H. A. Tchelepi, and R. Juanes, "Stability and convergence of sequential methods for coupled flow and geomechanics: Drained and undrained splits," *Computer Methods in Applied Mechanics and Engineering*, vol. 200, pp. 2094–2116, 2011.

[38] J. Kim, H. A. Tchelepi, and R. Juanes, "Stability and convergence of sequential methods for coupled flow and geomechanics: Fixed-stress and fixed-strain splits," *Computer Methods in Applied Mechanics and Engineering*, vol. 200, pp. 1591–1606, 2011.

[39] N. Castelletto, J. White, and H. Tchelepi, "Accuracy and convergence properties of the fixed-stress iterative solution of two-way coupled poromechanics," *International Journal for Numerical and Analytical Methods in Geomechanics*, vol. 39, no. 14, pp. 1593ï£¡–1618, 2015.

[40] A. Mikelic and M. Wheeler, "Convergence of iterative coupling for coupled flow and geomechanics," *Computational Geosciences*, vol. 17, no. 3, pp. 455ï£¡–461, 2013.

[41] W. Wood, *Practical Time-stepping Schemes*. Oxford, 1990.

[42] E. Hairer and G. Wanner, *Solving Ordinary Differential Equations II: Stiff and Differential-Algebraic Problems*. Springer, 1993.

[43] J. Morris, *Computational Methods in Elementary Numerical Analysis*. John Wiley and Sons, 1983.

[44] R. D. Richtmyer and K. W. Morton, *Difference Methods for Initial Value Problems*. Chichester, England: John Wiley and Sons, second edition ed., 1967.

[45] O. Coussy, *Mechanics of porous continua*. Chichester, England: John Wiley and Sons, 1995.

[46] J. Geertsma, "The effect of fluid pressure decline on volumetric change of porous rocks," *Petroleum Transactions, AIME*, vol. 210, pp. 331–340, 1957.

[47] K. E. Brenan, S. L. Campbell, and L. R. Petzold, *Numerical Solution of Initial-Value Problems in Differential-Algebraic Equations*. Philadelphia: SIAM, 1996.

[48] W. E. Schiesser, *The Numerical Method of Lines: Integration of Partial Differential Equations*. Academic Press, 1991.

[49] K. Park, "Partitioned transient analysis procedures for coupled-field problems: stability analysis," *Journal of Applied Mechanics*, vol. 47, no. 2, pp. 370–376, 1980.

[50] K. C. Park, "Stabilization of partitioned solution procedure for pore fluid-soil interaction analysis," *International Journal for Numerical Methods in Engineering*, vol. 19, no. 11, pp. 1669–1673, 1983.

[51] O. C. Zienkiewicz, D. K. Paul, and A. H. C. Chan, "Unconditionally stable staggered solution procedure for soil-pore fluid interaction problems," *International Journal for Numerical Methods in Engineering*, vol. 26, no. 5, pp. 1039–1055, 1988.

[52] F. Armero and J. C. Simo, "A new unconditionally stable fractional step method for non-linear coupled thermomechanical problems," *International Journal for Numerical Methods in Engineering*, vol. 35, pp. 737–766, 1992.

[53] J. Kim, H. A. Tchelepi, and R. Juanes, "Stability, accuracy, and efficiency of sequential methods for coupled flow and geomechanics," *SPE Journal*, vol. 16, no. 2, pp. 249–262, 2011. SPE-119084-PA.

[54] R. W. Lewis and Y. Sukirman, "Finite element modelling of three-phase flow in deforming saturated oil reservoirs," *International Journal for Numerical and Analytical Methods in Geomechanics*, vol. 17, pp. 577–598, 1993.

[55] J. A. White, N. Castelletto, and H. A. Tchelepi, "Block-partitioned solvers for coupled poromechanics: A unified framework," *Computer Methods in Applied Mechanics and Engineering*, vol. 303, pp. 55–74, 2016.

[56] R. W. Lewis and H. R. Ghafouri, "A novel finite element double porosity model for multiphase flow through deformable fractured porous media," *International Journal for Numerical and Analytical Methods in Geomechanics*, vol. 21, pp. 789 ï£¡– 816, 1997.

[57] M. A. Murad and A. F. D. Loula, "Improved accuracy in finite element analysis of biot's consolidation problem," *Computer Methods in Applied Mechanics and Engineering*, vol. 95, pp. 359–382, 1992.

[58] M. A. Murad and A. F. D. Loula, "On stability and convergence of finite element approximations of biot's consolidation problem," *Computer Methods in Applied Mechanics and Engineering*, vol. 37, pp. 645–667, 1994.

[59] J. Choo and R. Borja, "Stabilized mixed finite elements for deformable porous media with double porosity," *Computer Methods in Applied Mechanics and Engineering*, vol. 293, pp. 131–154, 2015.

[60] J. M. Nordbotten, "Stable cell-centered finite volume discretization for biot equations," *SIAM Journal on Numerical Analysis*, vol. 54, pp. 942–968, 2016.

[61] A. Ženišek, "The existence and uniqueness theorem in biot's consolidation theory," *Aplikace matematiky*, vol. 29, pp. 194–210, 1984.

[62] U. Langer and W. Queck, "On the convergence factor of uzawa's algorithm," *Journal of Computational and Applied Mathematics*, vol. 15, pp. 191–202, 1986.

[63] H. C. Elman and G. H. Golub, "Inexact and preconditioned uzawa algorithms for saddle point problems," *SIAM Journal on Numerical Analysis*, vol. 31, pp. 1645–1661, 1994.

[64] F. Brezzi and J. Pitkarata, "On the stability of finite element approximations of stokes problem, in efficient solutions of elliptic systems," in *Efficient Solutions of Elliptic Systems, Notes on Numerical Fluid Mechanics*, vol. 10, pp. 11–19, Springer, 1984. edited by W. Hackbusch.

[65] G. Strang, *Linear Algebra and Its Applications*. Brooks/Cole, third edition ed., 1988.

[66] K. Pruess and T. N. Narasimhan, "A practical method for modeling fluid and heat flow in fractured porous media," *SPE Journal*, vol. 25, no. 1, pp. 14 ï£¡– 26, 1985.

[67] J. G. Berryman, "Extension of poroelastic analysis to double-porosity materials: New technique in microgeomechanics," *Journal of Engineering Mechanics-ASCE*, vol. 128, no. 8, pp. 840 ï£¡– 847, 2002.

[68] J. Kim, E. Sonnenthal, and J. Rutqvist, "Formulation and sequential numerical algorithms of coupled fluid/heat flow and geomechanics for multiple porosity materials.," *International Journal for Numerical Methods in Engineering*, vol. 92, pp. 425–456, 2012.

[69] J. Wan, L. J. Durlofsky, T. J. R. Hughes, and K. Aziz, "Stabilized finite element methods for coupled geomechanicsï£¡reservoir flow simulations," in *SPE Reservoir Simulation Symposium (SPE 79694)*, (Houston), Feb. 2003. 3-5 Feb.

[70] J. McNamee and R. Gibson, "Displacement functions and linear transformations applied to diffusion through porous elastic media," *The Quarterly Journal of Mechanics and Applied Mathematics*, vol. 13, pp. 98–111, 1960.

[71] J. McNamee and R. Gibson, "Plane strain and axially symmetric problems of the

consolidation of a semi-infinite clay stratum," *The Quarterly Journal of Mechanics and Applied Mathematics*, vol. 13, pp. 210–227, 1960.

[72] E. Hairer, S. Norsett, and W. G., *Solving Ordinary Differential Equations I: Nonstiff Problems*. Springer, 1993.

[73] M. Tenenbaum and H. Pollard, *Ordinary Differential Equations*. Harper & Row, 1963.

[74] R. Frank and C. Ueberhuber, "Iterated defect correction for the efficient solution of stiff systems of ordinary differential equations," *BIT Numerical Mathematics*, vol. 17, no. 2, pp. 146–159, 1977.

[75] A. Dutt, L. Greengard, and V. Rokhlin, "Spectral deferred correction methods for ordinary differential equations," *BIT Numerical Mathematics*, vol. 40, no. 2, pp. 241–266, 2000.

[76] S. G., "On construction and comparison of difference schemes," *SIAM Journal on Numerical Analysis*, vol. 5, no. 3, pp. 506–517, 1968.

[77] R. McLachlan and G. Quispel, "Splitting methods," *Acta Numerica*, vol. 11, pp. 341–434, 2002.

[78] L. K. Thomas, L. Y. Chin, R. G. Pierson, and J. E. Sylte, "Coupled geomechanics and reservoir simulation," *SPE Journal*, vol. 8, no. 4, pp. 350–358, 2003.

[79] D. Tran, A. Settari, and L. Nghiem, "New iterative coupling between a reservoir simulator and a geomechanics module," *SPE Journal*, vol. 9, no. 3, pp. 362–369, 2004.

[80] L. Martin, R. Wolters, J. Rutqvist, K.-H. Lux, and J. Birkholzer, "Comparison of two simulators to investigate thermal-hydraulic-mechanical processes related to nucluear waste isolation in saliniferous formations," *Computers and Geotechnics*, vol. 66, pp. 219–229, 2015.

[81] K. Bathe, *Finite element procedures*. Englewood Cliffs, NJ: Prentice-Hall, 1996.

[82] K. Bathe, E. Ramm, and E. Wilson, "Finite element formulations for large deformation dynamic analysis," *International Journal for Numerical Methods in Engineering*, vol. 9, pp. 353–386, 1975.

[83] F. Armero, "Formulation and finite element implementation of a multiplicative model of coupled poro-plasticity at finite strains under fully saturated conditions," *Computer Methods in Applied Mechanics and Engineering*, vol. 171, pp. 205–241, 1999.

[84] J. C. Simo and T. J. R. Hughes, *Computational inelasticity*. Heidelberg: Springer, 1998.

[85] J. Simo, "A framework for finite strain elastoplasticity based on maximum plastic dissipation and the multiplicative decomposition. part i: continuum formulation," *Computer Methods in Applied Mechanics and Engineering*, vol. 66, pp. 199–219, 1988.

[86] J. Simo, "A framework for finite strain elastoplasticity based on maximum plastic dissipation and the multiplicative decomposition. part ii: computational aspects," *Computer Methods in Applied Mechanics and Engineering*, vol. 68, pp. 1–31, 1988.

[87] J. Simo, "Algorithms for static and dynamic multiplicative plasticity that preserve the classical return mapping schemes of the infinitesimal theory," *Computer Methods in Applied Mechanics and Engineering*, vol. 99, pp. 61–112, 1992.

[88] J. Kim, "A numerically stable sequential implicit algorithm for finite-strain elastoplastic geomechanics coupled to fluid flow," *SPE Reservoir Simulation Symposium*, 2015.

[89] K. Min and L. Jing, "Numerical determination of the equivalent elastic compliance tensor for fractured rock masses using the distinct element method," *International Journal of Rock Mechanics and Mining Sciences*, vol. 40, no. 6, pp. 795–816, 2003.

[90] J. E. Marsden and T. J. R. Hughes, *Mathematical Foundations of Elasticity*. Englewood Cliffs, NJ: Prentice-Hall, 1983.

APPENDIX A

THE LINEARIZED FORM USING Q1Q1 FOR A 1D PROBLEM OF POROMECHANICS

In this appendix, we derive the final linearized form of poromechanics using the Q1Q1 formulation for a simple 1D problem as an example.

A.1 Strong Form

When we assume the no gravity and 1D space, then for the momentum balance for geomechanics, Equation 2.3, expressed as,

$$\text{Div}\sigma = 0, \tag{A.1}$$

and for the mass balance for fluid flow, Equation 2.4, expressed as,

$$\frac{dm}{dt} + \text{Div}w = \rho_{f,0} f. \tag{A.2}$$

A.2 Linearized Form

Since the Q1Q1 space takes the same shape function of η_h for both displacement and pressure, the approximations for both fields are as follows:

$$u_h = \sum_a \eta_a u_a, \;\; p_h = \sum_a \eta_a p_a, \tag{A.3}$$

Then using the virtual work method, the variational form with discretized equations

can be expressed similar to Equation 2.14, and 2.15

$$\int_{\Omega} \mathbf{Grad}^{s} \eta_h \sigma_h \, d\Omega = \int_{\Gamma_\sigma} \eta_h \bar{t} \, d\Gamma, \tag{A.4}$$

$$\frac{1}{\rho_{f,0}} \int_{\Omega} \eta_h \frac{\partial m_h}{\partial t} \, d\Omega + \int_{\Omega} \eta_h \mathrm{Div} v_h \, d\Omega = \int_{\Omega} \eta_h f \, d\Omega. \tag{A.5}$$

Using the constitutive relations of Equation 2.5 and 2.6,

$$\int_{\Omega} B_a^T \sigma_h \, d\Omega = \int_{\Gamma_\sigma} \eta_a \bar{t} \, d\Gamma, \tag{A.6}$$

$$\int_{\Omega} \eta_a \frac{1}{M} \frac{\partial p_h}{\partial t} \, d\Omega + \int_{\Omega} \eta_a b \frac{\partial \varepsilon_v}{\partial t} \, d\Omega + \int_{\Gamma_\sigma} B_a v_h \, d\Gamma = \int_{\Omega_i} \eta_a f \, d\Omega, \tag{A.7}$$

which is for $\forall a = 1, \ldots, n_{\text{node}}$. Note that $\sigma_h = D\partial_x u_a - b p_h$, $B_a = \partial_x \eta_a$, where $D = \frac{E(1-\nu)}{(1+\nu)(1-2\nu)}$, and b and M are Biot's coefficient and modulus, respectively.

When the spatially discretized variable u_h and p_h are expressed with $\boldsymbol{U}$ and $\boldsymbol{P}$, using Galerkin's method, Equation A.6 and A.7 are transformed into

$$\underbrace{\int_{\Omega} B_a^T D B_b \, d\Omega}_{\boldsymbol{K}} \boldsymbol{U} - \underbrace{\int_{\Omega} b B_a \eta_b \, d\Omega}_{\boldsymbol{L}^T} \boldsymbol{P} = \underbrace{\int_{\Gamma_\sigma} \eta_a \bar{t} \, d\Gamma}_{\boldsymbol{s}^u}, \tag{A.8}$$

$$\underbrace{\int_{\Gamma_\sigma} B_a \lambda B_b \, d\Gamma}_{\boldsymbol{T}} \boldsymbol{P} + \underbrace{\int_{\Omega} b \eta_a B_b \, d\Omega}_{\boldsymbol{L}} \dot{\boldsymbol{U}} + \underbrace{\int_{\Omega} \frac{1}{M} \eta_a \eta_b \, d\Omega}_{\boldsymbol{Q}} \dot{\boldsymbol{P}} = \underbrace{\int_{\Gamma_\sigma} \eta_a f \, d\Omega}_{\boldsymbol{s}^p}, \tag{A.9}$$

for $\forall a = 1, \ldots, n_{\text{node}}$, $\forall b = 1, \ldots, n_{\text{node}}$ and where $\lambda = -\frac{k}{\mu}$, the mobility ratio. Thus, the final matrix form is

$$\underbrace{\begin{bmatrix} \boldsymbol{K} & -\boldsymbol{L}^T \\ \boldsymbol{0} & \boldsymbol{T} \end{bmatrix}}_{\boldsymbol{C}} \underbrace{\begin{bmatrix} \boldsymbol{U} \\ \boldsymbol{P} \end{bmatrix}}_{\boldsymbol{x}} + \underbrace{\begin{bmatrix} \boldsymbol{0} & \boldsymbol{0} \\ \boldsymbol{L} & \boldsymbol{Q} \end{bmatrix}}_{\boldsymbol{D}} \underbrace{\begin{bmatrix} \dot{\boldsymbol{U}} \\ \dot{\boldsymbol{P}} \end{bmatrix}}_{\dot{\boldsymbol{x}}} = \underbrace{\begin{bmatrix} \boldsymbol{s}^u \\ \boldsymbol{s}^p \end{bmatrix}}_{\boldsymbol{s}}, \tag{A.10}$$

which is the same form as Equation 4.11.

APPENDIX B

COMPRESSIBLE AND INCOMPRESSIBLE MECHANICS

In this appendix, the mechanics problem which is expressed with the static momentum balance equation is addressed in conjunction with mechanical pressure or mean stress with two different compressibilities: compressible case vs. incompressible case.

B.1 Energy Form

Basically, the variational form of momentum balance equation has the final discretized or matrix form based on the Hooke's law as

$$\boldsymbol{K}\boldsymbol{u} = \boldsymbol{f}, \tag{B.1}$$

where $\boldsymbol{K}$ is stiffness matrix, $\boldsymbol{u}$ is displacement vector, and $\boldsymbol{f}$ is force vector.

It should be noted that Equation B.1 is equivalent to the solution of minimizing energy, where the energy or work for elastic problem can be expressed with

$$\frac{1}{2}\int_{\Omega} \boldsymbol{\varepsilon} : \boldsymbol{\sigma} d\Omega, \tag{B.2}$$

where Ω is a domain to be considered. Then, the energy function F is defined as

$$F(\boldsymbol{u}) = \frac{1}{2}\boldsymbol{u}^T\boldsymbol{K}\boldsymbol{u} - \boldsymbol{u}^T\boldsymbol{f}, \tag{B.3}$$

and with Equation B.3, the minimization is taken from

$$\min F(\boldsymbol{u}) \Rightarrow \frac{d}{d\epsilon}F(\boldsymbol{u} + \epsilon\boldsymbol{c})|_{\epsilon=0} = 0 \Leftrightarrow \boldsymbol{K}\boldsymbol{u} = \boldsymbol{f}, \tag{B.4}$$

where ϵ is a perturbation coefficient and $\boldsymbol{c}$ is an arbitrary vector. The proof of this equivalence is omitted here.

B.2 Compressible Mechanics

Since the stress and strain tensor are composed of the volumetric (mean) part and the deviatoric (shear) part as Equation 2.10 and 2.11 in Mathematical Formulations, Equation B.3 is decomposed into

$$F(\boldsymbol{u}) = \frac{1}{2}\boldsymbol{u}^T\boldsymbol{K}\boldsymbol{u} - \boldsymbol{u}^T\boldsymbol{f} = \frac{1}{2}\boldsymbol{u}^T\tilde{\boldsymbol{K}}\boldsymbol{u} - \boldsymbol{u}^T\tilde{\boldsymbol{B}}^T\boldsymbol{p_M} - \boldsymbol{u}^T\boldsymbol{f}, \tag{B.5}$$

where $\boldsymbol{p_M}$ is a mechanical pressure (scalar), $\tilde{\boldsymbol{K}}$ belongs to the deviatoric part and $\tilde{\boldsymbol{B}}$ belongs to the mean stress, corresponding to the mechanical pressure, from $\boldsymbol{K}$. Let us minimize $F(\boldsymbol{u})$.

$$\begin{aligned} F(\boldsymbol{u}+\epsilon\boldsymbol{c}) &= \frac{1}{2}(\boldsymbol{u}+\epsilon\boldsymbol{c})^T\tilde{\boldsymbol{K}}(\boldsymbol{u}+\epsilon\boldsymbol{c}) - (\boldsymbol{u}+\epsilon\boldsymbol{c})^T\tilde{\boldsymbol{B}}^T\boldsymbol{p_M} - (\boldsymbol{u}+\epsilon\boldsymbol{c})^T\boldsymbol{f} \\ &= \frac{1}{2}(\boldsymbol{u}+\epsilon\boldsymbol{c})^T\tilde{\boldsymbol{K}}(\boldsymbol{u}+\epsilon\boldsymbol{c}) - (\boldsymbol{u}^T+\epsilon\boldsymbol{c}^T)\tilde{\boldsymbol{B}}^T\boldsymbol{p_M} - (\boldsymbol{u}^T+\epsilon\boldsymbol{c}^T)\boldsymbol{f} \\ &= \frac{1}{2}(\boldsymbol{u}^T\tilde{\boldsymbol{K}}\boldsymbol{u} + \epsilon\boldsymbol{u}^T\tilde{\boldsymbol{K}}\boldsymbol{c} + \epsilon\boldsymbol{c}^T\tilde{\boldsymbol{K}}\boldsymbol{u} + \epsilon^2\boldsymbol{c}^T\tilde{\boldsymbol{K}}\boldsymbol{c}) - (\boldsymbol{u}^T\tilde{\boldsymbol{B}}^T\boldsymbol{p_M} + \epsilon\boldsymbol{c}^T\tilde{\boldsymbol{B}}^T\boldsymbol{p_M}) \\ &\quad - (\boldsymbol{u}^T\boldsymbol{f} + \epsilon\boldsymbol{c}^T\boldsymbol{f}). \end{aligned} \tag{B.6}$$

Then, $\frac{d}{d\epsilon}F(\boldsymbol{u}+\epsilon\boldsymbol{c})$ is expressed as

$$\frac{d}{d\epsilon}F(\boldsymbol{u}+\epsilon\boldsymbol{c}) = \frac{1}{2}(\boldsymbol{u}^T\tilde{\boldsymbol{K}}\boldsymbol{c} + \boldsymbol{c}^T\tilde{\boldsymbol{K}}\boldsymbol{u} + 2\epsilon\boldsymbol{c}^T\tilde{\boldsymbol{K}}\boldsymbol{c}) - (\boldsymbol{c}^T\tilde{\boldsymbol{B}}^T\boldsymbol{p_M}) - \boldsymbol{c}^T\boldsymbol{f}. \tag{B.7}$$

Thus, $\frac{d}{d\epsilon}F(\boldsymbol{u}+\epsilon\boldsymbol{c})|_{\epsilon=0}$ is

$$\begin{aligned}\frac{d}{d\epsilon}F(\boldsymbol{u}+\epsilon\boldsymbol{c})|_{\epsilon=0} &= \frac{1}{2}(\boldsymbol{u}^T\tilde{\boldsymbol{K}}\boldsymbol{c}+\boldsymbol{c}^T\tilde{\boldsymbol{K}}\boldsymbol{u})-(\boldsymbol{c}^T\tilde{\boldsymbol{B}}^T\boldsymbol{p_M})-\boldsymbol{c}^T\boldsymbol{f}\\ &= \boldsymbol{c}^T\tilde{\boldsymbol{K}}\boldsymbol{u}-\boldsymbol{c}^T\tilde{\boldsymbol{B}}^T\boldsymbol{p_M}-\boldsymbol{c}^T\boldsymbol{f}\\ &= \boldsymbol{c}^T(\tilde{\boldsymbol{K}}\boldsymbol{u}-\tilde{\boldsymbol{B}}^T\boldsymbol{p_M}-\boldsymbol{f}).\end{aligned} \tag{B.8}$$

Therefore, we have $\tilde{\boldsymbol{K}}\boldsymbol{u}-\tilde{\boldsymbol{B}}^T\boldsymbol{p_M}=\boldsymbol{f}$, equivalent to Equation B.4.

Since the volumetric strain (scalar) $\varepsilon_v=\tilde{\boldsymbol{B}}\boldsymbol{u}=-\frac{1}{K}p_M$ where K is the bulk modulus, we finally have the equation of matrix form from Equation B.8 as

$$\begin{bmatrix}\tilde{\boldsymbol{K}} & -\tilde{\boldsymbol{B}}^T\\ \tilde{\boldsymbol{B}} & \boldsymbol{C}_M\end{bmatrix}\begin{bmatrix}\boldsymbol{u}\\ \boldsymbol{p_M}\end{bmatrix}=\begin{bmatrix}\boldsymbol{f}\\ \boldsymbol{0}\end{bmatrix}, \tag{B.9}$$

where $\boldsymbol{C}_M=\text{diag}(1/K)$.

B.3 Incompressible Mechanics

In order to account for the compressibility constraint from above, the Lagrangian multiplier method needs to be introduced. Assuming that the constraint is expressed with $\boldsymbol{B}\boldsymbol{u}=\boldsymbol{g}$ and if we set a variable, $\boldsymbol{p}$, as the Lagrangial multiplier, then the Equation B.3 is expressed with $L(\boldsymbol{u},\boldsymbol{p})$ as

$$L(\boldsymbol{u},\boldsymbol{p})=\frac{1}{2}\boldsymbol{u}^T\boldsymbol{K}\boldsymbol{u}-\boldsymbol{u}^T\boldsymbol{f}+(\boldsymbol{B}\boldsymbol{u}-\boldsymbol{g})\boldsymbol{p}. \tag{B.10}$$

Thus, let us minimize by taking derivative of ϵ with arbitrary variables of $\boldsymbol{c}$ and $\boldsymbol{m}$ corresponding to $\boldsymbol{u}$ and $\boldsymbol{p}$ as

$$\min L(\boldsymbol{u},\boldsymbol{p})\Rightarrow\frac{d}{d\epsilon}L(\boldsymbol{u}+\epsilon\boldsymbol{c},\boldsymbol{p}+\epsilon\boldsymbol{m})|_{\epsilon=0}=0. \tag{B.11}$$

Following the same procedure above,

$$\begin{aligned} L(\boldsymbol{u}+\epsilon\boldsymbol{c},\boldsymbol{p}+\epsilon\boldsymbol{m}) &= \frac{1}{2}(\boldsymbol{u}+\epsilon\boldsymbol{c})^T\boldsymbol{K}(\boldsymbol{u}+\epsilon\boldsymbol{c}) + (\boldsymbol{u}+\epsilon\boldsymbol{c})^T\boldsymbol{B}^T(\boldsymbol{p}+\epsilon\boldsymbol{m}) \\ &\quad - (\boldsymbol{u}+\epsilon\boldsymbol{c})^T\boldsymbol{f} - (\boldsymbol{p}+\epsilon\boldsymbol{m})^T\boldsymbol{g} \\ &= \frac{1}{2}(\boldsymbol{u}+\epsilon\boldsymbol{c})^T\boldsymbol{K}(\boldsymbol{u}+\epsilon\boldsymbol{c}) + (\boldsymbol{u}^T+\epsilon\boldsymbol{c}^T)\boldsymbol{B}^T(\boldsymbol{p}+\epsilon\boldsymbol{m}) \\ &\quad - (\boldsymbol{u}^T+\epsilon\boldsymbol{c}^T)\boldsymbol{f} - (\boldsymbol{p}^T+\epsilon\boldsymbol{m}^T)\boldsymbol{g} \\ &= \frac{1}{2}(\boldsymbol{u}^T\boldsymbol{K}\boldsymbol{u} + \epsilon\boldsymbol{u}^T\boldsymbol{K}\boldsymbol{c} + \epsilon\boldsymbol{c}^T\boldsymbol{K}\boldsymbol{u} + \epsilon^2\boldsymbol{c}^T\boldsymbol{K}\boldsymbol{c}) \\ &\quad + (\boldsymbol{u}^T\boldsymbol{B}^T\boldsymbol{p} + \epsilon\boldsymbol{u}^T\boldsymbol{B}^T\boldsymbol{m} + \epsilon\boldsymbol{c}^T\boldsymbol{B}^T\boldsymbol{p} + \epsilon^2\boldsymbol{c}^T\boldsymbol{B}^T\boldsymbol{m}) \\ &\quad - (\boldsymbol{u}^T\boldsymbol{f} + \boldsymbol{p}^T\boldsymbol{g} + \epsilon\boldsymbol{c}^T\boldsymbol{f} + \epsilon\boldsymbol{m}^T\boldsymbol{g}). \end{aligned} \tag{B.12}$$

Thus, $\frac{d}{d\epsilon}L(\boldsymbol{u}+\epsilon\boldsymbol{c},\boldsymbol{p}+\epsilon\boldsymbol{m})|_{\epsilon=0}$ is

$$\begin{aligned} \frac{d}{d\epsilon}L(\boldsymbol{u}+\epsilon\boldsymbol{c},\boldsymbol{p}+\epsilon\boldsymbol{m})|_{\epsilon=0} &= \frac{1}{2}(\boldsymbol{u}^T\boldsymbol{K}\boldsymbol{c} + \boldsymbol{c}^T\boldsymbol{K}\boldsymbol{u}) + (\boldsymbol{u}^T\boldsymbol{B}^T\boldsymbol{m} + \boldsymbol{c}^T\boldsymbol{B}^T\boldsymbol{p}) \\ &\quad - (\boldsymbol{c}^T\boldsymbol{f} + \boldsymbol{m}^T\boldsymbol{g}) \\ &= \boldsymbol{c}^T\boldsymbol{K}\boldsymbol{u} + \boldsymbol{c}^T\boldsymbol{B}^T\boldsymbol{p} - \boldsymbol{c}^T\boldsymbol{f} + \boldsymbol{m}^T\boldsymbol{B}\boldsymbol{u} - \boldsymbol{m}^T\boldsymbol{g} \\ &= \boldsymbol{c}^T(\boldsymbol{K}\boldsymbol{u} + \boldsymbol{B}^T\boldsymbol{p} - \boldsymbol{f}) + \boldsymbol{m}^T(\boldsymbol{B}\boldsymbol{u} - \boldsymbol{g}). \end{aligned} \tag{B.13}$$

Therefore, we have $\boldsymbol{K}\boldsymbol{u} + \boldsymbol{B}^T\boldsymbol{p} = \boldsymbol{f}$ and $\boldsymbol{B}\boldsymbol{u} = \boldsymbol{g}$. In matrix form,

$$\begin{bmatrix} \boldsymbol{K} & \boldsymbol{B}^T \\ \boldsymbol{B} & \boldsymbol{0} \end{bmatrix} \begin{bmatrix} \boldsymbol{u} \\ \boldsymbol{p} \end{bmatrix} = \begin{bmatrix} \boldsymbol{f} \\ \boldsymbol{g} \end{bmatrix}, \tag{B.14}$$

and when the constraint is incompressibility ($\boldsymbol{g} = \boldsymbol{0}$) then,

$$\begin{bmatrix} \boldsymbol{K} & \boldsymbol{B}^T \\ \boldsymbol{B} & \boldsymbol{0} \end{bmatrix} \begin{bmatrix} \boldsymbol{u} \\ \boldsymbol{p} \end{bmatrix} = \begin{bmatrix} \boldsymbol{f} \\ \boldsymbol{0} \end{bmatrix}. \tag{B.15}$$

Note that it has the same form as Equation B.9 when $K \to \infty$ through which incompressible mechanics is addressed and also it is the same form as the incompressible Stoke's flow equation.

APPENDIX C

SOBOLEV SPACES OF FUNCTIONS

Following [31], there are classes of functions need to be introduced which possess generalized derivatives including weak derivatives and certain integrability properties. Among them, Sobolev spaces are particular examples especially for weak formulations and finite element spaces of elliptic boundary value problems (PDEs).

Sobolev spaces are defined as

$$H^k = H^k(\Omega) = \left\{ \omega | \omega \in L_2; \omega_{,x} \in L_2; \cdots ; \omega_{,\underbrace{x \ldots x}_{\text{k times}}} \in L_2 \right\}, \tag{C.1}$$

where

$$L_2 = L_2(\Omega) = \left\{ \omega | \int_\Omega \omega^2 d\Omega < \infty \right\}, \tag{C.2}$$

that is square integrable space. Thus, H^1 space is the space where upto the first derivative of a function can be integrable.

Then we can define norm to measure the distance within space such as for u, L_2 norm, expressed as $||\cdot||_0$ with

$$||u||_0 = \left(\int_\Omega u^2 d\Omega \right)^{1/2}, \tag{C.3}$$

and H^1 norm expressed as $||\cdot||_1$ as

$$||u||_1 = \left(\int_\Omega \left(u^2 + u_{,x}^2 \right) d\Omega \right)^{1/2}. \tag{C.4}$$

APPENDIX D

THE DAES AND ITS INDEX

Following [47], a function $u(t)$ is a classical (generally not numerical) solution of the general nonlinear DAE

$$F(t, u, \dot{u}) = 0, \tag{D.1}$$

on a certain interval I it satisfies Equation D.1 for all time $t \in I$. $\dot{()}$ is a time derivative. Chances are that u is continuously differentiable (C^{∞}) for some interval but it can be just continuous (C^{0}) on other portion of I, leading to DAE's can exhibit all the behavior of ODE's plus additional behavior other than ODE.

The minimum number of times that all or part of Equation D.1 must be differentiated with respect to time in order to determine $\dot{u}$ as a continuous function of u and t is the index of the DAE of Equation D.1.

For example, if we have a semi-explicit type of DAEs

$$\dot{x} = f(x, y, t), \tag{D.2}$$

$$0 = g(x, y, t), \tag{D.3}$$

similar to the equations for poromechanics, then the constraint equation D.3 can be differentiated with time t once,

$$\dot{x} = f(x, y, t), \tag{D.4}$$

$$g_x(x, y, t)\dot{x} + g_y(x, y, t)\dot{y} = -g_t(x, y, t), \tag{D.5}$$

where subscripts mean partial differentiation. If g_y is nonsingular that it can be invertible,

then the system of Equation D.4 and D.5 leads to be an implicit ODE, thus it has index 1. The number of differentiation steps required in the constraint equation in this case is the number of index of DAEs.

APPENDIX E

INF-SUP CONDITION FOR STOKES PROBLEM

Let us consider Stokes problem for incompressible fluid flow within a domain, $\Omega \in \mathbb{R}^{\mathrm{d}}$, seeking $\boldsymbol{u} \in H_0^1(\Omega)^d$ and $p \in L_0^2(\Omega)$ (Q1P0) with governing equations as

$$-\Delta \boldsymbol{u} + \mathbf{Grad} p = \boldsymbol{f} \qquad in \quad \Omega, \tag{E.1}$$

$$\mathrm{Div} \boldsymbol{u} = 0 \qquad in \quad \Omega, \tag{E.2}$$

$$\boldsymbol{u} = \boldsymbol{u}_0 \qquad on \quad \partial\Omega, \tag{E.3}$$

where $\boldsymbol{f} \in L^2(\Omega)^d$.

Then weak form or the variational formulation is seeking (u, p) expressed as,

$$\int_\Omega \mathbf{Grad} \boldsymbol{u} : \mathbf{Grad} \boldsymbol{v} \; d\Omega - \int_\Omega p \, \mathrm{Div} \boldsymbol{v} \; d\Omega = \int_\Omega \boldsymbol{f} \boldsymbol{v} \; d\Omega \qquad for \quad \forall \boldsymbol{v} \in H_0^1(\Omega)^d, \tag{E.4}$$

$$\int_\Omega \mathrm{Div} \boldsymbol{v} \; q \; d\Omega = 0 \qquad for \quad \forall q \in L_0^2(\Omega). \tag{E.5}$$

Let $\mathbb{V}$ and $\mathbb{Q}$ be Hilbert spaces, then the above can be expressed with bilinear forms of $a : \mathbb{V} \times \mathbb{V} \to \mathbb{R}$, $b : \mathbb{V} \times \mathbb{Q} \to \mathbb{R}$ and a linear formulation of $L : \mathbb{V} \to \mathbb{R}$ as

$$a(\boldsymbol{u}, \boldsymbol{v}) + b(\boldsymbol{v}, p) = L(\boldsymbol{v}) \qquad for \quad \forall \boldsymbol{v} \in \mathbb{V}, \tag{E.6}$$

$$b(\boldsymbol{v}, p) = 0 \qquad for \quad \forall q \in \mathbb{Q} \tag{E.7}$$

In order to have a unique solution pair of $(\boldsymbol{u}, p) \in \mathbb{V} \times \mathbb{Q}$, there exists a constant $\beta > 0$ such that

$$\inf_{q\in\mathbb{Q}}\sup_{\boldsymbol{v}\in\mathbb{V}}\frac{b(\boldsymbol{v},q)}{\|\boldsymbol{v}\|_{\mathbb{V}}\,\|q\|_{\mathbb{Q}}}\geq\beta, \tag{E.8}$$

which is the inf-sup condition that must be satisfied for the uniqueness of the solution $(u,p)\in\mathbb{V}\times\mathbb{Q}$.

The above inequality is identical with

$$\begin{aligned}
\Leftrightarrow \quad & for \quad \forall q\in\mathbb{Q}, \quad \sup_{\boldsymbol{v}\in\mathbb{V}}\frac{b(\boldsymbol{v},q)}{\|\boldsymbol{v}\|_{\mathbb{V}}\,\|q\|_{\mathbb{Q}}}\geq\beta,\\
\Leftrightarrow \quad & for \quad \forall q\in\mathbb{Q},\ \exists\boldsymbol{v}\in\mathbb{V},\ b(\boldsymbol{v},q)\geq c_1c_2\,\|q\|_{\mathbb{Q}}\,\|\boldsymbol{v}\|_{\mathbb{V}}\,,\\
\Leftrightarrow \quad & for \quad \forall q\in\mathbb{Q},\ \exists\boldsymbol{v}\in\mathbb{V},\ b(\boldsymbol{v},q)\geq c_1\,\|q\|_{\mathbb{Q}}^2\ \ and\ \ \|\boldsymbol{v}\|_{\mathbb{V}}\leq c_2\,\|q\|_{\mathbb{Q}}\,,
\end{aligned}$$

where $c_1>0$ and $c_2>0$ are certain constants.

Going back to our problem, this implies the subjectivity of the divergence operator for Stokes equation from $H_0^1(\Omega)^d\rightarrow L^2(\Omega)$, since $\forall q\in L_0^2(\Omega),\ \exists\boldsymbol{v}\in H_0^1(\Omega)$ as:

$$\int_\Omega \mathrm{Div}\boldsymbol{v}\;q\;d\Omega\geq c_1\,\|q\|_{L_0^2(\Omega)}^2\,, \tag{E.9}$$

$$\|\boldsymbol{v}\|_{H_0^1(\Omega)}\leq c_2\,\|q\|_{L_0^2(\Omega)}\,, \tag{E.10}$$

which can be also viewed as the constraint of the incompressibility for Q1P0 pair.

APPENDIX F

OBJECTIVE STRESS RATE AND LIE DERIVATIVE

In this section, objective stress rate with Lie derivative concept is summarized following [84].

F.1 Objective Stress Rate

Material objects, any tensor fields on the reference configuration, remain unaltered under spatially superposed rigid body motions. By a proper orthogonal transformation which is depending only on time, any distance between two points is preserved and this is why it is called rigid. A spatial tensor field is regarded as transforming objectively under superposed rigid body motions if it transforms with the property.

However, in general spatial objects or any tensor field on the spatial configuration does not guarantee the objectivity. For example, even if the Cauchy stress tensor is objective, its material time derivative is not objective and this is why we need the objective stress rate with the total Lagrangian method.

F.2 Lie Derivative

Objective stress rates are modified time derivative of the Cauchy stress tensor to preserve the objectivity.

Following [90, 84], the Lie derivative of the Kirchhoff stress tensor ($\boldsymbol{\tau} = J\boldsymbol{\sigma}$) is

defined as

$$
\begin{aligned}
L_v\boldsymbol{\tau}_t :&= \left\{ \boldsymbol{F}_t \frac{\partial}{\partial t} \left[\boldsymbol{F}_t^{-1} \left(\boldsymbol{\tau}_t \circ \boldsymbol{\varphi}_t \right) \boldsymbol{F}_t^{-T} \right] \boldsymbol{F}_t^T \right\} \circ \boldsymbol{\varphi}_t^{-1}, \\
&= \left\{ \boldsymbol{F}_t \left[\frac{\partial}{\partial t} \boldsymbol{S}_t \right] \boldsymbol{F}_t^T \right\} \circ \boldsymbol{\varphi}_t^{-1}, \\
&= \left\{ \boldsymbol{F}_t \frac{\partial}{\partial t} \boldsymbol{F}_t^{-1} \left(\boldsymbol{\tau}_t \circ \boldsymbol{\varphi}_t \right) \boldsymbol{F}_t^{-T} \boldsymbol{F}_t^T \right\} \circ \boldsymbol{\varphi}_t^{-1} \\
&+ \left\{ \boldsymbol{F}_t \boldsymbol{F}_t^{-1} \frac{\partial}{\partial t} \left(\boldsymbol{\tau}_t \circ \boldsymbol{\varphi}_t \right) \boldsymbol{F}_t^{-T} \boldsymbol{F}_t^T \right\} \circ \boldsymbol{\varphi}_t^{-1} \\
&+ \left\{ \boldsymbol{F}_t \boldsymbol{F}_t^{-1} \left(\boldsymbol{\tau}_t \circ \boldsymbol{\varphi}_t \right) \frac{\partial}{\partial t} \boldsymbol{F}_t^{-T} \boldsymbol{F}_t^T \right\} \circ \boldsymbol{\varphi}_t^{-1}.
\end{aligned}
\tag{F.1}
$$

where $\boldsymbol{\varphi}$ is representing a motion, $\boldsymbol{S}$ is the second Piola total stress and the subscript t is indicating that it has the time for its variable. Since for the derivative of the inverse, $\frac{\partial}{\partial t}\left(\boldsymbol{F}_t^{-1}\right) = -\boldsymbol{F}_t^{-1} \frac{\partial \boldsymbol{F}_t}{\partial t} \boldsymbol{F}_t^{-1}$ and using the material time derivative over a certain material $\boldsymbol{Y}$ expressed with $\boldsymbol{y}$, the spatial quantity as,

$$
\frac{\mathrm{D}\boldsymbol{Y}(\boldsymbol{X}, t)}{\mathrm{D}t} = \frac{\partial \boldsymbol{y}(\boldsymbol{x}, t)}{\partial t} + \left(\boldsymbol{v}(\boldsymbol{x}, t) \cdot \nabla \right) \boldsymbol{y}(\boldsymbol{x}, t), \tag{F.2}
$$

where $\boldsymbol{v}$ is the spatial velocity, then we have the following expression for the Lie derivative,

$$
L_v\boldsymbol{\tau}_t = \dot{\boldsymbol{\tau}}_t - \left(\nabla \boldsymbol{v}_t \right) \boldsymbol{\tau}_t - \boldsymbol{\tau}_t \left(\nabla \boldsymbol{v}_t \right)^T, \tag{F.3}
$$

which is satisfying the objectivity.

When $\boldsymbol{c}$ is the spatial elasticity tensor and $\boldsymbol{d}$ is the spatial rate of deformation, then we have the relation of the constitutive equation as

$$
L_v\boldsymbol{\tau}_t = \boldsymbol{c} : \boldsymbol{d}_t. \tag{F.4}
$$